FACULTAD DE MEDICINA
UNIVERSIDAD DE SEVILLA

CLINICAL CORRELATES AND ADVANCED PROCESSING OF THE DOPAMINE TRANSPORTER SPECT

APPLICATIONS IN PARKINSONISM

Ismael Huertas Fernández

Trabajo presentado para optar al grado de Doctor con mención internacional por la Universidad de Sevilla

Agradecimientos / Acknowledgments

A mis padres y hermanos, porque he tenido la suerte de crecer en una familia donde estudiar ha sido un derecho primordial a la vez que una obligación. Siempre he gozado de un apoyo incondicional para seguir esta carrera y me he sentido muy arropado. Gracias a mi madre, que ha dado su vida para garantizar que tuviéramos estudios universitarios.

A mi director Pablo Mir, porque en su día, y a pesar de ser raro e inusual, apostó por incorporar un ingeniero en un equipo clínico y darme la oportunidad de aprender una profesión en la que hoy en día me desenvuelvo en el mundo. Gracias por tener esa visión tan "rara" y seguir con ella con un laboratorio clínico lleno de ingenieros ;). Gracias por no irte a tu casa después de pasar consulta y decidir crear algo: conocimiento, empleo y un grupo de amigos que trabajan juntos.

A mis trastornados, porque este trabajo es de tod@s. A mis genetistas más dicharacheras – Inma, Marta y Piluca: lo de agradeceros vuestro trabajo es lo de menos…. gracias por taaantas horas de labo, desayunos, almuerzos y ratos fuera del labo juntos. Al equipo clínico: Carla, Fátima, Juanmi, Maite, Mara, María José, Laura, Silvia y Sonia; y al equipo calambrazos: Juanfran, Paco, Paloma y Paolo. Podría escribir muchas líneas sobre vosotros, de nuevo, lo de agradeceros vuestro trabajo es lo de menos. Gracias por vuestra amistad, estoy seguro que nos quedan muchas batallas juntos en esto de las Neurociencias. A los compis de medicina nuclear: David, Javi y Jose: claro ejemplo de una colaboración exitosa, gracias por siempre estar disponibles y haber permitido que hayamos hecho este trabajo tan bonito. Y a las incorporaciones más recientes, Antonio, Cristina, Mario y Miguel, porque gran parte del futuro del laboratorio y estas líneas están en vuestras manos, así que ánimo!

To my brilliant mentor Andre Marquand, thanks for illuminating me in the world of machine learning. I have met very few people in my career with such a extraordinary mindset and those fascinating skills and work methodology. But more importantly, he is a very nice person, many thanks. To Christian Beckmann, no doubts one of the most brilliant reseachers I've ever met. Thanks for creating that wonderful SIN group and providing insights to my work. To Marianne, Erik for their excellent work with the striatum. To my team mates and friends Thomas, Roselyne and Izabela, for welcoming me in the group and making my stay in Nijmegen even much nicer. To my beloved roomies Maria and Leonore, for our deep roomchats, i loved them.

A mis Iberian Donderians: Alberto: gracias por las charlas frikis que tanto adoro y tu amistad, estoy seguro que un día pegaremos el pelotazo juntos. A mis hermanas de viaje: Mar - my sister - y fancy Sarita. Por las terapias, los kultuurs, los anne-miekes y los credibles. Desde luego, una etapa de felicidad que nunca olvidaremos, nos vemos en el Camarón Research Centre.

A los compis de FISEVI, en especial a Blanca Delgado y Pablo Hervás, por ser personas tan valiosas y eficientes en su trabajo. Al resto de compañeros del IBiS: seguridad, cafetería, limpieza y mantenimiento, por hacer que el IBiS haya sido un agradable "hogar" de trabajo durante más de 4 años.

TABLE OF CONTENT

Introduction

Parkinson disease

Parkinson's disease (PD) is the second most prevalent neurodegenerative disease after Alzheimer disease. Ageing is one of the most influencing risk factors, and as the worldwide life expectancy continues to grow, PD is expected to affect to 8.7 million people by 2030 (Dorsey et al., 2007).

PD is pathophysiologically characterized by a decline in striatal dopamine due to the degeneration of neurons arising from the pars compacta of the substantia nigra (SNpc). This degeneration gives rise in the early phase to the cardinal motor signs of bradykinesia, rigidity, resting tremor and postural instability. Non-motor features are also frequently present before the onset of the classical motor symptoms. This premotor or prodromal phase can be characterised by impaired olfaction, constipation, depression, excessive daytime sleepiness, and rapid eye movement sleep behaviour disorder. The pathogenic process that causes PD is presumed to be underway during the premotor phase, even more for more than 20 years, and involves regions of the peripheral and central nervous system in addition to the dopaminergic neurons of the SNpc (Samii et al., 2004, Kalia and Lang, 2015).

Progression of PD is characterised by worsening of motor features, which initially can be managed with symptomatic therapies. However, as the disease advances, there is an emergence of complications related to long-term treatment, including motor and non-motor fluctuations, dyskinesia, and psychosis. In late-stages, treatment-resistant motor and non-motor features are prominent and include axial motor symptoms such as postural instability, freezing of gait, falls, dysphagia, and speech dysfunction. After about 20 years of disease, up to 80% of patients with PD have freezing of gait, falls, and dementia. Autonomic symptoms, such as urinary incontinence, constipation, and postural hypotension, are also common in late stages (Samii et al., 2004, Kalia and Lang, 2015).
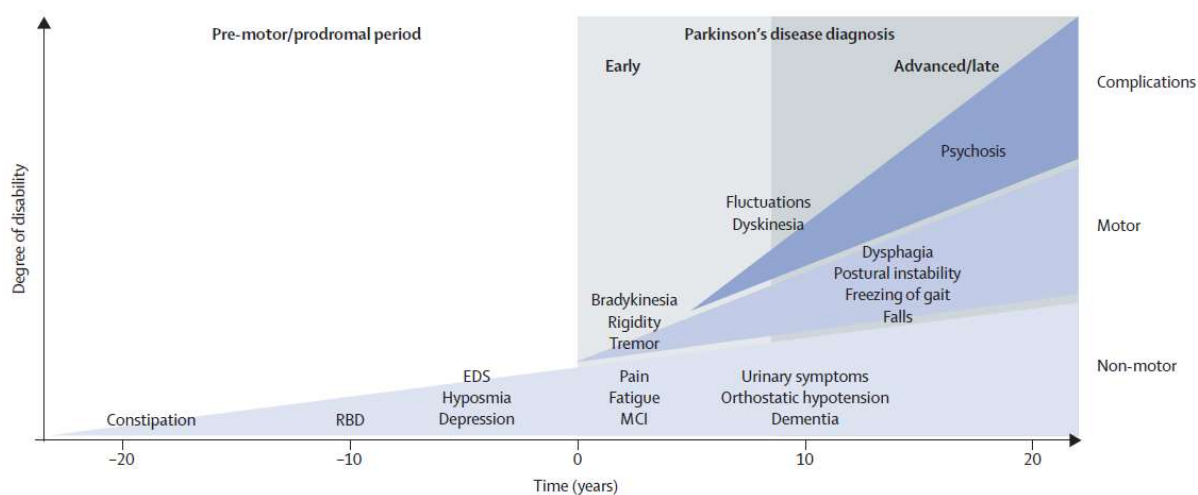
Figure 1. Clinical symptoms and time course of Parkinson's disease progression. Diagnosis of Parkinson's disease occurs with the onset of motor symptoms (time 0 years) but can be preceded by a prodromal phase of 20 years or more. As disease advances, axial motor symptoms, such as postural instability, falls and freezing of gait, drug-complications such as dyskinesias, and additional non-motor features tend to develop and contribute to disability. EDS=excessive daytime sleepiness. MCI=mild cognitive impairment. RBD=REM sleep behaviour disorder. Adapted from Kalia and Lang, 2015.

The etiopathogenesis of PD still remains unclear, but the current thinking is that the disease develops from a complicated interplay of risk factors, including demographics, environment and genetics.

Together with ageing, ethnicity and gender are also established risk factors, being approximately 3:2 the male-to-female ratio for example. Meta-analysis studies have found a variety of environmental factors to be associated with an increased risk of PD, including pesticide exposure, prior head injury, rural living, β-blocker use, agricultural occupation, and well-water drinking. It has been found also protective environmental factors such as tobacco smoking, coffee drinking, non-steroidal anti-inflammatory drug use, calcium channel blocker use, and alcohol consumption. The contribution of genetics to PD is suggested by the increased risk of disease associated with a family history of PD or tremor. The first monogenic form of PD identified was *SNCA*, which encodes the protein α-synuclein, and which led to the identification of α-synuclein as the major component of Lewy bodies and neurites. Mutations in this gene are rare and associated with autosomal dominant inheritance of parkinsonism. Mutations in *LRRK2* and *parkin* are the most frequent causes of dominantly and recessively inherited PD, respectively. Another important risk gene is *GBA*, which encodes β-glucocerebrosidase, a lysosomal enzyme, and which is the greatest genetic risk factor for developing PD identified so far (odds ratio greater than 5). Besides, advances in genomics and bioinformatics have uncovered additional genetic risk factors. In the past decade, almost 900 genetic association studies have implicated dozens of potential gene loci (Kalia and Lang, 2015).

Thus, in summary, PD is now viewed as a slowly progressive neurodegenerative disorder that begins years before diagnosis can be made, implicates multiple neuroanatomical areas, results from a combination of genetic and environmental factors, and manifests with a broad range of symptoms (motor and non-motor).
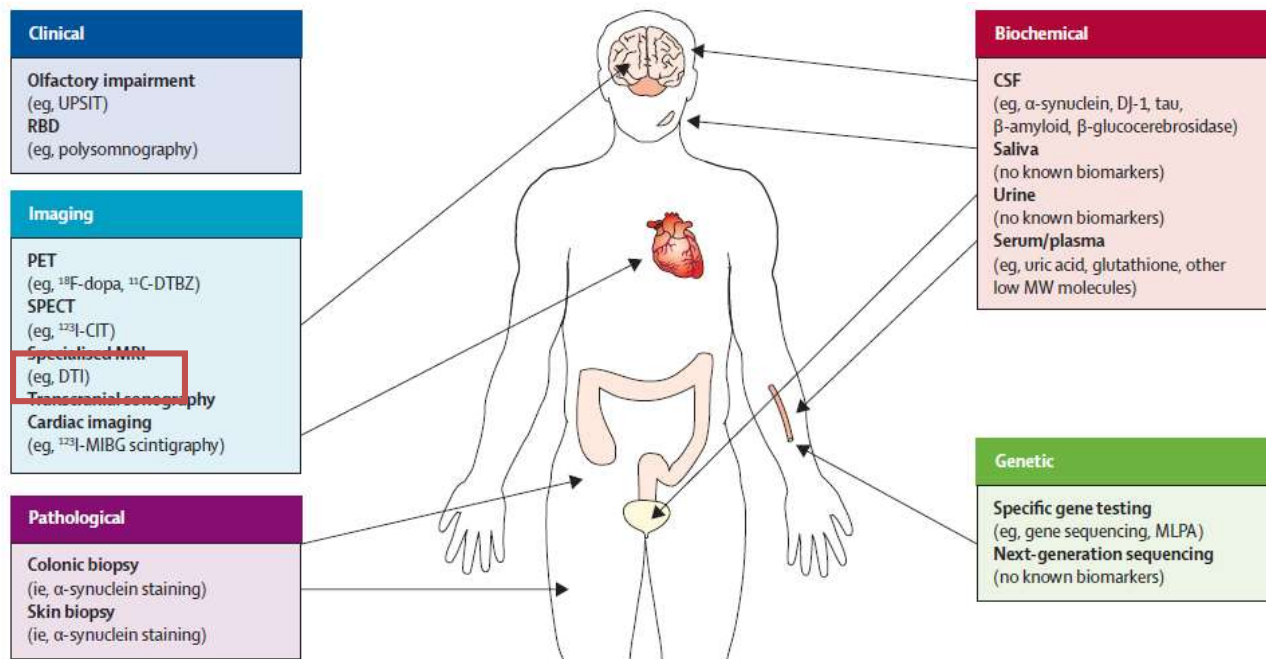
Diagnosis

The gold standard for diagnosis of PD still relies on post-mortem pathological examination. This is characterized by the presence of degeneration in the SNpc and Lewy pathology. Lewy pathology consists of abnormal aggregates of α-synuclein protein, called Lewy bodies and Lewy neurites.

In clinical practice, the diagnosis of PD is primarily based on the presence of parkinsonian motor features, namely bradykinesia plus rigidity and resting tremor. The U.K. Parkinson Disease Society Brain Bank has well-defined this clinical diagnostic criteria, which provides a sensitivity as high as 90%. However, in early stages, if clinical symptoms are subtle, monosymptomatic (e.g., an isolated tremor), or equivocal, it may be difficult to establish the correct diagnosis. Indeed, diagnostic tests which allow for definitive diagnosis at early stages of the disease do not exist yet. Of primary importance is to differentiate PD (and other neurodegenerative parkinsonisms) from other non-neurodegenerative movement disorders with similar clinical presentation (eg, essential tremor, drug-induced parkinsonism, psychogenic parkinsonism, etc) (Hughes et al., 2002).

A variety of biomarkers for rapid and accurate PD diagnosis are currently under investigation. These biomarkers different nature including clinical, imaging, pathological, biochemical, and genetic.

Potential clinical markers include olfactory impairment and rapid eye movement sleep behaviour disorder diagnosed by polysomnography. Pathological markers are being tested such as phosphorylated α-synuclein in both somatic and autonomic nerve fibres, and positive staining for α-synuclein in colonic biopsy tissue. Biochemial markers under study include concentration of α-synuclein, DJ-1, tau, and β-amyloid, as well as activity of β-glucocerebrosidase in cerebrospinal fluid (CSF). However, none of them has been established as an accurate biomarker yet, and some of them are too invasive to be rutinely used in risk individuals (Kalia and Lang, 2015).


Figure 2. Potential biomarkers for diagnosis of Parkinson's disease. These biomarkers can be classified as clinical, imaging, pathological, biochemical, and genetic. Combinations of biomarkers are likely to be necessary for accurate diagnosis of premotor or early PD. Adapted from Kalia and Lang, 2015.

Brain Imaging techniques are widely used for diagnosis since allow to **non-invasively** assess *in-vivo* the state of the brain circuitry. In PD and neurodegenerative parkinsonisms, the dopaminergic system plays a pivotal role and nuclear imaging of this pathway is an accurate biomarker of nigral degeneration. **Dopamine dysfunction** can be assessed using different molecular targets in the dopaminergic synapse with either **PET or SPECT**. Several options are available, but the most widely used approach is to assess the state of the presynaptic terminals with the dopamine transporter (DAT) imaging. The immediate advantage of this test is that is minimally invasive, however, the main disadvantagde is the lack of specificity with other parkinsonisms. One of the strong hypothesis and objective of this thesis is to improve this specificity with advanced computational image processing methods.

Dopamine transporter imaging

The nigrostriatal dopaminergic pathway can be analyzed at the striatal level, where the nigrostriatal neurons end and connect to the postsynaptic neurons using dopamine as the neurotransmitter. DATs are located at the presynaptic nerve terminals and are responsible for reuptake of dopamine from the synaptic cleft; thus, DAT imaging allow *in vivo* assessment of the integrity of presynaptic nerve terminals (Figure 1).
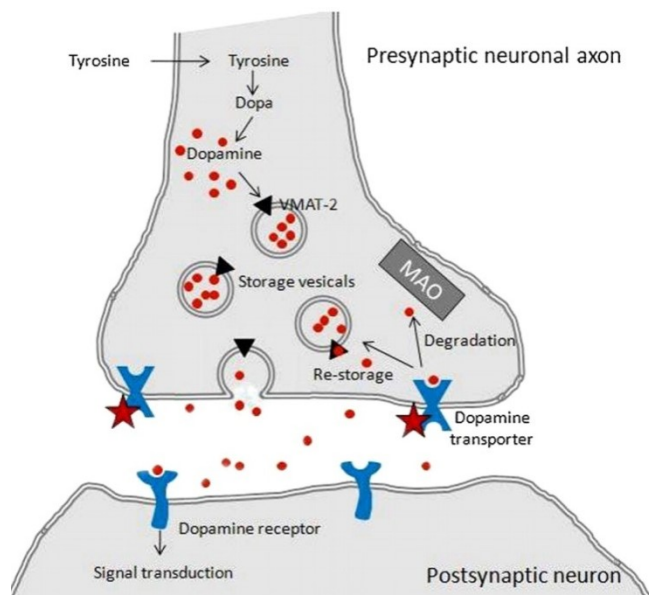
Figure 1. Schematic of striatal dopaminergic synapse (star indicates where ^{123}I-ioflupane binds). Adapted from (Djang et al., 2012).

The cocaine derivative 123I-labelled 2β-carbomethoxy-3β-(4-iodophenyl)-N-(3-fluoropropyl) nortropane (^{123}I-FP-CIT or ^{123}I-ioflupane) is a molecular imaging agent that binds to the DATs. ^{123}I-FP-CIT is stable 3–6 h after its i.v. administration and best imaged 3–4 h post-injection achieving high specific binding to the striatum compared to the rest of the brain parenchyma. The above characteristics make ^{123}I-FP-CIT SPECT (or DAT SPECT) ideal for clinical use.

^{123}I-FP-CIT SPECT was approved by the European Medicines Agency and available in Europe in 2000 and by the Food and Drug Administration In the United States on January 2011. Technical aspects of imaging such as the appropriate use of imaging devices, optimization of acquisition and processing parameters, and suggestions for further data analyses including quantification are dealt with in procedural guidelines published by the European Association of Nuclear Medicine and the Society of Nuclear Medicine and Molecular Imaging (Djang et al., 2012).

Image quantification

It is estimated that PD patient start manifestating motor symptoms after (the earliest) 50% or more of the nigrostriatal neurons have been lost. Hence, by the time the patient step by the clinic the nigrostriatal pathway is already severely degenerated.

The DAT SPECT image consists of a high intensity specific region, i.e. the striatum, where DAT is highly expressed, surronded by a lower intensity non-specific region, i.e. the rest of the brain, where DAT is non-significantly expressed. The SPECT images of normal volunteers and patients suffering from ET show similar uptake in the caudate nucleus and putamen with the striatum presenting as "comma-shaped" (Figure 2A). In parkinsonian syndromes, striatal DAT concentrations are and in severe cases the affected striatum loses the comma shape and becomes "point-like" (Figure 2B). PD is commonly clinically asymmetrical, and accordingly, the reduced uptake is more pronounced in the contralateral side of the one which suffers from the heavier movement disorder symptoms (Badiavas et al., 2011).
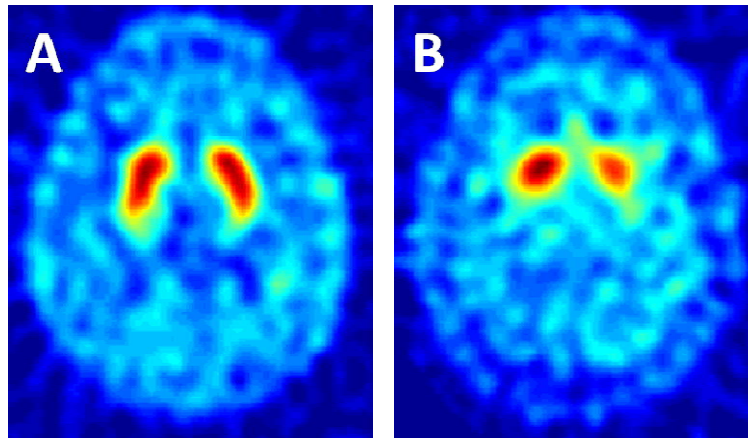
Figure 2. Axial view of a DAT SPECT image from a healthy control (A) and a Parkinson's disease patient (B).

In clinical practice, DAT SPECT is commonly assessed either visually (presence or not of nigral degeneration) or through striatal regional (putamen and caudate) DAT quantification with dedicated software packages. Visual assessment depends heavily on the observer's experience and naturally shows inter- and intra-observer variability, dictating the need for quantification to substantiate the diagnosis. Thus, quantification of regions of interests (ROI) is preferred and is usually performed by the calculation of the so-called binding potential or specific/nonspecific striatal binding ratio (SBR) (Badiavas et al., 2011).

$$SBR_{ROI} = \frac{C_{ROI} - C_{NSB}}{C_{NSB}}$$

where C_{ROI} is the count per voxel in the volume of interest and C_{NSB} denotes the mean count per voxel in the non-specific binding region. The occipital cortex is usually selected as the non-specific region because the density of DAT is negligible in this brain area.

The SBR is widely used in the literature for intensity normalization purposes in ^{123}I-FP-CIT SPECT images and also in other functional brain image modalities. However, the SBR value is sensitive to many factors including: i) deviced-related such as scanner hardware and acquisition protocol; ii) physiological-related such as sex, age and metabolism; and iii) operator-related such as the delineation of the ROIs. An illustrative example of this problem is shown in Table 1 with data derived from the European FP-CIT SPECT healthy controls database (Varrone et al., 2013). In this example it can be noted that controls have significantly different mean SBR values in different sites. The mean SBR in Leipzig is 2.75 whereas in Copenhagen is 3.95. Hence, SBR is not a good strategy for data hamonisation and results can be biased when working with different group of subjects and a large number of scans.

Imaging site	Right caudate	Right putamen	Left caudate	Left putamen
Copenhagen	3.95±0.61*	3.63±0.69*	3.87±0.69*	3.65±0.65*
Leipzig	2.75±0.43	2.57±0.20	2.77±0.44	2.43±0.27
Leuven	3.03±0.37	2.78±0.46	2.86±0.46	2.72±0.44
Munich	3.25±0.54	3.08±0.46	3.18±0.51	3.03±0.44
Stockholm	3.09±0.60	3.00±0.57	3.17±0.52	2.93±0.50
Yvoir	2.92±0.61	2.68±0.41	2.87±0.47	2.79±0.41

Table 1. Multi-site striatal binding ratio values from the European healthy controls database.

As we shall see in the last work of this thesis (work 5), this bias with improved intensity normalization methods. In this work, entitled "**Probabilistic intensity normalization of dopamine SPECT images via Variational mixture of Gamma distributions**", we aimed at developing an intensity normalization method for SPECT images to address SBR limitations.

Basal ganglia circuits and their relation with symptoms

The manifestation of symptoms and progression in PD is closely related to the affected connections between the basal ganglia and the cortex (cortico-basal ganglia-thalamocortical circuits) throughout the disease course (Obeso et al., 2002, Rodriguez-Oroz et al., 2009). In parkinsonian syndromes, dopamine depletion can be first observed in this scan in the putamen, which affects the connection with the motor cortex (Figure 3). Indeed, cumulated evidence has shown the correlation between the motor symptoms and putaminal dopamine. Dopamine depletion in the caudate usually occurs in later stages, affecting two well-defined frontostriatal loops: the associative and the limbic circuits (de la Fuente-Fernandez, 2013). The associative circuit connects the dorsolateral prefrontal cortex with the dorsal caudate nucleus. Therefore, the integrity of this latter pathway is essential to correct cognitive functioning, and a large number of studies have in fact found a correlation between cognitive performance (including executive and working memory tasks) and caudate dopamine levels in PD (Brooks and Piccini, 2006). The limbic circuit include connections between the orbitofrontal cortex and the ventral caudate nucleus, and between the anterior cingulate cortex and the nucleus accumbens and is related to emotions and mood states. Also, there are studies showing the relationship between déficits in the ventral striatum and mood and neuropsychiatric disorders such as depression, anxiety, visual hallucinations and impulse control disorders (Kiferle et al., 2014, Vriend et al., 2014a, Vriend et al., 2014b).
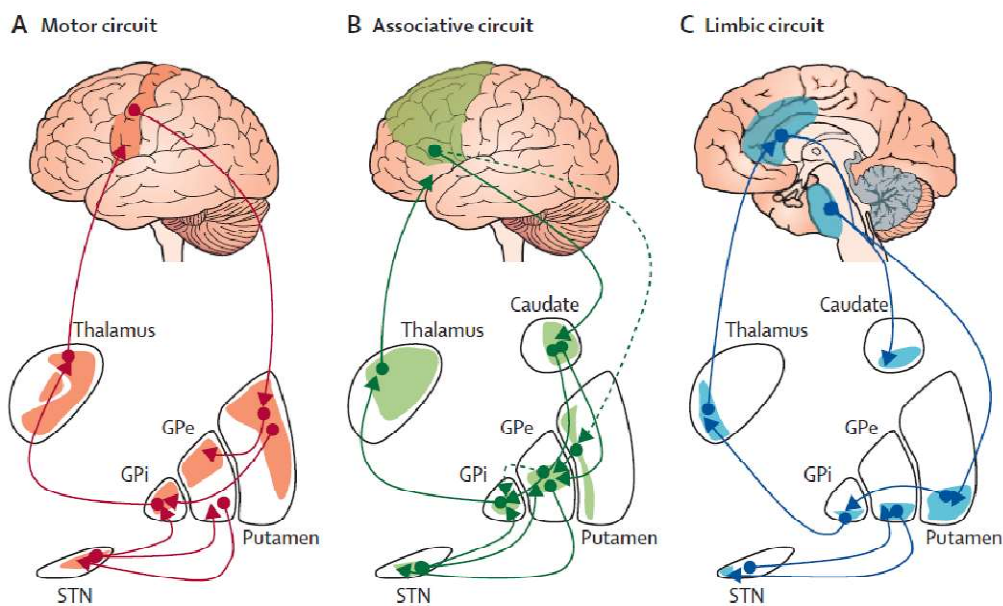
Figure 3. Functional organisation of the basal ganglia. The basal ganglia are divided into motor (A), associative (B), and limbic (C) subregions, which are topographically segregated, as highlighted by areas coloured in red (motor cortex), green (prefrontal cortex), and blue (anterior cingulate cortex). GPe=globus pallidus pars externa. GPi=globus pallidus pars interna. STN=subthalamic nucleus. Adapted from Rodriguez-Oroz et al., 2009.

Dopamine depletion and motor symptoms

The classical motor symptoms of PD include bradykinesia, muscular rigidity, rest tremor, and postural and gait impairment. Yet, not all PD patients present with the same motor symptoms, which has prompted attempts to classify subtypes of the disease based on the motor phenotype. A consensus on the classification of PD subtypes has not yet been established, but empirical clinical observations suggest two major subtypes: tremor-dominant (with a relative absence of other motor symptoms) and non-tremor-dominant PD (which includes phenotypes described as akinetic-rigid syndrome and postural instability gait disorder). An additional subgroup of patients has a mixed or indetermediate phenotype with several motor symptoms of comparable severity. Course and prognosis of disease differ between the subtypes; tremor-dominant PD is often associated with a slower rate of progression and less functional disability than non-tremor-dominant PD, including lower risk of cognitive impairment. Furthermore, the various subtypes are hypothesized to have distinct aetiologies and pathogenesis (Jankovic et al., 1990, Foltynie et al., 2002).

Distinctions are made between motor symptoms at presentation of the disease and the symptom dominance as the disease progresses, since some patients suffering from tremor at presentation become predominantly bradykinetic or rigid later in the disease. Hence, a fundamental and unsolved question is to elucidate which are the mechanisms underlying and driving the PD subtypes during the disease course.

The role of uric acid in PD subtypes

In this thesis, we present a work entitled "**Lower levels of uric acid and striatal dopamine in non-tremor dominant Parkinson's disease subtype**". The aim of this work was to show that PD subtypes differ in their levels uric acid (UA) and striatal dopamine, and that these both biological measures are closely related.

In recent years, several groups have reported the correlation between decreased plasma UA levels and neuron cell failure in the substantia nigra, clinical progression and stage of PD. Conversely, high plasma UA concentrations in hyperuricemia may reduce the risk and delay the progression of PD (Ascherio et al., 2009, Schwarzschild et al., 2011, Ravina et al., 2012).

The molecular mechanisms giving explanation to these clinical observations are not fully understood but it is believed that are related to the antioxidant properties of UA, which offers protection to the cells against oxidative stress. Oxidative stress seems to play a key role in nigrostriatal degeneration. Dopaminergic neurons in the substantia nigra pars compacta have high levels of basal oxidative stress likely due to enzymatic and nonenzymatic oxidation of dopamine. This process is considered enhanced in PD due to early compensatory changes in dopamine turnover resulting from the initiation of nigral cell degeneration. Remarkably, markers of oxidative stress and damage were found to be present in dopaminergic neurons in the SN of postmortem brain of PD patients. Moreover, several PD-linked genes such as α-synuclein, DJ-1, PINK1, and Parkin have been demonstrated to interact with oxidative stress, and these interactions may contribute to the progressive neurodegeneration underlying PD (Chen et al., 2012).

Therefore we hypothesized and show that the differences in nigrostriatal degeneration across PD subtypes are accompanied by differences in their levels of UA and that these two measures

correlate. More specifically, non-tremor dominant show lower levels of UA and striatal DAT, thus explaining why they present with more severe symptoms. We hypothesize in this work that UA might be involved in the mechanisms underlying and driving PD subtypes.

Cognitive impairment and dementia

Cognitive impairment is another (and common) disabling symptom in PD and is now considered to be among the most important symptoms of perhaps the greatest clinical unmet need. Cognitive deficits may be present in up to 24% of PD patients by the time of diagnosis, and this rate reaches over 80% in the long-term (Aarsland et al., 2011). Importantly, PD dementia is a crucial determinant of reduced life expectancy in patients.

Cognitive impairment is also considered a heterogeneous entity in PD. Although dysexecutive syndrome has long been considered the main hallmark of cognitive decline in PD, deficits in visuospatial, memory and attention functions may be also present. The rate and pattern of these deficits vary greatly among PD patients, and different biological mechanisms appear to play a role. These include neuronal degeneration of different neurotransmission systems, including catecholaminergic (ie, dopamine and norepinephrine) and cholinergic (acetylcholine) (Robbins and Cools, 2014).

In this regard, the dual syndrome hypothesis was recently proposed, suggesting two facets of cognitive decline in PD: (i) changes in frontostriatal dopaminergic transmission, leading to deficits in planning, working memory, response inhibition and attentional control; and (ii) posterior cortical Lewy body pathology and secondary cholinergic loss, affecting visuospatial, mnemonic and semantic functions and leading to dementia (Kehagia et al., 2013).

As for the development of PD itself, **some genetic factors have been described as risk factors for cognitive impairment and dementia in PD**. The early identification of these risk factors will allow to to adequately manage patients in early stages and tailor treatments to minimize and/or delay this cumbersome symptom. Furthermore, elucidating the contribution of these factors may provide new insights into the biological mechanisms underlying the different forms of cognitive deficits in PD.

Some studies have focused on α-synuclein and tau, which might be involved in this process, suggesting that common variation in both the **SNCA** (α-synuclein) and the **MAPT** (microtubule associated protein tau) H1 haplotype might not only aff ect susceptibility to sporadic PD, but also affect the rate of cognitive decline and PD dementia. Also, it is widely known that **APOE** (apolipoprotein E) e4 allele confers risk for cognitive impairment, particularly in Alzheimer's disease, and predicts cholinergic deficits. **COMT** (catechol-O-methyltransferase) encodes for a enzyme involved in the degradation of cortical dopamine and previous studies have shown that a variant in this gene modulates the dopamine levels in the frontostriatal network, and in turn, executive function performance. The glucocerebrosidase gene (**GBA**) is the most common genetic factor that has yet been identified for developing PD. PD patients with mutations in *GBA* have earlier disease onset, and are at a higher risk of developing visual hallucinations, cognitive impairment and dementia (Mollenhauer et al., 2014).

In this thesis, we present a work entitled "**Genetic factors influencing frontostriatal dysfunction and the development of dementia in Parkinson's disease**". The aim of this work was to study the contribution to the dual syndromes of cognitive impairment (frontostriatal dopamine-mediated and posterior cortical leading to dementia) of the main genetic risk factors decribed in the literature: *GBA*, *MAPT*, *APOE*, *SNCA* and *COMT*.

Other parkinsonisms

Although PD is the most common cause of parkinsonism, numerous other etiologies can lead to a similar set of parkinsonian symptoms (bradykinesia, rigidity, tremor at rest, and postural instability), thus making the differential diagnosis quite challenging, especially at early stages.

Parkinsonism is a syndromal umbrella term that comprises 4 etiologically different entities: idiopathic Parkinson disease, familial parkinsonism, atypical parkinsonims (caused by other neurodegenerative diseases), and secondary parkinsonism, including common differential diagnoses such as specific tremor syndromes. The group of atypical parkinsonisms includes multiple system atrophy (parkinsonian and cerebellar types), progressive supranuclear palsy, corticobasal degeneration, spinocerebellar atrophy, and dementia with Lewy bodies. Vascular, drug-induced, toxic, and metabolic parkinsonism; parkinsonism associated with inflammation, trauma, and tumor; and normal-pressure hydrocephalus belong to the category of secondary parkinsonism. Essential tremor and other tremor syndromes are further common differential diagnoses additional to PD and atypical parkinsonisms.

DAT imaging helps in this challenging task of differential diagnosis, especially between movement disorders with nigral degeneration and movement disorders without nigral degeneration. DAT concentrations are lower in presynaptic disorders, which include PD and other neurodegenerative parkinsonisms such as multiple system atrophy, progressive supranuclear palsy, and dementia with Lewy bodies (Booij et al., 2012). Conversely, DAT concentrations will generally be normal in parkinsonism without presynaptic dopaminergic loss, which includes essential tremor, drug-induced parkinsonism, and psychogenic parkinsonism. For this reason, DAT SPECT is frequently used in clinical practice to distinguish between more benign syndromes such as essential tremor or drug-induced parkinsonism and more aggressive neurodegenerative disorders such as PD or atypical parkinsonisms (Tatsch and Poepperl, 2013).

Secondary parkinsonism: vascular parkinsonism

The pattern seen in DAT SPECT in other forms of parkinsonism such as vascular parkinsonism (VP) is less clear and a matter of debate. Reports on DAT binding in VP provide heterogeneous results, which might indicate that VP is a mixed entity that is not yet well characterized. Some authors have reported normal or only a slight but insignificant reduction of DAT binding in patients with suspected VP; others have found significantly reduced binding values (Antonini et al., 2012, Navarro-Otano et al., 2014). There is consent that DAT binding is reduced in striatal subregions directly affected by infarction, as demonstrated by structural defects in corresponding anatomical imaging examinations (Zijlmans et al., 2007). In 2012, we published a work where we developed a visual scale able to distinguish vascular parkinsonism from PD with 94% accuracy (Benitez-Rivero et

al., 2013). This scale consisted in four imaging patterns, three corresponging to VP and one more charasteristic in PD (Figure 4). Nuclear medicine experts were able to visually identify these patterns and making a differential diagnosis solely based on the scan.
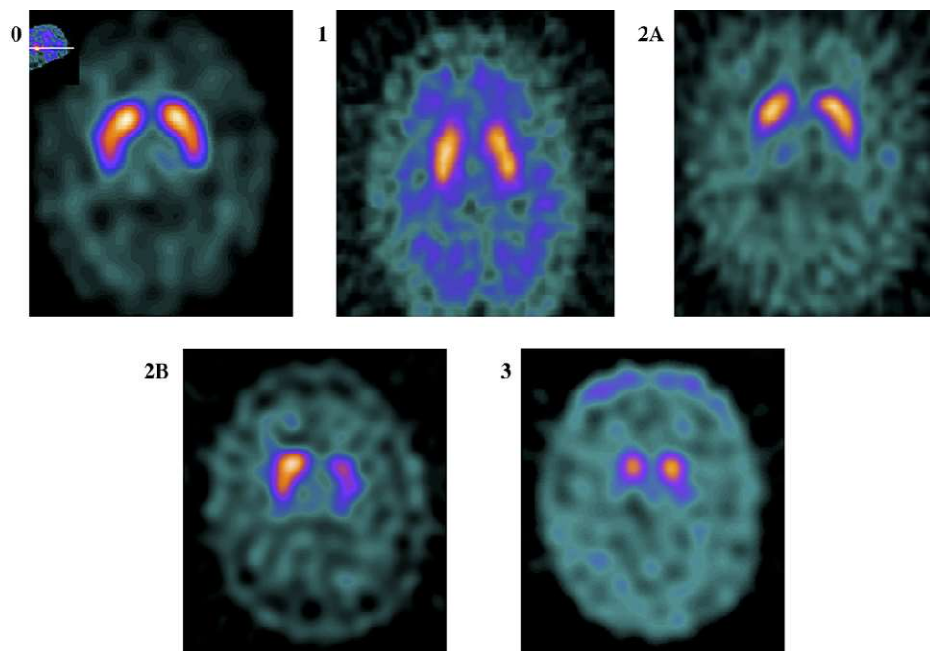
Figure 4. Visual scale to distinguish between vascular parkinsonism and Parkinson's disease. Patterns: 0. Bilateral normal uptake. 1. Mild or moderate homogeneous and bilateral decreased striatal uptake. 2. Focal deficit of tracer accumulation on any striatal region (A) or homogeneous unilateral striatal diminished uptake (B). 3. Symmetric or asymmetric striatal reduced uptake, more pronounced in putamen than in caudate, showing a rostrocaudal gradient, with or without other irregular associated defects. Adapted from (Benitez-Rivero et al., 2013).

Despite this good accuracy in the differential diagnosis and very good inter-rater agreement (Cohen's k = 0.83), visual scoring methods have important limitations such as the dependence on the rater. In this case, the two raters belonged to the same center and had the same training. ROI and voxel-based analyses can much better exploit the information content in the image to provide more objective estimates and generalizable to other centers. The number of voxels depends on several parameters including the type of image and scanner resolution, but a brain image can contain over 90,000 voxels. Hence, the analysis of these images are usually performed with computational image processing software packages, such as Statistical Parametric Mapping (SPM, run in Matlab) or FMRIB Software Library (FSL). The recognition of patterns in these images and construction of models for making inferences (including diagnosis) require the use of advanced statistical techniques that few years ago gave birth to a now established and promising field of research (see section Pattern Recognition and Machine Learning in brain imaging).

In this thesis, we present a work entitled "**Machine learning models for the differential diagnosis of vascular parkinsonism and Parkinson's disease using [123I]FP-CIT SPECT**". The aim of this work was to develop diagnostic models using data from two rater-independent DAT SPECT assessment methods: Striatal ROI and whole-brain voxel-based analyses.

Atypical parkinsonism

Current knowledge and state-of-the-art in the analysis of DAT SPECT do not allow to differentiate between PD and atypical parkinsonisms with accuracy. However, some studies have shown group-level statistical differences in DAT imaging among these parkinsonisms, and more in particular by assessing the ligand uptake in striatal subregions (Oh et al., 2012) (see subregions in Appendix). These findings have shed light on the possibility of aiding the diagnosis of these syndromes with this widely used scan. We have also investigated the use of voxel-based pattern recognition approaches to aid the differential diagnosis of PD and atypical parkinsonisms.

Pattern recognition and machine learning in brain imaging

Pattern recognition is a field within the area of machine learning (ML), which is concerned with automatic discovery of regularities in data through the use of computer algorithms, and with the use of these regularities to take actions such as classifying the data into different categories (eg, making diagnosis with classifiers) or finding correspondence between an anatomical or functional substrates in the brain and a phenotypic variable (regression with a quantitative measure). Pattern recognition aims to predict disease state at the single-subject level based on distributed patterns of anatomical/functional abnormality and is being increasingly applied in clinical neuroimaging studies. Classification algorithms have been applied to diagnose a wide range of neurological and psychiatric disorders (Orru et al., 2012, Zarogianni et al., 2013). In the context of this thesis, we aimed at identifying patterns in neuroimaging data to develop classifiers able to categorize subjects according to their most probable diagnosis.

Machine learning pipeline overview

In supervised machine learning, the basic scenario consists of a **training sample**, a **test sample** and a function – the **classifier** – to be learnt and tested.

A classifier is a function that takes the values of the features or independent variables (eg, voxels in a certain ROI or whole-brain) in an example and predicts the class or dependent variable (eg, diagnosis) that that example belongs to. The classifier function has a number of parameters that have to be learned from the training data, in order to model the inherent relationships between the features and the class label. **Feature selection** techniques can be used to select the most informative/discriminative features to feed the classifier. Once trained, these relationships (and its accuracy) can be tested by using the learned classifier on a different set of examples, the test data. Intuitively, the idea is that, if the classifier truly captured the relationship between features and classes, it ought to be able to predict the classes of examples it hasn't seen before. Very importantly, the testing set should not include instances of the training set to avoid circularity or data overfitting (Pereira et al., 2009).

Cross-validation techniques can be used to avoid splitting the whole sample in two independent datasets and thus loosing statistical power. In k-fold cross validation, the original data set is split into k non-overlapping sets and then the algorithm is trained using k − 1 subsets and the left-out set

is used in the testing phase. The procedure is repeated k times, so that every subgroup is used in the testing phase (Pereira et al., 2009).

The evaluation of **classification performance** usually includes measures such as sensitivity, specificity and accuracy. Sensitivity refers to the proportion of actual positive cases correctly identified and is computed by the TP / (TP + FN), where TP is the number of true positives and FN is the number of false negatives. Specificity refers to the proportion of the negatives cases correctly classified (e.g. healthy controls correctly identified as being healthy) and is computed by the amount TN / (TN + FP), where TN is the number of true negatives and FP is the number of false positives. Accuracy refers to the overall amount of correct classifications across the groups and is computed by TP + TN / TP + TN + FN + FP, or by the amount of (sensitivity + specificity) / 2, if the classes are balanced (Zarogianni et al., 2013).
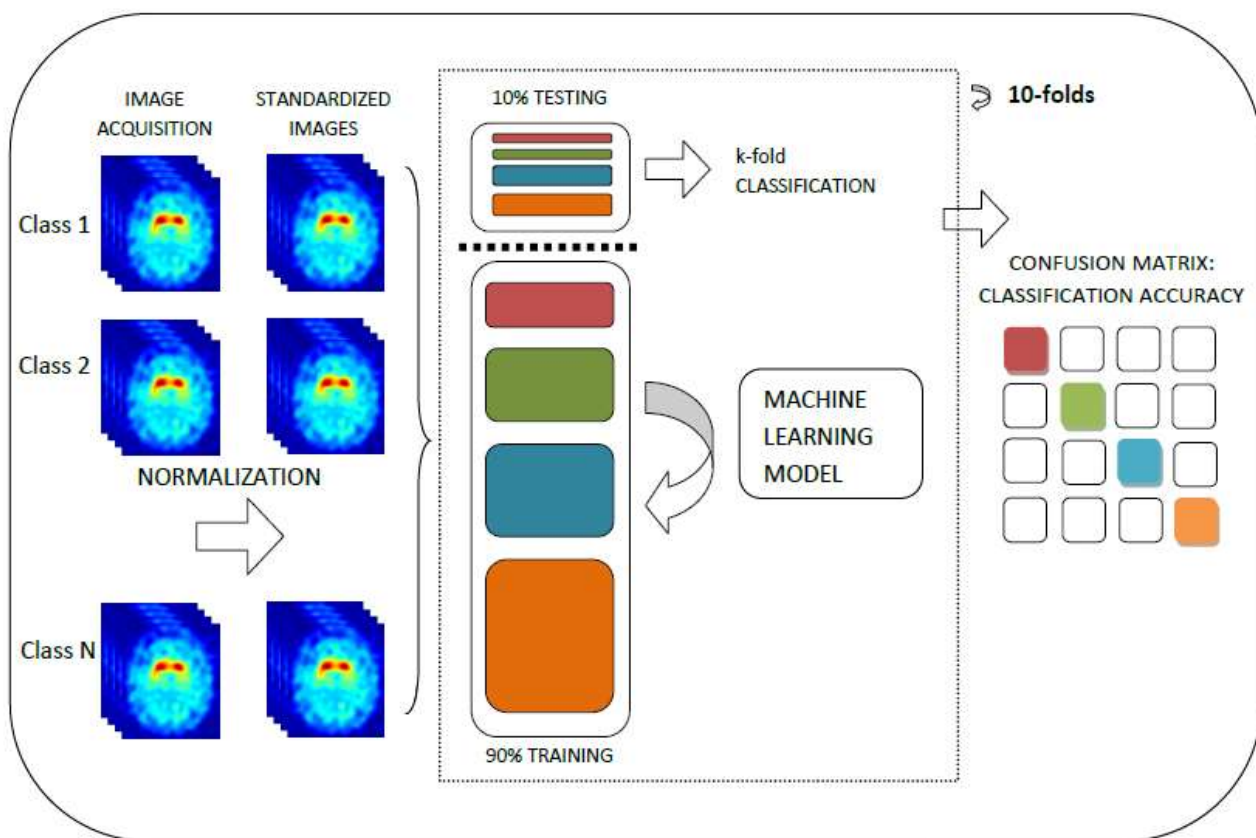
Figure 5. Machine learning pipeline in neuroimaging. Brain scans are first pre-processed using standard methods. A machine learning engine will attempt to find the function that minimizes classification error. A cross-validation scheme can be used to enhance power while avoiding overfitting.

In these machine learning scenarios we generally have many more features (i.e., voxels) than samples (images) (p>>N). One common pitfall in machine learning, and especially when dealing with high dimensions like in neuroimaging, is the phenomenon called overfitting. **Overfitting** will occur if the function that we find for the classifier in the training set does not generalize to the test set. Risk factors for overfitting include small sample sizes, unadequate training/test set balance and function complexity. Normally, the best performance in the test set is achieved by finding the optimal tradeoff point between model complexity and performance in the training set.

Machine learning with basis functions

In the more simplistic approach for ML, for example a linear regression, the goal is to find a function $\mathbf{y}$ of the input variables $\mathbf{x}$ to best approximate a set of output variables $\mathbf{t}$. Given a training data set comprising N observations $\{x_n\}$, where n = 1, …, N, in a input space of dimension D (number of voxels) together with corresponding target values $\{t_n\}$. The goal is to predict the value of t for a new value of x. In the simplest approach, this can be done by directly constructing an appropriate function $\mathbf{y}(\mathbf{x})$ whose values for new inputs $\mathbf{x}$ constitute the predictions for the corresponding values of $\mathbf{t}$ (Bishop, 2006).

In a linear regression model, the target function $\mathbf{y}$ can be as a linear combination of the input variables $\mathbf{x}$:

$$\mathbf{y}(\mathbf{x}, \mathbf{w}) = w_0 + w_1 x_1 + \cdots + w_D x_D$$

where $\mathbf{w}$ denotes the vector of weights (coefficients, parameters). The key property of this model is that it is a linear function of the parameters $w_0, \ldots, w_D$. It is also, however, a linear function of the input variables x_i, and this imposes significant limitations on the model. In ML it is convenient, especially in high-dimensions problems like in neuroimaging, to project the native feature input space into a new nonlinear feature space with the use of nonlinear basis functions $\boldsymbol{\phi}(x)$.

The target function $\mathbf{y}$ can therefore be expressed as a linear combination of M (M<<D) basis functions $\{\boldsymbol{\phi}_m(x)\}_{m=1}^{M}$:

$$\mathbf{y} = \sum_{m=1}^{M} w_m \boldsymbol{\phi}_m(\mathbf{x})$$

By using nonlinear basis functions, we allow the function $\mathbf{y}(\mathbf{x}, \mathbf{w})$ to be a nonlinear function of the input vector x although linear in the parameters w. This linearity in the parameters will greatly simplify the analysis of this class of models. This is the concept behind many ML methods for high-dimensions and these functions are called **kernels**. Kernels are functions that allow a mapping of the original, non-linearly separable data into a new feature space where the data are linearly separable (Figure 7). The concept of a kernel formulated as an inner product in a feature space allows us to build interesting extensions of many well-known algorithms by making use of the **kernel trick**, also known as kernel substitution. The general idea is that, if we have an algorithm formulated in such a way that the input vector x enters only in the form of scalar products, then we can replace that scalar product with some other choice of kernel (Bishop, 2006).

ϕ

Input Space   Feature Space
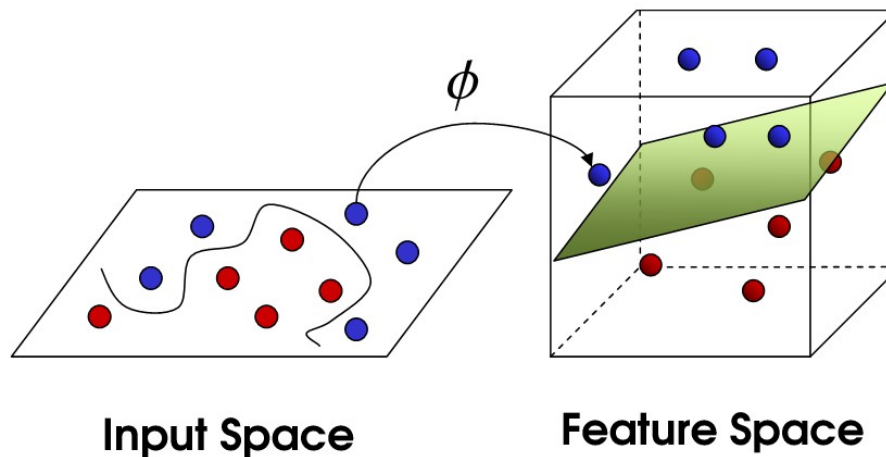
Figure 7. Graphical representation of the kernel trick. A non-linear function ϕ is applied to a non-linearly separable input space in R^2 so that is linearly separable in a new feature space of higher dimension R^3.

On top of this scenario, a pletora of ML methods have been built using an endless variety of statistical tricks and techniques. A binary classifier can logistic regression by simply letting y = {0,1} and taking the logit function of y.

A kernel is a function given by the relation:

$$k(x, x') = \phi^T(x)\phi(x')$$

The simplest example of a kernel function is obtained by considering the identity mapping for the feature space so that $\phi(x) = x$, in which case $k(x, x') = x^T x$. We shall refer to this as the linear kernel. There are numerous forms of kernel functions: polynomial, Gaussian and radial basis function (RBF) are some of the most commonly used basis functions. For example, a RBF has the form:

$$\phi(x) = exp\left\{\frac{(x - \mu)^2}{2s^2}\right\}$$

where μ represents the mean and s the standard deviation.

One important aspect of kernel ML methods is the selection of type, form and number of basis functions. For example, if we assume that the basis functions $\phi(x)$ are fixed before the training data set is observed, the number of basis functions may needs to grow rapidly, often exponentially, with the dimensionality D of the input space, which can lead to curse of dimensionality problems.

Popular machine learning methods in brain imaging

There are few widely used ML methods in the field of neuroimaging, including both discriminative models such as Support Vector Machines and Linear Discriminant Analysis and probabilistic models such as Relevance Vector Machines and Gaussian Processes.

Support Vector Machines (SVM) is one of the most popular methods, partly because it can deal effectively with high-dimensional data and provide good classification results. SVM are a family of kernel-based algorithms that have sparse solutions so that predictions for new inputs depend only on the kernel function evaluated at a subset of the training data points. Hence, these methods address the limitation of other kernel algorithms for which all possible pairs x_n and x_m of training points must be evaluated cand thus computation times may turn excessive.

The aim of a SVM classifier is to find a decision surface that would optimally distinguish between classes and based on that surface assign new, previously unseen data instances into the groups. In the training phase, the classifier computes the optimal decision surface expressed in the form $y(\mathbf{x}) = \mathbf{w}\mathbf{x} + b$ only by a subset of the original training set called the support vectors. Support vectors are data points that lie closest to the optimal separating hyperplane and hence are the most difficult patterns to classify (Figure 8). The optimal hyperplane is determined by maximizing the margin of separation between the two classes. The problem of finding the optimal hyperplane, thus, becomes an optimization problem.
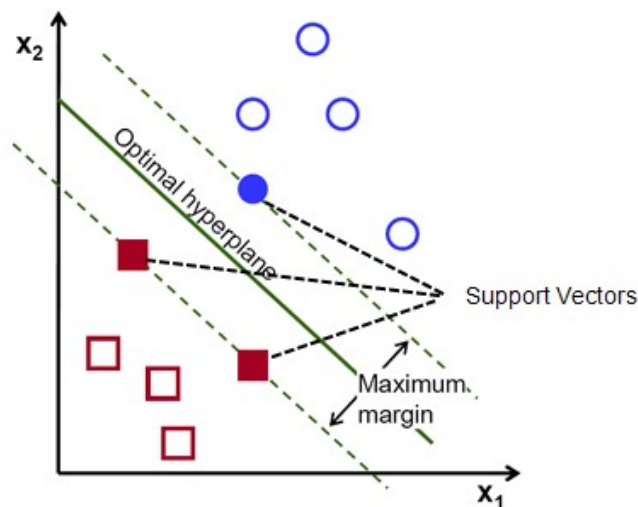
Figure 8. Binary Support Vector Machine classifier. The optimal hyperplane is determined by maximizing the margin of separation between the two clases according to the support vectors.

An important characteristic of the SVM algorithm is that it has a sparse representation, meaning that the hyperplane is specified by a subset of data samples (support vectors) and predictions are derived from support vectors only. However, all data dimensions are still required for prediction: **sparsity in SVM models refers to data samples, not features.** Furthermore, predictions in SVM are not probabilistic and thus limited to discrete categorical decisions (e.g. patient/control). However, in real life application quantitative predictions are desirable to accurately represent variability

within subject groups and uncertainity. For example, we have seen that some neurological disorders like PD are per se very heterogeneous regarding symptoms and disease progression. Therefore, ideally, all patients of this disease should not be clustered altogether with a same class label.

In this context, probabilistic models are different approaches for ML and may better reflect reality than discriminative models, since the uncertainty around a class label prediction is properly quantified. **Probabilistic ML** methods such as Relevance Vector Machines or Gaussian Processes have emerged as an alternative to SVM for prediction of high-dimensional data and are based on Bayesian theory. The conceptual foreground of Bayesian theory is completely different, as the notation and terminology are.

For example, in the probabilistic formulation of a simple linear regression (i.e., **Bayesian linear regression**) of the form $\mathbf{t} = \mathbf{y}(\mathbf{x}, \mathbf{w}) + \varepsilon$, where ε represents the noise, we aim to model a predictive distribution $\mathbf{p}(\mathbf{t}|\mathbf{x})$ to express our uncertainty about the value of $\mathbf{t}$ for each value of $\mathbf{x}$. From this conditional distribution we can make predictions of $\mathbf{t}$, for any new value of $\mathbf{x}$, in such a way as to minimize the expected value of a suitably chosen loss function.

Our objective is therefore to find values for $\mathbf{w}$ such that $\mathbf{y}(\mathbf{x}, \mathbf{w})$ makes good predictions for new data: i.e. to model the underlying generative function. We are interested in estimating a distribution for $\mathbf{w}$. To that end, we will assume a prior 'belief' on how is $\mathbf{w}$ **(prior distribution)**, and we will update this belief **(posterior distribution)** according to the observed data $\mathbf{t}$ **(likelihood)**, with more posterior probability assigned to values which are both probable under the prior and which 'explain the data' (Tipping, 2004).

In mathematical notation following the Bayes rule, and assuming Gaussian distributions for the prior and the likelihood functions, the posterior is equal to (see Tipping, 2004 for further details):

$$\text{posterior} = \frac{\text{likelihood} \times \text{prior}}{\text{normalizing factor}} = p(\mathbf{w}|\mathbf{t}, \mathbf{x}, \alpha, \beta) = \frac{p(t|x, w, \beta)p(w|\alpha)}{p(\mathbf{t}|\alpha, \beta)}$$

where α and β represent the precision (inverse variance) of the weights and the noise, respectively.

Generally, calculating the full posterior distribution involves computing intractable integrals and approximation methods are commonly used, such as Variational Bayes, Markov Chain Montercalo (MCMC), etc. Another common strategy is called maximum a posteriori (MAP), where the single most probable value under the posterior distribution of $\mathbf{w}$ is calculated instead. This latter method is considered a shortcut and not a "true Bayesian" approach (see Bishop, 2006).

The problem of univariate voxel-based methods

Most current approaches to neuroimaging take the basic spatial unit of analysis to be the voxel. Conventional voxel-wise analysis involve in Gaussian smoothing imaging data, independently fitting a statistical model to imaging data at each voxel, and generating statistical maps of test statistics and p-values. However, although this approach has been very effective, it suffers from some important shortcomings:

- **Voxel-based univariate methods do not properly account for the spatial properties of the image**. The assumption of independence between voxels in the general lineal model (GLM) is rarely true and therefore the spatial dependencies are disregarded.

- **The voxel is an unit of resolution, not an unit of computation of the brain**: modeling neural responses at the voxel level does not enable direct inferences about what are arguably the variables of real interest, the responses of the underlying neuroanatomical regions.

- This approach generates a **resolution-dependent mass amount of statistical estimates** that need to be dealt with complex post-hoc correction methods (Nichols, 2012). Thus, these methods may be suboptimal in statistical power and do not optimally benefit from new high-resolution acquisition protocols. This inefficiency may lead to equivocal error rates and therefore wrong conclusions in brain research and clinical applications (Eklund et al., 2016).

- The use of Gaussian smoothing can blur the image data near the edges of the spatially contiguous regions and thus introduce substantial bias in statistical results.

In the last years there have been efforts to develop multivariate approaches in order to overcome these issues. In neuroimaging, characterizing the spatial correlations among a large number of voxels, usually in the tens of thousands to millions, is tremendously challenging. Yet, such spatial correlation structure and variability are important for achieving better prediction accuracy, for increasing the sensitivity of signal detection, and for characterizing the random variability of imaging data across subjects. In this thesis we introduce and have worked with a multivariate approach based on the progresses made in the field of spatial statistics.

## Spatial statistics – an elegant multivariate approach

Spatial statistics is a developed field in geoscience, where characterizing the continous spatial dependencies of the earth with sensors in discrete point locations have been a big scientific matter in this science for a long time. The classical approach is the linear mixed model, in which an additional term, called spatial random effects ($\mathbf{h\alpha}$), is added to the GLM.

$$\mathbf{y} = \mathbf{xw} + \mathbf{h\alpha}$$

The covariance matrix of this term describes the spatial correlation between V locations, and the inversion of this V x V matrix is necessary to solve the equations (Wikle and Royle, 2002).

In 2008, Cressie and Johannesson developed a geostatistical model, termed Fixed Rank Kriging (FRK), in which the process of interest is modeled as a linear combination of basis functions plus a fine-scale variation term (Cressie and Johannesson, 2008). Spatial prediction using this method is then feasible even for very large number locations (up to a million or more), as long as the number of basis functions is much smaller (no more than a few thousand) than the number of observations. These basis functions can be nonlinear functions, such as RBF, b-splines, or wavelets that are placed all over the spatial domain. Typically, lengthscale parameters control the smoothness of the function and multiple resolutions are used so as to capture both short and long ranges of spatial dependencies (Figure 10). They provided some guidance about the requisites for the basis functions:

- It is recommended that the basis functions be of different resolutions, to capture different scales of spatial variation.
- Each resolution contains a group of basis functions with the same smoothness and range, but the range varies between resolutions. There are typically a few smooth basis functions with large support, and many "spiky" basis functions with small support.
- The locations of the basis functions within a resolution should ideally cover the entire spatial domain of interest, D, and the locations of the basis functions from two different resolutions should probably not be coincident.
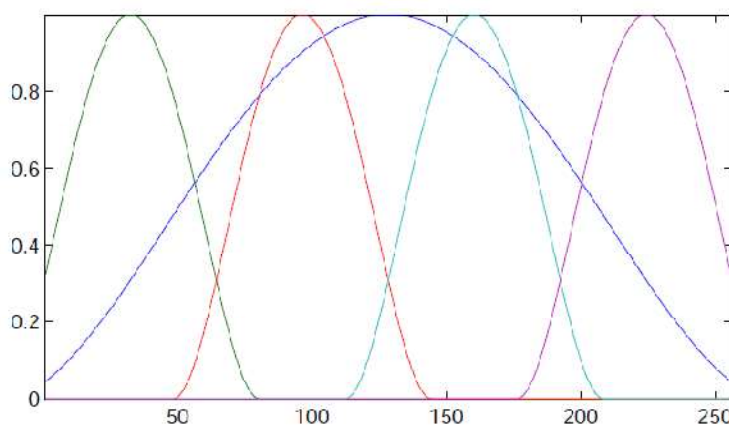
Figure 6. Multiresolutional Radial basis functions. Five one-dimensional RBF from two resolutions

Basis functions for brain imaging

We have already introduced in the previous section the use of basis functions for machine learning. There is a big fundamental question in neuroimaging machine learning though: which are the best form of basis functions to model a brain image?. Many options are possible, we have briefly mentioned above that there is a plethora of possible basis set to use such as RBF, b-splines or wavelets. Indeed, RBF are popular 3D computer modeling and some have made use to model brain images.

However, there are two fundamental problems if using generic kernels such as isotropic RBFs: How many basis functions should be used to properly cover a specific region or even the entire brain, and what are they representing biologically? Essentially, one would need to conduct a brute force approach comprising three steps: i) selecting an arbitrary number of resolutions and ranges; ii) placing a large number of RBF covering the spatial domain; and iii) running a heavy optimization machinery in order to minimize some error measure in fitting a given data set. Furthermore, the biological substrate of the relevant RBF(s) coming out may not cleanly map onto congruent biological sources (i.e. bran nuclei) and thus lead to misleading conclusions

The next work presented in this thesis is entitled **"A Bayesian spatial model for neuroimaging using multiscale functional parcellations"**. In this work we address these problems by introducing **a new family of spatial basis functions for neuroimaging** studies that more closely reflect the underlying biology. We have extracted a basis set of functions from high-quality resting state functional MRI. These are based on a novel **multiscale functional parcellation of the relevant brain regions** called Instantaneous Correlation Parcellation (ICP) (van Oort et al., 2016).

Multiscale functional parcellation of the brain

In this work we propose to use a soft hierarchical parcellation obtained from an advanced parcellation strategy known as **Instantaneous Connectivity Parcellation (ICP)** (van Oort et al., 2016). Our rationale is based on emerging evidence of temporally independent, spatially overlapping, subnetworks within anatomical regions and functional networks in the human brain (Smith et al., 2012). These subnetworks are believed to represent fine-scale units of computation used by the brain for processing and therefore correspond well with biology.

The ICP approach is ideally suited to derive from a brain region the underlying subnetworks, which we will use as basis functions. ICP will generate an adequate basis set of functions to our spatial statistics approach for three reasons:

- ICP sub-divides brain networks on the basis of fine-grained temporal similarities instead of temporally averaged correlations.
- ICP does not impose a spatial contiguity constraint, meaning that brain regions that are not spatially adjacent can still participate in the same subnetwork
- ICP follows a hierarchical top-down strategy for parcellation, which generates a set of parcels at different levels of granularity which allows us to model multiple resolutions of spatial dependencies in the image.

Instantaneous Correlation Parcellation

ICP is based on the assumption that voxels that form a subregion within a larger region of interest (ROI) exhibit similar, yet slightly different time courses compared to other voxels within the larger region. Accordingly, each subregion within this ROI could be identified by structured changes between the voxel-wise timeseries and thus has its own characteristic temporal signature. To enhance the identifiability of subregions, ICP selectively augments these subtle differences by the element-wise multiplication of the voxel-wise time courses with the average time course of the entire ROI. This process (called "temporal unfolding") results in instantaneous correlations and is illustrated in Figure 7. The instantaneous correlations are calculated separately for every fMRI dataset. Subsequently, group-level independent component analysis (Beckmann and Smith, 2004), a data-driven multivariate analyses technique, is applied to these transformed time courses. ICA will divide the ROI into subregions (i.e., components) by grouping voxels with similar timeseries, thus segregating voxels with different instantaneous correlations (Oldehinkel et al., 2016).
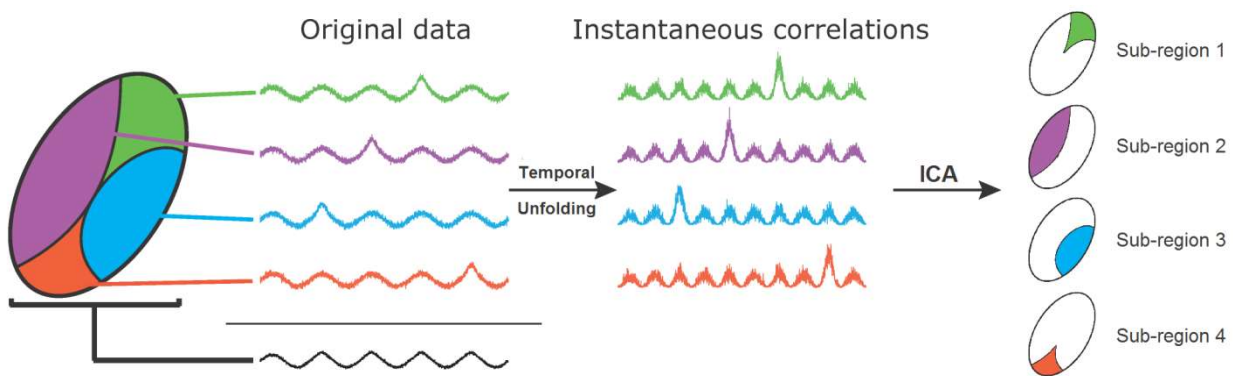
Figure 7. Illustration of the instantaneous correlation parcellation strategy. The oval represents a ROI consisting of four subregions. The black time course represents the average timeseries of the entire ROI, whereas the four colored timeseries represent exemplar timeseries for a voxel within each subregion. Multiplying each of these voxel specific timeseries with the average time course of the entire ROI (temporal unfolding), results in instantaneous correlations in which the subtle differences between the timeseries of each voxel are enhanced (increase in SNR of about 3 dB in this example). Subsequently, ICA is applied to the unfolded timeseries to segregate the region of interest into subregions by grouping voxels with similar instantaneous correlations. Adapted from Oldehinkel et al. 2016.

Hypothesis & Objectives

Hypothesis

The dopamine transporter SPECT is a useful and widespread tool to assess the neurodegenerative state of the nigrostriatal pathway. Therefore, this image is helpful to evaluate the disease state, including motor and non-motor symptoms, in Parkinson's disease (PD) and other parkinsonisms. However, its use is limited to determining the presence of nigral degeneration in clinical settings and assessing large striatal ROIs in clinical research. We hypothesized that more elaborated computational approaches to evaluate this image will help to: i) improve its reliability to further understanding disease hallmarks; and ii) develop extended clinical applications including the differential diagnosis between PD and other secondary and atypical parkinsonisms.

More specifically we hypothesized that:

- PD patients with a non-tremorigenous motor profile, namely postural instabiliy gait disorders subtype, will have lowers levels striatal dopamine and uric acid.

- Distinct genetic factors affect distinct aspects of cognitive impairment in PD. *APOE2, APOE4, MAPT* H1, *SNCA* rs356219, *COMT* Val158Met and variants in *GBA* may have a different role in the dual syndromes: frontostriatal dopamine-mediated and posterior-cortical leading to dementia.

- Vascular parkinsonism and PD can be accurately differentiated with objective and automated algorithms using the DAT SPECT.

- A particular brain region like the striatum can be accurately and parsimoniously represented with a linear combination of spatial basis funcions. A set of multiresolutional subparcellations of the striatum, using advanced termporal processing of fMRI experiments, can constitute a potential basis set of functions.

- The intensity histogram of the DAT SPECT images has the form of a mixture model of Gamma distributions. The intensity of images acquired with different Gamma cameras can be harmonized by using the parameters of the resulting Gamma distributions.

Objectives

In this thesis multiple disciplines of clinical neuroscience have been engaged, such as clinical neurology, genetics and computational methods, to achieve a set of objectives. Two global objectives were pursued: i) to improve our understanding of the motor and non-motor phenotype in PD aided by an *in-vivo* assessment of the patient with striatal DAT imaging; and ii) to improve the processing and assessment of DAT images with the use advanced computational approaches ir order to explore new potential clinical applications in parkinsonisms.

The specific objectives are:

- To investigate whether PD motor subtypes differ in their levels of uric acid, and if these differences correlate with the degree of striatal DAT
- To investigate the role of *APOE*, *MAPT*, *COMT*, *SNCA* and *GBA* genes n both striatal denervation and the development of dementia in PD
- To investigate and develop new methods of machine learning and pattern recognition for functional neuroimaging using advanced techniques, ir order to find new clinical applications for DAT SPECT
- To develop algorithms using DAT SPECT images to automatically differentiate between PD from other parkinsonian disorders, such as the vascular parkinsonism and the progressive supranuclear palsy
- To develop a voxel-based intensity normalization method for DAT SPECT images to allow harmonizing the images produced by different Gamma cameras

Summary of the results

Summary of the results

In this section, the results obtained in the works presented in this thesis are briefly summarized.

In the article "**Lower levels of uric acid and striatal dopamine in non-tremor dominant Parkinson's disease subtype**" we investigated the differences in uric acid and striatal DAT in PD motor subtypes: tremor-dominant (TD), intermediate (I), or postural instability and gait disorder (PIGD).

We found that:

- Uric acid levels were significantly lower for PIGD than for TD (3.7 vs 5.3 mg/dL; P<0.001) and I (3.7 vs 4.5 mg/dL; P=0.05) subtypes.
- Striatal DAT levels were significantly lower for PIGD than for TD (3.7 vs 5.3; P<0.001) and I (3.7 vs 4.5; P=0.05) subtypes.
- Uric Acid and striatal DAT levels were significantly correlated in posterior putamen (R^2=0.18; P=0.002), anterior putamen (R^2=0.18; P=0.001) and posterior caudate (R^2=0.23; P<0.001).
- All TD patients (100%) had a tremor onset, while this percentage reduced to 45% for I and to 25% for PIGD (P<0.001). We speculate that UA might be involved in the maintenance of the less damaging TD phenotype and thus also in the conversion from TD to PIGD.

In the article "**Genetic factors influencing frontostriatal dysfunction and the development of dementia in Parkinson's disease**" we investigated the contribution to the dual syndromes of cognitive impairment in PD (frontostriatal dopamine-mediated and posterior cortical leading to dementia) of the main genetic risk factors decribed in the literature: *GBA*, *MAPT*, *APOE*, *SNCA* and *COMT*.

We found that:

- *APOE2* allele (P_{put}=0.002; P_{cau}=0.01), the minor allele 'G' in *SNCA* polymorphism (P_{put}=0.02; P_{cau}=0.006) and *GBA* deleterious variants in (P_{put}=0.01; P_{cau}=0.001) had a detrimental effect on striatal DAT.
- Met/Met carriers in *COMT* polymorphism had increased caudate DAT (P_{cau}=0.03).
- Progression to dementia was influenced by *APOE4* allele (HR=1.90; *P*=0.03) and *GBA* deleterious variants (HR=2.44; *P*=0.01).
- The controversial *MAPT* had no role in either striatal DAT or dementia.

In the article "**Machine learning models for the differential diagnosis of vascular parkinsonism and Parkinson's disease using [123I]FP-CIT SPECT**" we developed diagnostic models with machine learning algorithms to differentate between vascular parkinsonism (VP) and Parkinson's disease (PD). We assessed the DAT SPECT images with two methods: ROI-based and whole-brain voxel-based.

We found that:

- In regional striatal ROI analyses (putamen and caudate), there were significant differences between VP and PD in the most-affected putamen and the ipsilateral caudate. Age, disease duration and severity were also different.
- Logistic regression using the ROI variables and the significant covariates gave a diagnostic accuracy of 90.3%.
- The voxel-based analysis localized significant reductions in $[^{123}I]$FP-CIT uptake in PD with respect to VP in two specular clusters of 1113 and 1320 voxels comprising areas corresponding to left and right striatum, respectively.
- A Support Vector Machine model using the voxel data gave a diagnostic accuracy of 90.4%.

In the article "**A Bayesian spatial model for neuroimaging using multiscale functional parcellations**" we developed a new anaylsis framework to perform inferences with functional neuroimaging data. We introduced a new family of basis functions (ICP functions), extracted from functional MRI experiments, to build parsimonious models. To test our new framework, we applied the model to fit quantitative images of DAT SPECT using the new basis set as compared with other potential basis sets including: generic isotropic bisquare functions, anatomical parcellations from Harvard-Oxford (HO) and Oxford-Imanova (OI) atlases, and independent components from ICA analyses as an alternative strategy to process functional MRI. We also showed the utility of our method to develop clinical application by constructing classifiers for parkinsonian syndromes with DAT SPECT images.

We found that:

- The new model provided an accurate (90% of explained variance) low-dimensional represensentation of the striatum with a reduced number of basis functions (e.g. 50 ICP parcellations) and the corresponding weights. This gave a substantial reduction of the number of parameters as compared with the number of striatal voxels (V = 4,622).
- The representation of the striatum was more accurate with the newly proposed family of basis functions (ICP parcellations) than with other basis sets. The explained variance was superior with ICP than with i) bisquare functions: indicating that basis functions derived from brain function are superior than generic; ii) anatomical parcellations, even at the same model order, indicating that functional imaging modalities can be better explained with brain function than with brain structure; and iii) functional independent components: indicating the importance of the multi-resolutional property recommended in spatial theory.

- Our framework allows to easily develop clinical applications. The weights associated with the basis functions, which implicitly encode spatial information, can be used in second-level analyses for classification or regression. We built classifiers to distinguish PD from normal controls with outstanding performance (AUC = 99%). We also built more challenging classifiers, aiming at distinguishim PD from PSP and its subtypes. We obtained relatively good performance to differentiate PD vs all PSP with different basis sets (AUC around 80%). We observed that the model using ICP functions was the best discriminanting the PSP subtypes (RS vs PAGF, AUC = 88%)

In the work "**Probabilistic intensity normalization of dopamine SPECT images via Variational mixture of Gamma distributions**" we aimed at developing a voxel-based intensity normalization method for DAT SPECT images. The method equalizes intensity and enhances performance of analyses when working with images acquired with different Gamma cameras.

We found that:
- The intensity histogram of a DAT SPECT image has the form of a mixture model of Gamma distributions, two modeling the background and another modeling the specific region.
- The model parameters of the distributions can be used to re-cast the intensity at the voxel level into a new – and universal – normalized feature space between 0 and 1.
- The proposed methodology alleviated intensity differences between scans acquired with different Gamma cameras
- The proposed reparameterization drastically improved the accuracy of PD diagnosis when images from different cameras were pooled. From the initial 83% to 93% range of performance using the current ROI-based normalization method, this increased after our proposed normalization to 89%-98% with ROI-based classifiers, and further to 95%-100% with voxel-based classifiers.

Publications

Lower levels of uric acid and striatal dopamine in non-tremor dominant Parkinson's disease subtype

Lower levels of uric acid and striatal dopamine in non-tremor dominant Parkinson's disease subtype

Ismael Huertas, MSc[1]; Silvia Jesús, MD, PhD[1]; José Antonio Lojo, MD[2]; Francisco Javier García-Gómez, MD[2]; María Teresa Cáceres-Redondo, MD[1]; Juan Manuel Oropesa-Ruiz, MD[1]; Fátima Carrillo, MD, PhD[1]; Laura Vargas-Gonzalez, RN[1]; Juan Francisco Martín Rodríguez, PhD[1]; Pilar Gómez-Garre, PhD [1,3]; David García-Solís, MD[2,3]; Pablo Mir, MD, PhD[1,3*].

1. Unidad de Trastornos del Movimiento, Servicio de Neurología y Neurofisiología Clínica, Instituto de Biomedicina de Sevilla (IBiS), Hospital Universitario Virgen del Rocío/CSIC/Universidad de Sevilla, Seville, Spain.
2. Servicio de Medicina Nuclear. UDIM. Hospital Universitario Virgen del Rocío, Seville, Spain.
3. Centro de Investigación Biomédica en Red sobre Enfermedades Neurodegenerativas (CIBERNED), Spain.

Author for correspondence: Dr. Pablo Mir. Unidad de Trastornos del Movimiento. Servicio de Neurología y Neurofisiología Clínica. Hospital Universitario Virgen del Rocío. Avda. Manuel Siurot s/n. 41013 Sevilla, Spain. Tel.: +34 955923040. Fax: +34 955923101. e-mail: pmir@us.es

Word count: 2609

Keywords: Parkinson's disease; Uric Acid; [123I]FP-CIT SPECT; Motor subtypes

Abstract

Parkinson's disease (PD) patients who present with tremor and maintain a predominance of tremor have a better prognosis. Similarly, PD patients with high levels of uric acid (UA), a natural neuroprotectant, have also a better disease course. Our aim was to investigate whether PD motor subtypes differ in their levels of UA, and if these differences correlate with the degree of dopamine transporter (DAT) availability. We included 75 PD patients from whom we collected information about their motor symptoms, DAT imaging and UA concentration levels. Based on the predominance of their motor symptoms, patients were classified into postural instability and gait disorder (PIGD, n=36), intermediate (I, n=22), and tremor-dominant (TD, n=17) subtypes. The levels of UA and striatal DAT were compared across subtypes and the correlation between these two measures was also explored. We found that PIGD patients had lower levels of UA (3.7 vs 4.5 vs 5.3 mg/dL; $P<0.001$) and striatal DAT than patients with an intermediate or TD phenotype. Furthermore, UA levels significantly correlated with the levels of striatal DAT. We also observed that some PIGD (25%) and I (45%) patients had a predominance of tremor at disease onset. We speculate that UA might be involved in the maintenance of the less damaging TD phenotype and thus also in the conversion from TD to PIGD. Low levels of this natural antioxidant could lead to a major neuronal damage and therefore influence the conversion to a more severe motor phenotype.

Introduction

Parkinson's disease (PD) patients can be categorized, based on the predominant motor symptoms, into tremor-dominant (TD) and non-tremor dominant subtypes (Foltynie et al., 2002). The former is characterized by a predominance of tremor and the latter by a predominance of rigidity, akinesia, and/or postural instability and gait disorder (PIGD) symptoms. This distinction differs between symptom predominance at presentation of the disease and symptom predominance at later stages, since some patients presenting with tremor at onset become predominantly rigid-akinetic or PIGD in more advanced stages (Hershey et al., 1991). Previous studies have demonstrated that PD patients who continue to have tremor dominance after several years progress more slowly than those with predominance of non-tremor symptoms (Jankovic et al., 1990, Rajput et al., 2009), including a lower likelihood to develop cognitive impairment and dementia (Lewis et al., 2005, Reijnders et al., 2009). At autopsy, TD patients have less pathological burden (Paulus and Jellinger, 1991, Selikhova et al., 2009), and accordingly, neuroimaging studies have found a higher degree of dopaminergic denervation (Spiegel et al., 2007, Rossi et al., 2010, Schillaci et al., 2011, Eggers et al., 2012, Kaasinen et al., 2014) and grey matter atrophy in the non-tremor subtype (Rosenberg-Katz et al., 2013). It is not yet well-known whether the pathophysiological mechanisms underlying these PD subtypes are different (Zaidel et al., 2009, Helmich et al., 2012).

A major challenge is to unravel why PD patients presenting and maintaining a TD phenotype have a better prognosis (i.e. slower deterioration), or conversely, why PD patients with a non-tremor onset, or PD patients with a tremor onset but converting to rigid-akinetic and/or PIGD, progress worse (i.e. faster deterioration). It is likely that multiple factors play a role in PD phenotype and progression, including genetic susceptibility loci and environmental factors, but the identification of potential biomarkers is essential to improve treatment. A possible explanation for these differences could be that, although the biological mechanisms triggering sporadic PD for both subtypes were the same, these patients might differ in their levels of endogenous neuroprotective agents. In this regard, uric acid (UA) is an important natural antioxidant in the human body and it has been demonstrated that it reduces damage to neurons caused by oxidative stress. Indeed, low levels of serum UA have been associated with an increased risk to develop neurodegenerative diseases, including PD (Schlesinger and Schlesinger, 2008, Chen et al., 2012). Furthermore, longitudinal studies have determined that PD patients with lower levels of serum UA deteriorate more quickly (Schwarzschild et al., 2008, Ascherio et al., 2009).

In this study we sought to investigate whether the tremor and non-tremor PD subtypes differ in their levels of serum UA and degree of dopaminergic degeneration, and if these two measurements correlate. To this end, we collected motor information, UA levels and dopamine transporter (DAT) imaging by [^{123}I]FP-CIT SPECT from 214 PD patients. Using retrospective data from the disease motor onset, we investigated in late stage patients whether patients who consistently maintained throughout the time a TD phenotype had higher values of UA as compared with those who developed PIGD symptoms. We hypothesized that the major neuronal damage seen in non-tremor PD patients could be related to a lower degree of neuroprotection, and UA might be one of the factors implicated in these mechanisms.

Materials and Methods

Subjects

We collected information from 75 PD patients (60% males, age of onset 46 ± 10 years [19-64], disease duration after symptom onset: 12 ± 6 years [5-23]) whom visited the Movement Disorders Unit from 2004 to 2014 at Hospital Virgen del Rocío (Seville, Spain). All patients had confirmed PD diagnosis based on the UK Parkinson's Disease Society Brain Bank clinical diagnostic criteria. For all these patients, we collected information about motor status and symptoms, [123I]FP-CIT SPECT, and serum UA concentration levels. The study was approved by the Hospital Virgen del Rocío ethics committee and all patients signed informed consent to participating in the study.

Uric Acid measurement

Blood samples of the patients were processed after extraction at the Central Laboratory of our Hospital. Serum urate concentration was determined by means of enzymatic assay following the standards in routine clinical practice. We did not include patients with conditions that could affect the serum UA concentration such as lymphoproliferative diseases, cancer, chemotherapy, haemolytic and pernicious anaemia, alcoholism, hypoxanthine phosphorylated guanidine deficits, gout, diabetic and alcoholic ketoacidosis, treatments that could affect the serum UA concentration [acetylsalicylic acid, diuretics, nicotinic acid, ethambutol, allopurinol, cyclosporine and pyrazinamide], lead poisoning, renal disease and hypo- or hyperthyroidism.

Classification into motor subtypes

Patients were classified based on established methods into TD, PIGD, or intermediate (I) using items from the Unified Parkinson's Disease Rating Scale (UPDRS), off-medication (Jankovic et al., 1990). We considered that the motor phenotype at this UPDRS evaluation after a mean follow-up of 12 years was stable and definite. Patients' tremor score was determined by adding items 16 and 20-21, and dividing by 8, and balance and gait score by adding items 13-15 and 29-30, and dividing by 5. Patients were defined as TD if the ratio of the tremor score divided by the balance and gait score was ≥ 1.50, PIGD if the ratio was ≤ 1, and as I if the ratio was between 1-1.50. Disease severity by Hoehn and Yahr (H&Y) stage and the main symptom at onset (Tremor Onset (TO): any presence of tremor (from slight to severe) vs, Non-tremor Onset) were also recorded.

SPECT imaging

The acquisition procedure and SPECT reconstruction were carried out following standard protocols and can be found in a previous report (Huertas-Fernandez et al., 2015). SPECT images were processed with SPM8 using a homemade [123I]FP-CIT template (http://www.nitrc.org/projects/spmtemplates), and following the standard processing pipeline in SPM. We extracted the average [123I]FP-CIT binding at posterior and anterior putamen, and posterior caudate (head of caudate) using a custom-made parcellation of the striatum (https://www.nitrc.org/projects/striatalvoimap) following established methodology (Oh et al.,

2012). For each patient and striatal subregion, we calculated the $[^{123}I]$FP-CIT specific binding ratio (SBR) with respect to a non-specific volume in the occipital cortex by the formula: (striatal regional binding - occipital binding)/occipital binding.

Given the high influence of age and scanner in the value of SBR (Varrone et al., 2013), we have worked with the age-normalized SBR instead (nSBR) (although raw SBR are also provided in supporting information). This measure is defined as the ratio between the patient SBR and the average age-specific healthy SBR, the latter calculated from linearly regressing age and SBR of normal controls. Thus, this measure represents the age and scanner-specific reduction of SBR due to the disease and makes these imaging variables more comparable with other studies using other machines (Pirker, 2003). For this, we used in-house images of 184 scans without evidence of dopaminergic deficit from the same scanner (age range 18–90 years; 56% males). In line with previous findings, we observed a 5.1% SBR decline per decade in these normal controls (Varrone et al., 2013). Lastly, since PD is asymmetrical by nature and laterality can affect the statistics at the group level, the comparisons were made for contralateral and ipsilateral to the most affected side instead of right and left.

Statistical analysis

We compared the three motor subtypes (TD, I and PIGD) using Chi-square test for nominal variables, ANOVA for quantitative variables, and the Kruskal Wallis test for the H&Y stage. Post-hoc analyses were performed to compare significant associations in a pairwise manner. Additionally, since UA levels are higher in men than in women by nature, we examined UA levels separated by sex as well. The correlation between UA and SPECT variables was evaluated with Pearson's coefficient and the value of R^2 (explained variance) is reported. Linear regression analyses were also performed to verify that the associations of UA and striatal nSBR with the motor subtype were not confounded by other variables such as age, sex and disease severity (UPDRSIII and H&Y). The significance threshold was set to $P<0.05$. Statistical analyses were performed with IBM SPSS Statistics 22.0.

Results

Descriptive values and statistics are shown in Table 1. Of the 75 PD patients, 36 were classified as PIGD, 22 as I and 17 as TD. ANOVA indicated that UA levels were different across subtypes (P<0.001). Post-hoc analyses revealed that UA was significantly lower for PIGD than for TD (3.7 vs 5.3; P<0.001) and I (3.7 vs 4.5; P=0.05) subtypes. When segregated by sex, UA levels were slightly higher in males as expected, but importantly, the differences across motor subtypes remained consistent (P=0.041). Post-hoc comparisons were still significant between PIGD and TD subtypes although the differences between PIGD and I subtypes vanished probably due to a loss in statistical power. ANOVA analyses also showed differences in striatal nSBR across motor subtypes (P<0.01, see Table), and in particular that PIGD had lower nSBR values than TD and I phenotypes (P<0.05). This was consistent for both ipsilateral and contralateral hemispheres and for both normalized SBR and raw SBR (raw SBR values are available in Table S1 in supporting information). Furthermore, UA levels were significantly correlated with striatal nSBR in posterior putamen (R^2=0.17; P=0.002), anterior putamen (R^2=0.18; P=0.001) and posterior caudate (R^2=0.23; P<0.001) (Fig 1).
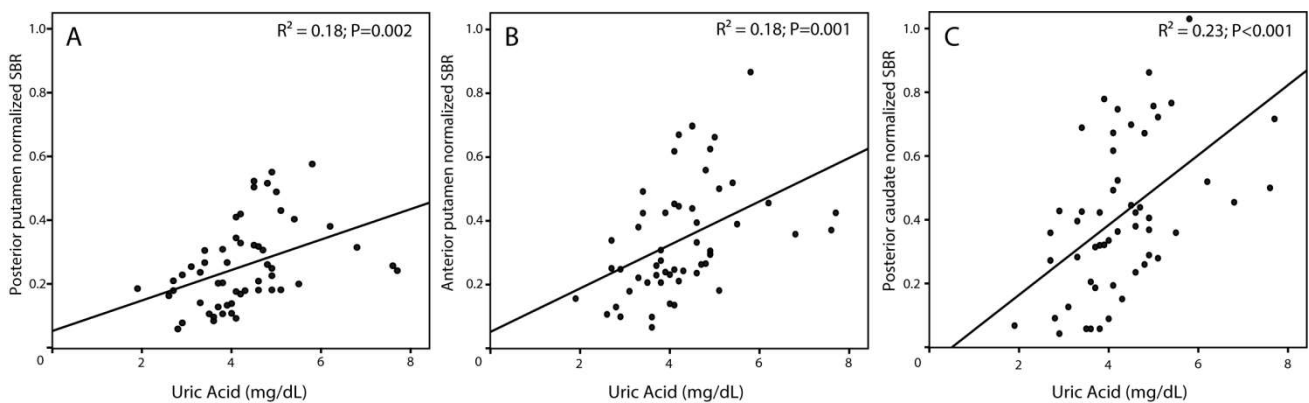
Fig 1. Correlation of uric acid and contralateral normalized specific binding ratio (nSBR) for posterior putamen (A), anterior putamen (B), and posterior caudate (C).

Regarding motor scales, PIGD patients were more severely affected than TD and I patients (H&Y = 4 > 3, P<0.001), and had UPDRS total score was higher than TD patients (90 vs 74, P<0.05). Multivariate regression analyses confirmed that the positive univariate associations between motor subtypes and UA (β = 0.43, P=0.006) and (putamen) nSBR (β = 0.38, P=0.01) remained significant after correcting for the potential confounds and the differences in severity. Finally, when retrospectively examined the motor symptom onset of these patients, we observed that all TD patients (100%) had a tremor onset, but there was also a non-negligible percentage of patients with tremor onset who converted to I (45%) and to PIGD (25%) over the disease course. In this article, we speculate that this conversion may be partially driven by UA.

Table 1. Demographic values, motor information, uric acid levels and the regional age-normalized [^{123}I]FP-CIT SBR.

	PIGD (n=36)	I (n=22)	TD (n=17)	p-value
Sex (m/f)	17 / 19	15 / 7	13 / 4	N.S.
Age of onset (y)	46 ± 9	41 ± 9	45 ± 12	N.S.
Disease duration (y)	13 ± 6	13 ± 6	11 ± 7	N.S.
TO (%)	25%	45%	100%***	**<0.001**
UPDRS-III	49 ± 12	49 ± 12	46 ± 11	N.S.
UPDRS Total	90 ± 22	86 ± 22	74 ± 14*	**0.036**
Hoehn & Yahr	4 [3, 5]	3 [2.5, 4]***	3 [2.5, 3]***	**<0.001**
Uric Acid (mg/dL)	3.7 ± 0.9	4.5 ± 1.1*	5.3 ± 1.3***	**<0.001**
Male	4.0 ± 1.0	4.7 ± 1.0	5.3 ± 1.3*	**0.041**
Female	3.4 ± 0.8	4.0 ± 1.0	5.2 ± 1.8*	**0.041**
Posterior putamen nSBR				
contralateral	0.18 ± 0.13	0.29 ± 0.14*	0.30 ± 0.16*	**0.004**
ipsilateral	0.24 ± 0.13	0.34 ± 0.15*	0.38 ± 0.18**	**0.004**
Anterior putamen nSBR				
contralateral	0.24 ± 0.16	0.38 ± 0.18*	0.40 ± 0.20*	**0.002**
ipsilateral	0.31 ± 0.16	0.45 ± 0.19*	0.47 ± 0.20**	**0.002**
Posterior caudate nSBR				
contralateral	0.28 ± 0.25	0.49 ± 0.28*	0.46 ± 0.29*	**0.008**
ipsilateral	0.40 ± 0.26	0.63 ± 0.29*	0.61 ± 0.29**	**0.002**

* p<0.05, ** p<0.01, *** p<0.001 for post-hoc analyses with respect to PIGD.

PIGD: postural instability and gait disorder subtype; TD: tremor-dominant subtype, I: intermediate subtype; TO: Tremor Onset; N.S.: not significant.

Discussion

In this study we found that PD patients with a PIGD motor phenotype have lower levels of serum UA and striatal DAT availability than PD patients with a predominance of tremor, and that the levels of UA are correlated with the degree of striatal dopamine depletion. These associations were significant in both univariate and multivariate analyses where potential confounds were also accounted for. Furthermore, using retrospective data of late stage patients, we also found that patients who maintained a TD phenotype throughout the disease course, or to a lesser extent progressed to an intermediate phenotype, had higher levels of UA and striatal DAT than PD patients who converted to the PIGD phenotype.

Our results are in line with a similar study that found significant lower UA levels and higher disease severity in PD patients with a non-tremor subtype (Lolekha et al., 2015). These authors also found consistent differences across motor subtypes for both genders, which is important given the inherent difference in UA values between men and women. However it is worth commenting that the levels of UA concentration in the study of Lolekha and colleagues were in overall higher than in our study. For example, on average, they observed 5.9 mg/dL in their TD patients as compared with 5.3 mg/dL in our cohort, and these differences were even more accentuated when segregated by sex, where they report an average value of 6.4 mg/dL for TD males. We discard the UA assessment method as the main cause of this discrepancy since we also followed standard methodology to measure UA concentration, so we speculate that these differences are more likely due to intrinsic differences between the two populations (Thailand vs Spain) such as diet and ethnic origin among others. Also in line, our group in a previous study, and another cross-sectional study found lower levels of UA in advanced Hoehn and Yahr stages (Sun et al., 2012, Jesus et al., 2013). The longitudinal PRECEPT and DATATOP studies also found that PD patients with lower levels of UA at baseline suffered from faster rates of clinical progression, including greater declines in the UPDRS total score and striatal DAT availability (Schwarzschild et al., 2008, Ascherio et al., 2009).

Imaging of the striatal DAT is also a marker of disease severity and PD subtypes show a different degree of dopaminergic depletion in both hemispheres. In particular, higher motor severity, postural instability and falling have been associated with lower striatal DAT binding (Ravina et al., 2012). Previous studies also found higher [123I]FP-CIT uptake in TD in both putamen and caudate than in rigid-akinetic (Spiegel et al., 2007, Schillaci et al., 2011). A longitudinal study found higher declines in rigid-akinetic in striatal DAT at follow-up, although they found no differences at baseline (Eggers et al., 2012). Rossi et al. only found differences in putamen, probably because they included patients at a very early stage (<1 year of disease duration) and the caudate region was probably not sufficiently affected for differences between groups to be noted.(Rossi et al., 2010) Similarly, our results are partially consistent with a recent study that found higher caudate [123I]FP-CIT uptake but no differences in putaminal binding (Kaasinen et al., 2014). However, since the putamen is the part of the striatum involved in the motor loop, it is surprising to find that patients with a different motor phenotype do not differ in their levels of dopamine depletion in this region. Some obvious differences in methodology could have led to this discordance.

The correlations between UA levels and DAT binding are consistent with a recent study performed in 52 newly diagnosed, drug-naïve PD patients, although its correlation coefficients ($R^2_{putamen}$= 0.136; $R^2_{caudate}$= 0.349) were not exactly the same (Moccia et al., 2015). These correlations are also in line with findings from the PRECEPT study, in which it was found that higher levels of urate were associated with a greater likelihood of a DAT scan without evidence of a dopaminergic deficit (Schwarzschild et al., 2011). Of relevance, all of these results are in line with the hypothesis that UA acts as a protector against dopaminergic degeneration and, in keeping with this notion, a recent animal study found attenuated toxic effects on nigral dopaminergic cell counts and striatal dopamine content in UOx (the gene encoding urate oxidase) knockout mice (Chen et al., 2013).

We observed that 100% of TD had a tremor onset, but there was also a non-negligible proportion of patients that converted from a tremor-dominant onset to an intermediate phenotype (45% of I) or even to PIGD (25% of PIGD). This suggests that, in accordance with the literature (Hershey et al., 1991), PD patients with a tremor onset may evolve as the disease progresses to TD, I or, with a lower likelihood, to PIGD. Although a longitudinal study is necessary to corroborate this hypothesis, we speculate that those patients with a tremor onset that will maintain a TD phenotype may be those with higher levels of UA. Conversely, those with lower levels of UA could convert to an intermediate or PIGD subtype (Fig 2). Predicting motor disease progression is highly complex and may depend on multiple interacting factors (including genetic factors), but our results suggest that the motor phenotype may also be partially driven by UA levels. In this case, high levels of UA could help to maintain a less damaging TD form of PD.
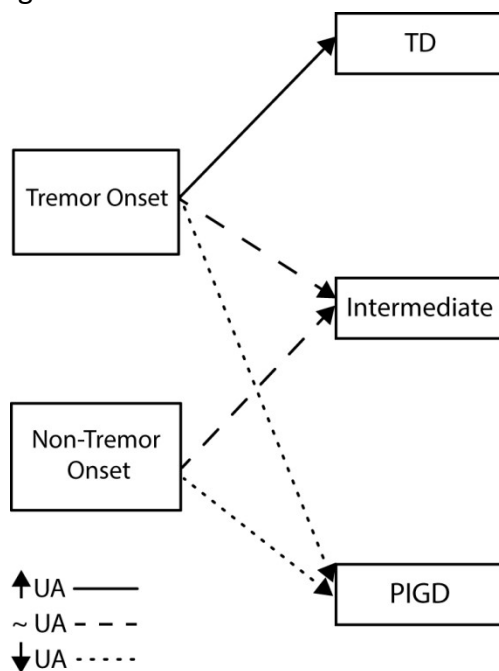
Fig 2. Diagram of conversion to motor phenotypes according to the levels of uric acid.

Lastly, we acknowledge the limitations in our design and sample size to draw solid conclusions about our results. To corroborate our hypothesis, it would be very interesting to study in longitudinal cohorts such as PRECEPT the progression/conversion to motor phenotypes based on

the levels of UA at baseline and at follow-up. Unfortunately, direct comparison is not possible since these researchers compared and reported an UPDRS total score obtained by adding the motor activity, mentation, and activity of daily living subscales and did not perform motor subtype classification.

In summary, in this study we provide further evidence about the differences in UA and striatal DAT between PD motor subtypes. We hypothesize and would like to test in the future whether PD patients who present with a tremor onset and maintain predominance of tremor, or, to a lesser extent, an intermediate phenotype, have higher levels of UA than those who develop PIGD symptoms. In this scenario, UA might be involved in maintaining the less damaging tremor-dominant form of PD. Low levels of this natural antioxidant may lead to a lesser degree of neuroprotection and could therefore influence motor phenotype and the clinical course.

Funding disclosure

References

Foltynie T, Brayne C, Barker RA (2002) The heterogeneity of idiopathic Parkinson's disease. J Neurol 249: 138-145.

Hershey LA, Feldman BJ, Kim KY, Commichau C, Lichter DG (1991) Tremor at onset. Predictor of cognitive and motor outcome in Parkinson's disease? Arch Neurol 48: 1049-1051.

Jankovic J, McDermott M, Carter J, Gauthier S, Goetz C, et al. (1990) Variable expression of Parkinson's disease: a base-line analysis of the DATATOP cohort. The Parkinson Study Group. Neurology 40: 1529-1534.

Rajput AH, Voll A, Rajput ML, Robinson CA, Rajput A (2009) Course in Parkinson disease subtypes: A 39-year clinicopathologic study. Neurology 73: 206-212.

Lewis SJ, Foltynie T, Blackwell AD, Robbins TW, Owen AM, et al. (2005) Heterogeneity of Parkinson's disease in the early clinical stages using a data driven approach. J Neurol Neurosurg Psychiatry 76: 343-348.

Reijnders JS, Ehrt U, Lousberg R, Aarsland D, Leentjens AF (2009) The association between motor subtypes and psychopathology in Parkinson's disease. Parkinsonism Relat Disord 15: 379-382.

Paulus W, Jellinger K (1991) The neuropathologic basis of different clinical subgroups of Parkinson's disease. J Neuropathol Exp Neurol 50: 743-755.

Selikhova M, Williams DR, Kempster PA, Holton JL, Revesz T, et al. (2009) A clinico-pathological study of subtypes in Parkinson's disease. Brain 132: 2947-2957.

Eggers C, Pedrosa DJ, Kahraman D, Maier F, Lewis CJ, et al. (2012) Parkinson subtypes progress differently in clinical course and imaging pattern. PLoS One 7: e46813.

Kaasinen V, Kinos M, Joutsa J, Seppanen M, Noponen T (2014) Differences in striatal dopamine transporter density between tremor dominant and non-tremor Parkinson's disease. Eur J Nucl Med Mol Imaging 41: 1931-1937.

Rossi C, Frosini D, Volterrani D, De Feo P, Unti E, et al. (2010) Differences in nigro-striatal impairment in clinical variants of early Parkinson's disease: evidence from a FP-CIT SPECT study. Eur J Neurol 17: 626-630.

Schillaci O, Chiaravalloti A, Pierantozzi M, Di Pietro B, Koch G, et al. (2011) Different patterns of nigrostriatal degeneration in tremor type versus the akinetic-rigid and mixed types of Parkinson's disease at the early stages: molecular imaging with 123I-FP-CIT SPECT. Int J Mol Med 28: 881-886.

Spiegel J, Hellwig D, Samnick S, Jost W, Mollers MO, et al. (2007) Striatal FP-CIT uptake differs in the subtypes of early Parkinson's disease. J Neural Transm (Vienna) 114: 331-335.

Rosenberg-Katz K, Herman T, Jacob Y, Giladi N, Hendler T, et al. (2013) Gray matter atrophy distinguishes between Parkinson disease motor subtypes. Neurology 80: 1476-1484.

Helmich RC, Hallett M, Deuschl G, Toni I, Bloem BR (2012) Cerebral causes and consequences of parkinsonian resting tremor: a tale of two circuits? Brain 135: 3206-3226.

Zaidel A, Arkadir D, Israel Z, Bergman H (2009) Akineto-rigid vs. tremor syndromes in Parkinsonism. Curr Opin Neurol 22: 387-393.

Chen X, Wu G, Schwarzschild MA (2012) Urate in Parkinson's disease: more than a biomarker? Curr Neurol Neurosci Rep 12: 367-375.

Schlesinger I, Schlesinger N (2008) Uric acid in Parkinson's disease. Mov Disord 23: 1653-1657.

Ascherio A, LeWitt PA, Xu K, Eberly S, Watts A, et al. (2009) Urate as a predictor of the rate of clinical decline in Parkinson disease. Arch Neurol 66: 1460-1468.

Schwarzschild MA, Schwid SR, Marek K, Watts A, Lang AE, et al. (2008) Serum urate as a predictor

of clinical and radiographic progression in Parkinson disease. Arch Neurol 65: 716-723.

Huertas-Fernandez I, Garcia-Gomez FJ, Garcia-Solis D, Benitez-Rivero S, Marin-Oyaga VA, et al. (2015) Machine learning models for the differential diagnosis of vascular parkinsonism and Parkinson's disease using [(123)I]FP-CIT SPECT. Eur J Nucl Med Mol Imaging 42: 112-119.

Oh M, Kim JS, Kim JY, Shin KH, Park SH, et al. (2012) Subregional patterns of preferential striatal dopamine transporter loss differ in Parkinson disease, progressive supranuclear palsy, and multiple-system atrophy. J Nucl Med 53: 399-406.

Varrone A, Dickson JC, Tossici-Bolt L, Sera T, Asenbaum S, et al. (2013) European multicentre database of healthy controls for [123I]FP-CIT SPECT (ENC-DAT): age-related effects, gender differences and evaluation of different methods of analysis. Eur J Nucl Med Mol Imaging 40: 213-227.

Pirker W (2003) Correlation of dopamine transporter imaging with parkinsonian motor handicap: how close is it? Mov Disord 18 Suppl 7: S43-51.

Lolekha P, Wongwan P, Kulkantrakorn K (2015) Association between serum uric acid and motor subtypes of Parkinson's disease. J Clin Neurosci 22: 1264-1267.

Jesus S, Perez I, Caceres-Redondo MT, Carrillo F, Carballo M, et al. (2013) Low serum uric acid concentration in Parkinson's disease in southern Spain. Eur J Neurol 20: 208-210.

Sun CC, Luo FF, Wei L, Lei M, Li GF, et al. (2012) Association of serum uric acid levels with the progression of Parkinson's disease in Chinese patients. Chin Med J (Engl) 125: 583-587.

Ravina B, Marek K, Eberly S, Oakes D, Kurlan R, et al. (2012) Dopamine transporter imaging is associated with long-term outcomes in Parkinson's disease. Mov Disord 27: 1392-1397.

Moccia M, Pappata S, Erro R, Picillo M, Vitale C, et al. (2015) Uric acid relates to dopamine transporter availability in Parkinson's disease. Acta Neurol Scand 131: 127-131.

Schwarzschild MA, Marek K, Eberly S, Oakes D, Shoulson I, et al. (2011) Serum urate and probability of dopaminergic deficit in early "Parkinson's disease". Mov Disord 26: 1864-1868.

Chen X, Burdett TC, Desjardins CA, Logan R, Cipriani S, et al. (2013) Disrupted and transgenic urate oxidase alter urate and dopaminergic neurodegeneration. Proc Natl Acad Sci U S A 110: 300-305.

Genetic factors influencing frontostriatal dysfunction and the development of dementia in Parkinson's disease

Genetic factors influencing frontostriatal dysfunction and the development of dementia in Parkinson's disease

Ismael Huertas, MSc[1]; Silvia Jesús, MD, PhD[1]; Francisco Javier García-Gómez, MD[2]; José Antonio Lojo, MD[2]; Inmaculada Bernal-Bernal, MSc[1]; Marta Bonilla-Toribio, MSc[1]; Juan Francisco Martín-Rodriguez, PhD[1]; David García-Solís, MD[2,3]; Pilar Gómez-Garre, PhD [1,3]; Pablo Mir, MD, PhD.[1,3*]

1. Unidad de Trastornos del Movimiento, Servicio de Neurología y Neurofisiología Clínica, Instituto de Biomedicina de Sevilla (IBiS), Hospital Universitario Virgen del Rocío/CSIC/Universidad de Sevilla, Seville, Spain.
2. Servicio de Medicina Nuclear. UDIM. Hospital Universitario Virgen del Rocío, Seville, Spain.
3. Centro de Investigación Biomédica en Red sobre Enfermedades Neurodegenerativas (CIBERNED), Spain.

Author for correspondence: Dr. Pablo Mir. Unidad de Trastornos del Movimiento. Servicio de Neurología y Neurofisiología Clínica. Hospital Universitario Virgen del Rocío. Avda. Manuel Siurot s/n. 41013 Sevilla, Spain. Tel.: +34 955923040. Fax: +34 955923101. E-mail: pmir@us.es

Abstract

The *dual syndrome* hypothesis for cognitive impairment in Parkinson's disease (PD) establishes a dichotomy between a frontrostriatal dopamine-mediated syndrome, which leads to executive deficits, and a posterior cortical syndrome, which leads to dementia. Certain genes have been linked to these syndromes although the exact contribution is still controversial. The study's objective was to investigate the role of *APOE*, *MAPT*, *COMT*, *SNCA* and *GBA* genes in the dual syndromes. We genotyped *APOE* (rs429358 and rs7412), *MAPT* (rs9468), *COMT* (rs4680) and *SNCA* (rs356219) risk polymorphisms and sequenced *GBA* in a cohort of 298 PD patients. The degree of dopaminergic depletion was investigated with [^{123}I]FP-CIT SPECTs the presence of dementia was ascertained with a long-term review based on established criteria. The association between genetic and imaging parameters was studied with linear regression, and the relationship with dementia onset with Cox regression. We found that *APOE2* allele (P_{put}=0.002; P_{cau}=0.01), the minor allele 'G' in *SNCA* polymorphism (P_{put}=0.02; P_{cau}=0.006) and *GBA* deleterious variants in (P_{put}=0.01; P_{cau}=0.001) had a detrimental effect on striatal [^{123}I]FP-CIT uptake in PD. Conversely, Met/Met carriers in *COMT* polymorphism had increased caudate uptake (P_{cau}=0.03). The development of dementia was influenced by *APOE4* allele (HR=1.90; *P*=0.03) and *GBA* deleterious variants (HR=2.44; *P*=0.01). Finally, we observed no role of *MAPT* locus in any of the syndromes. As a conclusion, *APOE2, SNCA*, *COMT* and *GBA* influence frontrostriatal dysfunction whereas *APOE4* and *GBA* influence the development of dementia, suggesting a double-edged role of *GBA*. The dichotomy of the dual syndromes may be driven by a broad dichotomy in these genetic factors.

Introduction

Cognitive impairment is a common and disabling non-motor symptom of Parkinson's disease (PD). Cognitive deficits may be present in up to 24% of PD patients by the time of diagnosis, and this rate reaches over 80% in the long-term (Aarsland et al., 2011). Although dysexecutive syndrome has long been considered the main hallmark of cognitive decline in PD, deficits in visuospatial, memory and attention functions may be also present. The rate and pattern of these deficits vary greatly among PD patients, and different biological mechanisms appear to play a role (Robbins and Cools, 2014). In this regard, the *dual syndrome* hypothesis was recently proposed, suggesting two facets of cognitive decline in PD: (i) changes in frontostriatal dopaminergic transmission, leading to deficits in planning, working memory, response inhibition and attentional control; and (ii) posterior cortical Lewy body pathology and secondary cholinergic loss, affecting visuospatial, mnemonic and semantic functions and leading to dementia (Kehagia et al., 2013).

It is possible to assess the state of the frontostriatal circuitry by imaging the striatal dopamine transporter (DAT) with [^{123}I]FP-CIT SPECT. In this scan, dopamine depletion can first be observed in the putamen, which affects the motor loop, whilst dopamine depletion in the caudate usually occurs in later stages, affecting two well-defined frontostriatal loops: the cognitive and the limbic loops (de la Fuente-Fernandez, 2013). Therefore, the integrity of this latter pathway is essential to correct cognitive functioning, and a large number of studies have in fact found a correlation between cognitive performance (including executive and working memory tasks) and caudate dopamine levels in PD (Brooks and Piccini, 2006).

Several genetic *loci* have also been proposed as risk factors for cognitive decline in PD (Mollenhauer et al., 2014). Some of these genetic *loci* have been linked to the dopaminergic pathway, such as the Val158Met polymorphism in the catechol-O-methyltransferase gene (*COMT*). This gene encodes the COMT enzyme, which contributes to the degradation of cortical dopamine. Met carriers show low enzyme activity in comparison to Val carriers. This genotype therefore modulates dopamine levels in the frontostriatal network, and in turn, executive function performance (Nombela et al., 2014). Other genetic *loci* have been linked to both the development of dementia and performance in tasks mediated by other non-dopaminergic mechanisms. Specifically, the apolipoprotein E gene (*APOE*) ε4 allele has been associated with an increased risk of dementia (Williams-Gray et al., 2009) and deficits in memory and verbal fluency (Mata et al., 2014, Nombela et al., 2014). Furthermore, the microtubule-associated protein tau gene (*MAPT*) H1 haplotype has been linked with dementia (Seto-Salvia et al., 2011, Williams-Gray et al., 2013) and visuospatial deficits (Nombela et al., 2014), although recent results have been controversial (Mata et al., 2014). It is not yet known what role these two *loci* play in dopaminergic degeneration, and this needs to be addressed. Another genetic *locus* of interest is the rs356219 polymorphism, located in the 3'UTR of the α-synuclein gene (*SNCA*). Mutations and repetitions in *SNCA* lead to a familial form of PD with prominent cognitive impairment and dementia. The rs356219 polymorphism has been linked to PD pathogenesis (Pihlstrom and Toft, 2011), although its role in cognition is far from clear. Its relationship with dopaminergic imaging has besides not yet been studied. Lastly, the glucocerebrosidase gene (*GBA*) is the most common genetic factor that has yet

been identified for developing PD (Sidransky et al., 2009). PD patients with mutations in *GBA* have earlier disease onset, and are at a higher risk of developing visual hallucinations, cognitive impairment and dementia (Neumann et al., 2009). Recent studies suggest that *GBA*-carriers have a more severe phenotype, with quicker disease progression (Winder-Rhodes et al., 2013). As is the case with other genes, very little is known about the relationship between *GBA* and dopaminergic imaging.

Although other groups are thoroughly investigating the relationship between these genes and domain-specific neuropsychological tasks, using large cohorts of PD patients, not enough studies have yet been conducted to evaluate how these genetic loci contribute to dopaminergic degeneration through imaging. Furthermore, recent studies have produced contradictory results concerning the role that some *loci*, such as the H1 haplotype in *MAPT*, play in PD dementia. This study aims to investigate the role that these genes play in striatal dopaminergic denervation and PD dementia. To this end, we collected [^{123}I]FP-CIT SPECT images and long-term clinical data on the developement of dementia, and genotyped *APOE*, *MAPT*, *COMT* and *SNCA* risk polymorphisms, as well as *GBA* screening in a cohort of 298 PD patients from our centre.

Materials and Methods

Subjects

A total of 298 PD patients were included in this study (age at onset 55 ± 13 years, 60% males), recruited from the Movement Disorders Unit at Virgen del Rocío Hospital (Seville, Spain). The diagnosis of PD was made using the UK Parkinson's Disease Society Brain Bank clinical diagnostic criteria. All patients underwent [^{123}I]FP-CIT SPECT (mean disease duration 6 ± 6 years, median Hoehn and Yahr 2 [1.5, 2.5]) and were clinically monitored during the course of the disease with periodic visits to our clinic. At SPECT exam, 17% of the patients had no medication, 17% on levodopa, 18% on dopaminergic agonists and 48% on both. The median levodopa equivalent daily dose (LEDD) for those under treatment was of 596 [300, 1063] mg/day. The influence of the genetic factors on the dopamine-mediated syndrome was investigated through the association between the genotypes and striatal DAT, whereas the influence on the posterior syndrome was investigated through the association between the genotypes and the onset of dementia. We identified patients who met diagnostic criteria for possible or probable dementia (Emre et al., 2007) in a long-term review of the medical records (mean disease duration at time of review: 11 years). The diagnosis of dementia was ascertained by a variety of screening tools including a medical interview to the patient and caregiver, or scores in standard scales such as Mini Mental State Examination (MMSE ≤ 24), and Parkinson's disease Dementia Short Screen (PDD-SS ≤ 11) (Pagonabarraga et al., 2010).

The disease duration at the visit when the patient met the criteria was used to perform survival analyses of the progression to dementia. The core features of these criteria include the presence of deficits (social, occupational, or personal care) impairing daily life and the presence of deficits in one or more cognitive domains such as attention, executive, visuo-spatial, memory and language, and behavioral symptoms. The diagnosis of possible dementia included an atypical profile of cognitive impairment in one or more domains such as prominent or receptive-type (fluent) aphasia, or pure storage-failure type amnesia. The diagnosis of probable dementia included impairment in at least two domains such as attention, executive and/or visuo-spatial functions, and free recall memory. Probable dementia diagnosis was also reinforced by the presence of behavioral symptoms such as apathy, changes in personality and mood, hallucinations and delusions, and excessive daytime sleepiness. All subjects provided informed written consent, and the Hospital Virgen del Rocío ethics committee approved this study.

Genetics

Genomic DNA was extracted from peripheral blood samples using the standard methods. All patients underwent genotyping for rs429358 and rs7412 (*APOE* ε2, ε3, and ε4), rs9468 (*MAPT* H1 vs. H2), rs4680 (*COMT* Val158Met), and rs356219 (*SNCA*). Genotyping was performed with TaqMan SNP Genotyping Assay in a LightCycler480 (Roche Applied Science), and the genotyping success rate was over 98%. All patients were also screened for variants in the entire gene *GBA*, using both high-resolution melting analysis for all exons and direct DNA resequencing for those samples showing abnormal melting profiles. Of the 298 subjects, we identified 62 *GBA* variants in a total of 48 carriers. Identified variants were classified as potential deleterious (n=35) or potential benign

(n=27) (see Table S1) based on *in silico* analyses using the bioinformatic tools Grantham score, Polyphen-2, MutPred v1.2, and Mutation Taster. PD patients were classified into the group of "benign" if all the carried variants were potentially benign (n=17), and classified into the group of "deleterious" if at least one of the carried variants was potentially deleterious (n=31). A more detailed description about the sequencing procedure, variants and criteria for assessing pathogenicity can be found in a recent work from our group (Jesus et al., 2016).

SPECT imaging

The acquisition procedure and SPECT reconstruction can be found in a previous report (Huertas-Fernandez et al., 2015). SPECT images were processed with standard procedures in SPM8 using a homemade [^{123}I]FP-CIT template (http://www.nitrc.org/projects/spmtemplates). Quantitative analyses were based on volumes of interest in the striatum manually drawn by expert nuclear-medicine specialists (https://www.nitrc.org/projects/striatalvoimap) following established methodology (Oh et al., 2012). A volume in the occipital cortex was used as a reference region and, for each patient, [^{123}I]FP-CIT binding potential (BP) for posterior putamen and head of caudate was calculated. The BP was expressed as the percentage of age-expected binding with respect to 184 normal scans (age range 18–90 years) (Pirker, 2003), and since laterality can affect the statistics at the group level, the comparisons were made for the more affected side.

Statistical analysis

We investigated the role of *APOE* ε2 and ε4 alleles; *MAPT* H1 and H2 haplotypes; *COMT* Met allele; *SNCA* G allele; and deleterious and benign variants in *GBA*. Based on the previous reported genotypes of risk in the literature, the comparisons of interest in this study were: *APOE*: ε2+ vs. (ε2-, ε4-) and ε4+ vs (ε2-, ε4-); *MAPT*: H1/H1 vs. H2; *COMT*: Met/Met vs. Val; *SNCA*: G vs. A; *GBA*: GBA+ vs. non carriers. Other potential genetic models were also explored (allelic, dominant and recessive), but for the sake of simplicity only the contrasts of interest and/or the strongest associations are presented. We performed separate linear regression analyses for each gene and imaging variable to study their potential interaction with PLINK (http://pngu.mgh.harvard.edu/~purcell/plink/). We entered the quantitative imaging variables as dependent variables, the genetic factors as independent variables and the regression coefficients were calculated as a measure of effect size. The potential confounding factors sex, age and disease duration at time of scan were also introduced as covariates. Although previous studies have shown that dopaminergic medications do not alter DAT imaging (Schillaci et al., 2005, Federoff et al., 2012), we verified with exploratory analyses that medication was not confounding striatal uptake.

The development of dementia was examined with survival analyses through Cox regression. For this analysis, we used as event variable the presence of dementia (yes/no), and as time variable the disease duration at dementia onset for the positive cases (yes) and the disease duration at the review of the records for the negative cases (no). We performed a separate regression analysis for each gene and Hazard ratios (HR) for each risk genotype were calculated adjusting for sex and age at disease onset as potential confounding factors for dementia. Analyses were done using IBM SPSS

Statistics 22.0 and the statistical threshold for significance was set to *P* < 0.05. Given that this is an exploratory study, we did not apply multiple testing penalization.

Results

Dopaminergic imaging

Distribution of genotypes and descriptive values for putamen and caudate age-expected [^{123}I]FP-CIT BP are shown in Table 1. Age at onset was similar among genotypes for each gene except for *GBA*, for which carriers of variants were younger than non-carriers (51 vs. 55 years; *P*=0.004). In linear regression analyses, we found that *APOE* ε2 allele, the minor allele 'G' in *SNCA* polymorphism, and deleterious variants in *GBA* were associated with a reduced BP in both striatal regions putamen and caudate (Table 2). Conversely, we observed higher BP in the caudate of *COMT* Met/Met carriers. Since this association could have been driven by the interaction between COMT enzyme and levodopa, we verified that there were no differences between genotype groups in the LEDD at scan with ANOVA test (Val: 278 mg/day vs. Met/Met: 331 mg/day; *P*=0.45). We also compared LEDD across genotypes for the other genetic factors and no differences were found. Lastly, we observed a trend for reduced caudate BP for H2/H2 carriers (*P*=0.06). No relationship was found between DAT availability and *APOE* ε4 allele or benign variants in *GBA*.

Table 1. Descriptive values distributed by genotype for age of onset and percentage of putamen and caudate age-expected [^{123}I]FP-CIT binding potential.

	n	AoO	Caudate	Putamen
APOE				
ε2+	32	55 ± 13	0.48 ± 0.29	0.30 ± 0.16
ε4+	60	54 ± 12	0.55 ± 0.25	0.35 ± 0.17
(ε2-,ε4-)	200	55 ± 13	0.61 ± 0.30	0.40 ± 0.19
MAPT				
H1/H1	166	54 ± 13	0.60 ± 0.31	0.39 ± 0.20
H1/H2	108	55 ± 14	0.58 ± 0.26	0.38 ± 0.16
H2/H2	20	56 ± 10	0.46 ± 0.29	0.33 ± 0.14
COMT				
Met/Met	52	57 ± 12	0.67 ± 0.30	0.43 ± 0.21
Val/Met	146	55 ± 14	0.57 ± 0.29	0.37 ± 0.17
Val/Val	98	53 ± 13	0.57 ± 0.29	0.37 ± 0.18
SNCA				
G/G	56	55 ± 14	0.53 ± 0.29	0.35 ± 0.17
A/G	149	55 ± 12	0.57 ± 0.29	0.38 ± 0.19
A/A	88	54 ± 14	0.64 ± 0.29	0.41 ± 0.17
GBA				
deleterious	31	50 ± 8	0.53 ± 0.31	0.33 ± 0.15
benign	17	52 + 11	0.58 ± 0.31	0.37 ± 0.21
non-carriers	250	55 ± 13	0.59 ± 0.29	0.38 ± 0.18

AoO: Age of disease onset

Table 2. Results for linear regressions of SPECT variables corrected for sex, age and disease duration.

	Caudate		Putamen	
	β (95% CI)	p	β (95% CI)	p
APOE				
ε2+ vs (ε2-,ε4-)	-0.13 (-0.22,-0.02)	**0.01**	-0.18 (-0.25,-0.05)	**0.002**
ε4+ vs (ε2-,ε4-)	-0.07 (-0.13,0.03)	0.20	-0.09 (-0.14, 0.007)	0.08
MAPT				
H1/H1 vs H2	-0.007 (-0.07,0.05)	0.83	-0.001 (-0.04,0.04)	0.94
H2/H2 vs H1	-0.11 (-0.23,0.004)	0.06	-0.04 (-0.11,0.04)	0.31
COMT				
Met/Met vs Val	0.09 (0.01,0.16)	**0.03**	0.04 (-0.004,0.09)	0.07
SNCA				
G vs A	-0.06 (-0.10,-0.02)	**0.006**	-0.03 (-0.06,-0.005)	**0.02**
GBA				
deleterious vs non-carriers	-0.14 (-0.24,-0.03)	**0.01**	-0.18 (-0.26,-0.07)	**0.001**
benign vs non-carriers	-0.02 (-0.16,0.11)	0.70	-0.03 (-0.17,0.09)	0.55

β:regression coefficient; CI: confidence interval

Dementia

Of the 298 patients, 59 progressed to dementia after a mean average of 10 years from disease onset. Of those, 34 met the criteria for probable dementia and 25 met those for possible dementia. The cumulated probability of dementia was 25.7%. Cox regression analyses are presented in Table 3. We found that the development of dementia was influenced by the *APOE* ε4 allele (HR=1.90; *P*=0.03) and *GBA* deleterious variants (HR=2.59; *P*=0.01). The hazard ratio for the patients carrying both *APOE* ε4 and *GBA* deleterious variants was even higher although it did not reach significance due to the small number of cases (n=6, HR=2.95, *P*=0.10). The survival curves for these two genetic factors and their combination are presented in Fig 1. Also, a trend for a protective effect was observed for *COMT* Met/Met (HR=0.46; *P*=0.07). Finally, no association was found for the *APOE* ε2 allele, *MAPT* H1/H1 genotype, *SNCA* polymorphism or *GBA* benign variants.

Table 3. Results for Cox regressions for the development of dementia corrected for sex and age of onset.

	HR (95% CI)	p
APOE		
ε4+	1.90 (1.05,3.44)	**0.03**
ε2+	1.19 (0.54,2.64)	0.67
(ε4-,ε2-)	Ref.	
MAPT		
H1/H1	0.83 (0.51,1.45)	0.48
H2	Ref.	
COMT		
Met/Met	0.46 (0.21,1.13)	0.07
Val	Ref.	
SNCA		
G/G	0.73 (0.35,1.59)	0.41
A	Ref.	
GBA		
deleterious	2.59 (1.16,5.76)	**0.01**
benign	1.69 (0.59,4.80)	0.32
non-carriers	Ref.	
APOE + GBA		
ε4+ and deleterious	2.95 (0.80,10.90)	0.10
non-carriers	Ref.	

HR: Hazards ratio; CI: Confidence Interval.
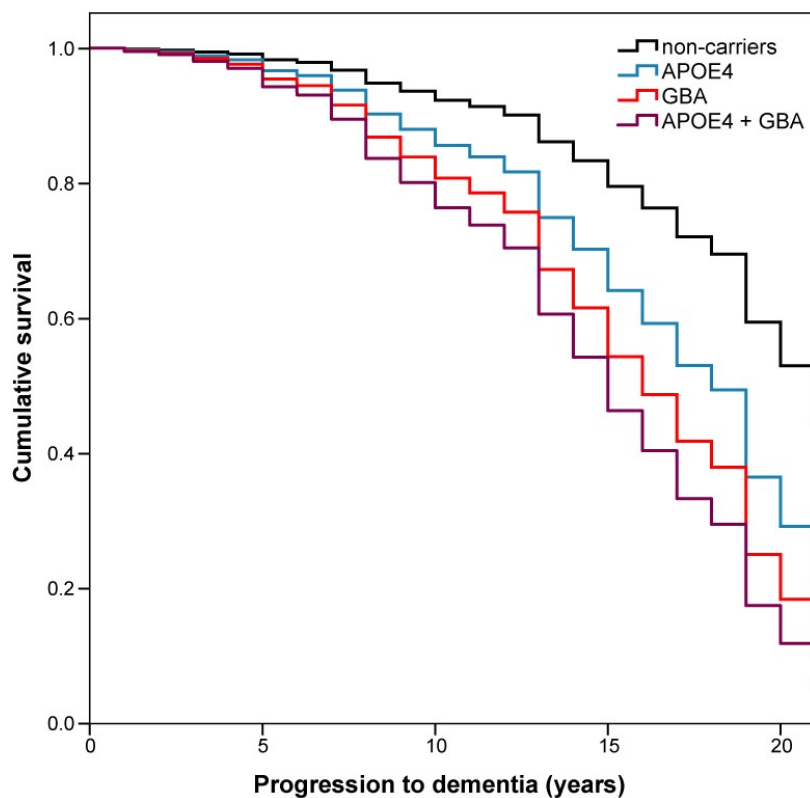
Fig 2. Survival plot of dementia onset. Lines represent the cumulative dementia-free survival in years from disease onset. GBA labels refer to patients carrying deleterious variants.

Discussion

In this study, we found that striatal DAT availability levels in PD were influenced by *APOE* ε2 allele, *COMT* Val158Met, *SNCA* rs356219 and deleterious variants in *GBA*, whereas the development of dementia was influenced by the *APOE* ε4 allele and also by deleterious variants in *GBA.* Our results therefore suggest that *APOE*2, *COMT* and *SNCA* may be related to dopaminergic degeneration, while *APOE*4 may be related to other, non-dopaminergic degeneration mechanisms, and *GBA* may be implicated in both. Our findings support the dichotomy of the *dual-syndrome* hypothesis and provide new insights into the dissociation of the genetic factors which contribute to cognitive decline in PD.

The role of *APOE*2 in PD is controversial, some studies found a higher ratio of ε2 alleles in PD patients than in controls, although other studies do not share this finding (Huang et al., 2004, Federoff et al., 2012). Similarly, the 'G' allele in *SNCA* polymorphism has been found overrepresented in PD (Goris et al., 2007). There are no previous studies investigating the relationship between these genetic factors with striatal DAT, but our results suggest that both *APOE*2 and *SNCA* could have a negative effect on the dopaminergic pathway. We also observed a trend for reduced caudate BP fot H2/H2 carriers, although this trend should be further supported by other data sets since, to the best of our knowledge, no prior data on this relationship have been reported. Hence, our results suggest that *APOE2 and SNCA* may be implicated in PD pathogenesis and lead to a faster frontoexecutive impairment. No association with dementia onset was found, which is consistent with previuos data (Williams-Gray et al., 2013), and indicate that these *loci* do not play any role in the posterior cortical syndrome. We also found increased levels of caudate DAT in Met/Met carriers of *COMT* polymorphism. This is consistent with a ^{18}F-DOPA PET study, which found higher presynaptic dopamine levels in frontal regions in Met/Met (Wu et al., 2012), and in controversy with a recent study that found higher levels of striatal FP-CIT BP in Val/Val (Muellner et al., 2015). However, this last result could be a false positive due to a small sample size (40 subjects in total, and only 3 Met/Met carriers).

We found *APOE*4 to be associated with a faster progression to dementia, but no such relationship was found for *MAPT* H1/H1. The observed effect size for *APOE* ε4 (HR=1.90) was modest in comparison to that seen in AD but consistent with an existing meta-analysis in PD, which also suggests this allele has a moderate effect on PD dementia (OR=1.74; 95% CI 1.36-2.23) (Williams-Gray et al., 2009). Consistent with our data, Mata and colleagues' recent study noted the detrimental effect of *APOE* ε4 on cognition in PD, and no effect for *MAPT* H1/H1 (Mata et al., 2014). Also, a previous study of PD in Spain discarded a relationship between *MAPT* H1/H1 and dementia (Ezquerra et al., 2008). On the other hand, a recent 10-year follow-up for the CamPaIGN cohort found a link between *MAPT* H1/H1 and dementia, and no link for *APOE* ε4 (Williams-Gray et al., 2013). However, this discrepancy concerning *APOE* ε4 could arise from a lack of power, since only 38 demented PD patients and 35 non-demented PD patients were evaluated, and ε4 frequency was higher in the case of the demented (37% vs. 26%), although it did not reach a significant level.

Interestingly, we found that deleterious variants in *GBA* were associated to both reduced striatal BP and faster progression to dementia, possibly indicating that these variants play a role in

both dopaminergic and non-dopaminergic degeneration processes. There are very few studies on dopaminergic imaging for PD *GBA* carriers, and these are limited to only a few cases;(Goker-Alpan et al., 2012, McNeill et al., 2013) as of yet, no solid conclusions have therefore been drawn on the relationship between *GBA* and the dopaminergic system. Consistent with our observations, a recent study found a reduced glucocerebrosidase enzymatic activity in the substantia nigra of *GBA* carriers (Gegg et al., 2012). Clinical studies also support our results, having observed greater motor and cognitive impairment in PD patients with deleterious *GBA* variants (e.g. L444P, N370S), including a higher risk of progressing to Hoehn and Yahr stage 3 and dementia (Winder-Rhodes et al., 2013, Brockmann et al., 2015). Moreover, a recent study found executive and visuospatial deficits in these carriers, supporting our view that *GBA* might have a double-edged role in both dopaminergic and non-dopaminergic degeneration (Mata et al., 2016). Also importantly, despite our bioinformatic analyses classified the variant E326K as benign, there are recent data suggesting the deleterious effect of E326K variant, including lower glucocerebrocidase activity (Alcalay et al., 2015) and worse performance in executive and visuospatial tasks in these carriers (Mata et al., 2016). However, our data do not support the negative role of this variant. There were 5 patients heterozygous for E326K and 4 patients with compound heterozygosis with other deleterious variants, and none of them had reduced DAT binding in comparison with analogous non-carriers nor displayed signs of dementia after a mean follow-up of 14 years. We acknowledge that our sample size is limited to make conclusions about this variant but our observations on these 9 patients do not indicate that this variant should be classified as deleterious. Lastly, we also observed that the risk of *GBA* deleterious variants carriers to develop dementia was increased in combination with *APOE4* allele. However, this is just an observation and should be interpreted with caution since we only had 6 patients having both risk genotypes (3 of them got demented, and two of them were L444P carriers). Indeed, the result is not significant due to the lack of power.

In summary, *APOE*2, *COMT* Met, 'G' allele at *SNCA* rs356219 and deleterious variants in *GBA* contribute to dopaminergic degeneration in PD. These *loci* may therefore contribute to frontostriatal dysfunction. *APOE*4 and variants in *GBA* contribute to the development of dementia, and are possibly related to other non-dopaminergic processes. Different genetic risk genotypes produce different outcomes of the dual syndromes of cognitive impairment in PD, and deleterious variants in *GBA* may play a double-edged role in both. We acknowledge that the lack of exhaustive clinical and neuropsychological assessments for dementia is a potential limitation in our study. However, this population-based study was designed to overcome limitations of sample size in genetic studies and provide reliable effect sizes. Futher research will be able to verify the findings of this discovery sample, and will allow for more convincing conclusions.

Acknowledgments

Funding disclosure

References

Aarsland D, Bronnick K, Fladby T (2011) Mild cognitive impairment in Parkinson's disease. Curr Neurol Neurosci Rep 11: 371-378.

Robbins TW, Cools R (2014) Cognitive deficits in Parkinson's disease: a cognitive neuroscience perspective. Mov Disord 29: 597-607.

Kehagia AA, Barker RA, Robbins TW (2013) Cognitive impairment in Parkinson's disease: the dual syndrome hypothesis. Neurodegener Dis 11: 79-92.

de la Fuente-Fernandez R (2013) Imaging of Dopamine in PD and Implications for Motor and Neuropsychiatric Manifestations of PD. Front Neurol 4: 90.

Brooks DJ, Piccini P (2006) Imaging in Parkinson's disease: the role of monoamines in behavior. Biol Psychiatry 59: 908-918.

Mollenhauer B, Rochester L, Chen-Plotkin A, Brooks D (2014) What can biomarkers tell us about cognition in Parkinson's disease? Mov Disord 29: 622-633.

Nombela C, Rowe JB, Winder-Rhodes SE, Hampshire A, Owen AM, et al. (2014) Genetic impact on cognition and brain function in newly diagnosed Parkinson's disease: ICICLE-PD study. Brain 137: 2743-2758.

Williams-Gray CH, Goris A, Saiki M, Foltynie T, Compston DA, et al. (2009) Apolipoprotein E genotype as a risk factor for susceptibility to and dementia in Parkinson's disease. J Neurol 256: 493-498.

Mata IF, Leverenz JB, Weintraub D, Trojanowski JQ, Hurtig HI, et al. (2014) APOE, MAPT, and SNCA genes and cognitive performance in Parkinson disease. JAMA Neurol 71: 1405-1412.

Seto-Salvia N, Clarimon J, Pagonabarraga J, Pascual-Sedano B, Campolongo A, et al. (2011) Dementia risk in Parkinson disease: disentangling the role of MAPT haplotypes. Arch Neurol 68: 359-364.

Williams-Gray CH, Mason SL, Evans JR, Foltynie T, Brayne C, et al. (2013) The CamPaIGN study of Parkinson's disease: 10-year outlook in an incident population-based cohort. J Neurol Neurosurg Psychiatry 84: 1258-1264.

Pihlstrom L, Toft M (2011) Genetic variability in SNCA and Parkinson's disease. Neurogenetics 12: 283-293.

Sidransky E, Nalls MA, Aasly JO, Aharon-Peretz J, Annesi G, et al. (2009) Multicenter analysis of glucocerebrosidase mutations in Parkinson's disease. N Engl J Med 361: 1651-1661.

Neumann J, Bras J, Deas E, O'Sullivan SS, Parkkinen L, et al. (2009) Glucocerebrosidase mutations in clinical and pathologically proven Parkinson's disease. Brain 132: 1783-1794.

Winder-Rhodes SE, Evans JR, Ban M, Mason SL, Williams-Gray CH, et al. (2013) Glucocerebrosidase mutations influence the natural history of Parkinson's disease in a community-based incident cohort. Brain 136: 392-399.

Emre M, Aarsland D, Brown R, Burn DJ, Duyckaerts C, et al. (2007) Clinical diagnostic criteria for dementia associated with Parkinson's disease. Mov Disord 22: 1689-1707; quiz 1837.

Pagonabarraga J, Kulisevsky J, Llebaria G, Garcia-Sanchez C, Pascual-Sedano B, et al. (2010) PDD-Short Screen: a brief cognitive test for screening dementia in Parkinson's disease. Mov Disord 25: 440-446.

Jesus S, Huertas I, Bernal-Bernal I, Bonilla-Toribio M, Caceres-Redondo MT, et al. (2016) GBA Variants Influence Motor and Non-Motor Features of Parkinson's Disease. PLoS One 11: e0167749.

Huertas-Fernandez I, Garcia-Gomez FJ, Garcia-Solis D, Benitez-Rivero S, Marin-Oyaga VA, et al. (2015) Machine learning models for the differential diagnosis of vascular parkinsonism and

Parkinson's disease using [(123)I]FP-CIT SPECT. Eur J Nucl Med Mol Imaging 42: 112-119.

Oh M, Kim JS, Kim JY, Shin KH, Park SH, et al. (2012) Subregional patterns of preferential striatal dopamine transporter loss differ in Parkinson disease, progressive supranuclear palsy, and multiple-system atrophy. J Nucl Med 53: 399-406.

Pirker W (2003) Correlation of dopamine transporter imaging with parkinsonian motor handicap: how close is it? Mov Disord 18 Suppl 7: S43-51.

Federoff M, Jimenez-Rolando B, Nalls MA, Singleton AB (2012) A large study reveals no association between APOE and Parkinson's disease. Neurobiol Dis 46: 389-392.

Schillaci O, Pierantozzi M, Filippi L, Manni C, Brusa L, et al. (2005) The effect of levodopa therapy on dopamine transporter SPECT imaging with(123)I-FP-CIT in patients with Parkinson's disease. Eur J Nucl Med Mol Imaging 32: 1452-1456.

Huang X, Chen PC, Poole C (2004) APOE-[epsilon]2 allele associated with higher prevalence of sporadic Parkinson disease. Neurology 62: 2198-2202.

Goris A, Williams-Gray CH, Clark GR, Foltynie T, Lewis SJ, et al. (2007) Tau and alpha-synuclein in susceptibility to, and dementia in, Parkinson's disease. Ann Neurol 62: 145-153.

Wu K, O'Keeffe D, Politis M, O'Keeffe GC, Robbins TW, et al. (2012) The catechol-O-methyltransferase Val(158)Met polymorphism modulates fronto-cortical dopamine turnover in early Parkinson's disease: a PET study. Brain 135: 2449-2457.

Muellner J, Gharrad I, Habert MO, Kas A, Martini JB, et al. (2015) Dopaminergic denervation severity depends on COMT Val158Met polymorphism in Parkinson's disease. Parkinsonism Relat Disord 21: 471-476.

Ezquerra M, Campdelacreu J, Gaig C, Compta Y, Munoz E, et al. (2008) Lack of association of APOE and tau polymorphisms with dementia in Parkinson's disease. Neurosci Lett 448: 20-23.

Goker-Alpan O, Masdeu JC, Kohn PD, Ianni A, Lopez G, et al. (2012) The neurobiology of glucocerebrosidase-associated parkinsonism: a positron emission tomography study of dopamine synthesis and regional cerebral blood flow. Brain 135: 2440-2448.

McNeill A, Wu RM, Tzen KY, Aguiar PC, Arbelo JM, et al. (2013) Dopaminergic neuronal imaging in genetic Parkinson's disease: insights into pathogenesis. PLoS One 8: e69190.

Gegg ME, Burke D, Heales SJ, Cooper JM, Hardy J, et al. (2012) Glucocerebrosidase deficiency in substantia nigra of parkinson disease brains. Ann Neurol 72: 455-463.

Brockmann K, Srulijes K, Pflederer S, Hauser AK, Schulte C, et al. (2015) GBA-associated Parkinson's disease: reduced survival and more rapid progression in a prospective longitudinal study. Mov Disord 30: 407-411.

Mata IF, Leverenz JB, Weintraub D, Trojanowski JQ, Chen-Plotkin A, et al. (2016) GBA Variants are associated with a distinct pattern of cognitive deficits in Parkinson's disease. Mov Disord 31: 95-102.

Alcalay RN, Levy OA, Waters CC, Fahn S, Ford B, et al. (2015) Glucocerebrosidase activity in Parkinson's disease with and without GBA mutations. Brain 138: 2648-2658.

Supporting Information

Table S1. List of *GBA* variants grouped by potential pathogenicity according to *in-silico* analyses

	Allele	cDNA	Protein	Exon	n
deleterious	G195W	c.700G/T	p.Gly234Trp	7	5
	S271G	c.928A/G	p.Ser310Gly	8	2
	R262C / rs374117599	c.901C>T	p.Arg301Cys	8	1
	T369T / rs138498426	c.1224G/	p.Thr408Thr	9	1
	W312R	c.1051T>A	p.Trp351Arg	9	5
	N370S	c.1223A/G	p.Asn409Ser	10	5
	D409H	c.1342G/C	p.Asp448His	10	1
	--	c.1264_1319del55	p.Leu422fsx3	10	1
	L444P	c.1448T/C	p.Leu483Pro	11	10
	V457D	c.1487T>A	p.Val496Asp	11	2
	R496H	c.1604G>A	p.Arg535His	12	2
	Total				35
benign	--	c.116-8C/T	--	4	4
	--	c.588+7A>C	--	6	1
	I119I / rs14741115	c.474C/T	p.Ile158Ile	6	1
	L268L	c.921C/T	p.Leu307Leu	8	2
	R262H / rs140955685	c.902G/A	p.Arg301His	8	1
	T369M / rs75548401	c.1223C/T	p.Thr408Met	9	3
	E326K / rs2230288	c.1093G/A	p.Glu365Lys	9	9
	--	c.1388+10T>G	--	10	1
	T410T	c.1347G/C	p.Thr449Thr	10	1
	A446T	c.1453G>A	p.Ala485Thr	11	1
	A446A / rs199928507	c.1455A>G	p.Ala485Ala	11	1
	L449L	c.1464G/C	p.Leu488Leu	11	2
	Total				27

Machine learning models for the differential diagnosis of vascular parkinsonism and Parkinson's disease using [^{123}I]FP-CIT SPECT

Machine learning models for the differential diagnosis of vascular parkinsonism and Parkinson's disease using [123I]FP-CIT SPECT

Ismael Huertas-Fernández, MSc[1]; Francisco Javier García-Gómez, MD[2]; David García-Solís, MD[2,3]; Sonia Benítez-Rivero, MD[1]; Victor Marín-Oyaga, MD[2]; Silvia Jesús, MD, PhD[1]; María Teresa Cáceres-Redondo, MD[1], José Antonio Lojo, MD[2]; Juan Francisco Martín-Rodríguez, PhD[1]; Fátima Carrillo, MD[1]; and Pablo Mir, MD, PhD[1,3].

1. Unidad de Trastornos del Movimiento, Servicio de Neurología y Neurofisiología Clínica, Instituto de Biomedicina de Sevilla (IBiS), Hospital Universitario Virgen del Rocío/CSIC/Universidad de Sevilla, Seville, Spain.
2. Servicio de Medicina Nuclear. UDIM. Hospital Universitario Virgen del Rocío, Seville, Spain.
3. Centro de Investigación Biomédica en Red sobre Enfermedades Neurodegenerativas (CIBERNED), Spain.

Author for correspondence: Dr. Pablo Mir. Unidad de Trastornos del Movimiento. Servicio de Neurología y Neurofisiología Clínica. Hospital Universitario Virgen del Rocío. Avda. Manuel Siurot s/n. 41013 Sevilla, Spain. Tel.: +34 955923040. Fax: +34 955923101. e-mail: pmir@us.es

Word count text: 4423

Word count abstract: 274

Abstract

Purpose: The study's objective was to develop diagnostic predictive models using data from two commonly used [^{123}I]FP-CIT SPECT assessment methods: Region-of-interest (ROI) analysis and whole-brain voxel-based analysis.

Methods: We included retrospectively 80 patients with vascular parkinsonism (VP) and 164 patients with Parkinson's disease (PD) who underwent [^{123}I]FP-CIT SPECT. Nuclear-medicine specialists evaluated the scans and calculated bilateral caudate and putamen [^{123}I]FP-CIT uptake, and asymmetry index using the BRASS software. Statistical Parametric Mapping (SPM) was used to compare the radioligand uptake between both entities at the voxel level. Quantitative data from these two methods, together with potential confounding factors for dopamine transporter (DAT) availability (sex, age, disease duration and severity), were used to build predictive models following a 10-fold cross-validation scheme. Logistic regression (LR), linear discriminant analysis (LDA) and support vector machine (SVM) algorithms for ROI data, and its penalized versions for SPM data (PLR, PDA and SVM), were assessed for performance.

Results: Significant differences were found between VP and PD in the most-affected putamen and the ipsilateral caudate in the ROI analysis after covariate correction. Age, disease duration and severity were also found to be informative in feeding the statistical model. SPM localized significant reductions in [^{123}I]FP-CIT uptake in PD with respect to VP in two specular clusters comprising areas corresponding to left and right striatum. The diagnostic predictive accuracy for the LR model using ROI data was 90.3%, and 90.4% for the SVM model using SPM data.

Conclusion: The predictive models built with ROI data and SPM data from [^{123}I]FP-CIT SPECT provide great discrimination accuracy between VP and PD. An external validation using these methods would be convenient to confirm its applicability across centers.

Introduction

Vascular parkinsonism (VP) is a parkinsonian syndrome due to cerebrovascular lesions and characterized by the presence of gait difficulty, symmetrical lower body bradykinesia and postural instability, and the absence of resting tremor (FitzGerald and Jankovic, 1989, Winikates and Jankovic, 1999, Rektor et al., 2006). Although recent neuropathology and epidemiological studies have reported hallmarks distinguishing VP from idiopathic Parkinson's disease (PD), overlap in symptoms presentation is not rare and its differentiation is still a clinical challenge, especially at early stages (Hughes et al., 1992, Jellinger, 2003, Zijlmans et al., 2004, Kalra et al., 2010).

The visualization of the dopamine transporter (DAT) through the use of $[^{123}I]$FP-CIT SPECT is a commonly used tool that may help in the distinction of VP and PD. However, the status of the striatal DAT in VP is controversial due to its heterogeneity and the accuracy in the differential diagnosis is still poor (Gerschlager et al., 2002, Lorberboym et al., 2004, Kalra et al., 2010, Antonini et al., 2012, Contrafatto et al., 2012, Navarro-Otano et al., 2014). This heterogeneity has been reflected in a recent study with a large cohort that showed that the $[^{123}I]$FP-CIT SPECT of about one third of VP cases were normal, while the other two thirds were abnormal, and from which a small percent of cases overlapped the typical imaging pattern of PD (Antonini et al., 2012). Furthermore, it has been suggested that a normal scan in VP can be associated to a negative responsiveness to l-dopa treatment (Antonini et al., 2012), although this association is also currently contradictory (Zijlmans et al., 2007).

The majority of the studies including VP have evaluated $[^{123}I]$FP-CIT SPECT imaging through visual assessment according to a standardized scale (Benamer et al., 2000) or semi-quantification of striatal ligand uptake (ROI analysis). Such methods may be suboptimal for two main reasons: the specialist's introduction of a certain degree of subjectivity in the visual interpretation and in the manual ROI delineation and focusing primarily on DAT uptake in the striatum, thus missing the extent of the radioligand binding to the DAT, serotonin and noradrenergic transporters in other brain regions. In contrast, voxel-based analysis has proven to be a reliable and unbiased tool for the examination of whole-brain imaging and some studies have used it with success in the differentiation of PD from other neurodegenerative diseases (Colloby et al., 2004, Scherfler et al., 2005, Goebel et al., 2011, Nocker et al., 2012). However, voxel-based studies including VP series are still lacking.

We have recently published a detailed clinical research with a large cohort of VP and PD patients (Benitez-Rivero et al., 2013). This study presented a newly developed visual scoring system with above 94% accuracy in the distinction of VP and PD and a clustering method using ROI data that achieved an accuracy of 82%. The first objective of the present study was to build a diagnostic predictive model using the ROI data from the same dataset with improved performance and applying more adequate methodologies for problems of classification from the machine learning theory. The second objective was to conduct a whole-brain voxel-based comparison between VP and PD using Statistical Parametric Mapping (SPM) and to follow the same strategy as the ROI data for building a predictive model with the voxel data.

Materials and methods

Patients

We included a total of 80 patients with VP and a control group of 164 patients with PD seen at our center from 2006 to 2011. This is the subset of patients with digital [^{123}I]FP-CIT SPECT available from our previous work and detailed clinical information of the whole dataset was given in that study (Benitez-Rivero et al., 2013). For this study, basic features were reviewed when carrying out SPECT, i.e. sex, age, disease duration and severity measured by the Hoehn & Yahr scale (H&Y). The diagnosis of VP was made according to the diagnostic criteria proposed by Zijlmans et al. (Zijlmans et al., 2004) and the diagnosis of PD was made according to the UK Parkinson's Disease Society Brain Bank clinical diagnostic criteria (Hughes et al., 1992). This study was approved by the local ethics committee and conducted in accordance with the Declaration of Helsinki.

SPECT imaging

Patients underwent a brain SPECT scan with a dual-head rotating gamma camera (Philips Axis) fitted with LEHR fan-beam collimators. In order to block the thyroid uptake of free radioactive iodide, patients were given potassium perchlorate 500 mg orally 30 min before intravenous injection of 185 MBq of [^{123}I]FP-CIT (Ioflupane. Datscan®. GE Healthcare). Image acquisition began between 3 and 4 hours after radioligand injection. A total of 120 images of 30 seconds each over a 360° circular orbit were acquired on a 128 x 128 matrix (zoom 1.5). Reconstruction was performed by filtered back-projection using a Butterworth without attenuation nor scatter correction and further reorientation to obtain transaxial slices. Patients gave informed written consent for the [^{123}I]FP-CIT SPECT scan after a full discussion of possible risks and benefits as is the general practice in our hospital.

ROI analysis

An automatized semi-quantitative analysis was performed to evaluate specific-to-nondisplaceable [^{123}I]FP-CIT binding potential (BP$_{ND}$) using the HERMES-BRASS software (version 3.5). Regions of interest (ROI) were constructed around the right and left caudate and putamen. Patient scans were first normalized to a [^{123}I]FP-CIT mean template, and regions were drawn using a standardized 3-D volume-of-interest map. [^{123}I]FP-CIT BP$_{ND}$ for these regions and asymmetry index (AI) were calculated. We defined the most-affected side as the hemisphere with the lowest putaminal ligand uptake. ROI variables were then defined as follows: putamen and caudate ipsilateral to the most-affected side (Put_I, Cau_I), and putamen and caudate contralateral to the most-affected side (Put_C, Cau_C).

SPM analysis

A semi-quantitative whole-brain voxel-based analysis was performed using SPM8 (http://www.fil.ion.ucl.ac.uk/spm/software/spm8/) running under a Matlab environment (MathWorks, Sherborn, MA).

Raw SPECT images were first manually reoriented setting the anterior commissure as the co-ordinate's origin. Each scan was then spatially normalized into the standard stereotactic MNI (Montreal Neurological Institute) space using a [123I]FP-CIT template developed by our group and available at http://www.nitrc.org/projects/spmtemplate (Garcia-Gomez et al., 2013). This normalization algorithm comprises a 12-parameter affine transformation of the reoriented images onto the [123I]FP-CIT template image followed by estimating the nonlinear deformations between the applied images. Next, spatially normalized images were smoothed using an isotropic 8 mm full width at half-maximum isotropic Gaussian kernel (FWHM) to compensate for inter-individual anatomical variability and render the imaging data more normally distributed. Lastly, since DAT densities are known to be low in the occipital lobe and the cerebellum, a brain mask for those areas was created using automated anatomical labeling (AAL) atlas. A total of 152,673 voxels were analyzed. Clusters of a minimum of 16 (twice FWHM of the gaussian filter) contiguous voxels with a threshold of $P_{FWE} < 0.05$ corrected for multiple comparisons were considered to be statistically significant.

Data analysis

Statistical analyses were performed using the IBM SPSS Statistics 20.0 software and R. Descriptive statistics are reported with percentages, mean and standard deviation and median and interquartilic range when necessary. Scale variables were first checked for normality with Shapiro-Wilk test and homoscedasticity with Levene test.

For comparing VP and PD, chi-square test was used for sex, two-sample t-test was used for age, disease duration and mean regional [123I]FP-CIT uptake, and Mann-Whitney test was used for AI and H&Y stage. Furthermore, ROI values were entered into a logistic regression along with age, sex, disease duration and H&Y stage as covariates. Additionally, since these factors are known to influence the radioligand uptake (Erro et al., 2012, Varrone et al., 2013), interaction terms were included to check its role as effect modifiers. In the SPM analysis, the [123I]FP-CIT uptake was compared between VP and PD with a two-sample t-test contrast (VP>PD).

Moreover, due to its clinical relevance and in order to clarify the inconsistencies so far in literature, subanalyses of VP cases comparing l-dopa responders versus non-responders were performed by logistic regression for ROI data, and again by two-sample t-test contrast in SPM (VP non-responder > VP responder).

Predictive models

Predictive models using the quantitative data from the ROI and SPM analyses were built for diagnosis classification. The clinical diagnosis, as defined in the section "*Patients*", was considered "gold standard" in this study and it was used as dependent variable in the models building. For the models using ROI data, the independent variables were the significant variables from the logistic regression, while for the models using SPM data, the independent variables were the voxel's intensity values (after normalization and smoothing) contained in the significant clusters from the SPM contrasts. Significant covariates were also taken into account.

The models were assessed using a 10-fold cross-validation scheme, which randomly splits the dataset into K=10 parts, 90% is used for training and the remaining 10% for testing, for every kth=1, 2,...,10. The final model and performance results were obtained from averaging the ten runs, which were given in area under curve, accuracy, sensitivity and specificity. This strategy prevents overfitting the model with our dataset thus allowing model generalization for other centers data. All calculations were done using the R-package "caret" (http://cran.r project.org/web/packages/caret/index.html).

From a statistical point of view, the modeling of ROI data and SPM data requires different approaches. The ROI data consist of few variables, whereas the SPM data consist of hundreds of voxels values. The latter is a classical p>>N problem and must be faced with regularized algorithms, which weight the independent variables according to its information content, priorizing some and penalizing others through tunable shrinkage functions. We have opted for comparing three methods recommended elsewhere (Hastie et al., 2013): penalized logistic regression (PLR), penalized discriminant analysis (PDA) and support vector machine (SVM). The ROI data were analyzed with equivalent methods: logistic regression (LR), linear discriminant analysis (LDA) and support vector machine (SVM). Tuning parameters for the algorithms were chosen based on the package default grid of iterations.

Results

Demographic and clinical features

The demographic and clinical features are reported in Table 1. There were significant differences between VP and PD in age, disease duration and H&Y stage ($P<0.001$). These associations were consistent in the regression analysis. As already described in our previous work, our subset of VP patients were older, with higher disease duration and H&Y stage than our subset of PD patients.

Table 1 Demographic and main clinical features of VP and PD patients.

	VP (n=80)	PD (n=164)
Sex (m/f,n)	57/23	101/68
Age (years, mean ± SD)	75.11 ± 6.70	60.26 ± 10.84 [#,***]
Disease duration (years, median [IQR])	4 [2, 8]	2 [1, 4] [#,**]
H&Y stage (median [IQR])	2.5[2.5, 3]	2 [2, 2.5] [†,*]

Intergroup comparisons between VP patients and PD patients. [#]p<0.001 with t-test. [†]p<0.001 with Mann-Whitney test. [*]p<0.05, [**]p<0.01, [***]p<0.001 with logistic regression.

Discrimination between VP and PD using ROI analysis

Regional [123I]FP-CIT uptake values and intergroup statistics are summarized in Table 2. Descriptive analyses showed significantly lower [123I]FP-CIT BP_{ND} values for all four regions along with an increased AI in PD with respect to VP ($P<0.001$). Regression analysis indicated that these findings were consistent after covariate correction for the most-affected hemisphere regions (Cau_I, $P<0.001$; Put_I, $P<0.001$). None of the interaction terms reached significance.

Table 2 Mean regional putamen and caudate [123I]FP-CIT BP_{ND} in VP and PD patients.

	VP (n=80)	PD (n=164)
Cau_I (mean ± SD)	1.54 ± 0.54 [#,***]	1.06 ± 0.46
Cau_C (mean ± SD)	1.64 ± 0.49 [#]	1.23 ± 0.50
Put_I (mean ± SD)	1.20 ± 0.52 [#,***]	0.53 ± 0.30
Put_C (mean ± SD)	1.43 ± 0.52 [#]	0.78 ± 0.37
AI (median [IQR])	7.04 [3.00,18.94] [†]	20.69[8.82, 39.00]

Intergroup comparisons between VP patients and PD patients. [#]p<0.001 with t-test. [†]p<0.001 with Mann-Whitney test. [***]p<0.001 with logistic regression.

These significant variables, along with the covariates age, disease duration (DisDur) and H&Y, were further used to build the predictive models. Scatter plots with the 2-dimensional combinations of the two input factors, i.e. Cau_I, and Put_I, were inspected to ensure that linear approaches were in fact suitable to fit decision boundaries between VP and PD (Fig. 1). Cross-validation results for the three methods are shown in Table 3. LR demonstrated slight superior discrimination accuracy than SVM and LDA (accuracy = 0.903>0.899>0.898, respectively), and its equation is given by the following formula:

$$logit(diagnosis) = -14.55 - 3.92*Cau\_I + 7.29*Put\_I + 0.18*age + 0.75*H\&Y - 0.28*DisDur$$

These results indicated that, despite being a very good model, a small percentage of scans were misdiagnosed. To improve the discrimination accuracy, we established a cut-off of 80% for the class probability. In other words, we assigned a diagnosis only if the probability of belonging to that class applying the formula was above 80%. We tested the LR model in the whole dataset and accuracy was raised up to 95%, although 17% of the cases were under threshold and remained tagged as "doubtful".
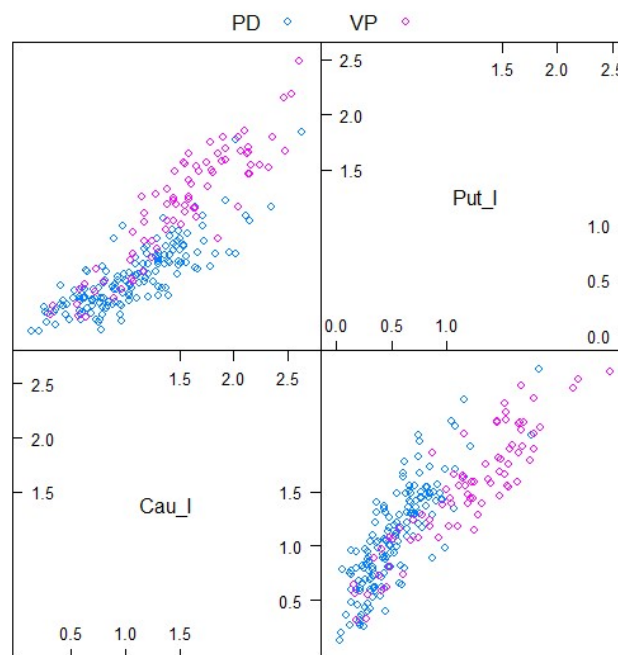
Fig. 1 Scatter plots with the 2-dimensional graphs of regional [^{123}I]FP-CIT uptakes of caudate (Cau_I) and putamen (Put_I) ipsilateral to the most-affected side, for VP and PD cases.

Table 3 Average 10-fold cross-validation performance results for the diagnostic predictive models built with ROI data, given in area under curve (AUC), accuracy, sensitivity (Sens) and specificity (Spec). The methods tested were logistic regression (LR), linear discriminant analysis (LDA) and support vector machine (SVM).

Method	AUC	Accuracy	Sens	Spec	Parameter
LR	0.951	0.903	0.944	0.794	-
LDA	0.940	0.898	0.963	0.775	-
SVM	0.950	0.899	0.947	0.784	C=1

Discrimination between VP and PD using SPM analysis

Voxel-based analysis of [123I]FP-CIT SPECTs confirmed the results of the striatal ROI analysis. SPM contrasts revealed decreased intensity values in PD patients in comparison to VP patients in two specular clusters (1113 and 1320 voxels) that comprised areas corresponding to, respectively, left and right striatum (Table 4).

Fig. 2 Voxel clusters representing significant decreases in [123I]FP-CIT uptake in PD with respect to VP. Areas comprise putamen and caudate nucleus and are represented in MNI normalized MRI scan.

Table 4 Significant findings of the SPM comparison of VP and PD (VP>PD).

Cluster localization	Cluster size	MNI co-ordinates			T value	Z value	p_{FWE}
		X	y	z			
Left striatum	1113	-26	-10	2	8.31	7.77	<0.001
		-20	14	2	5.59	5.42	<0.001
		-22	-18	4	5.46	5.29	<0.001
Right striatum	1320	28	-6	2	8.08	7.59	<0.001
		22	-16	0	5.32	5.17	0.001
		20	10	12	5.27	5.12	0.001

The predictive models were built using all intensity values of voxels contained in the significant clusters as independent variables, and the same covariates as in ROI analysis (age, disease duration and H&Y stage). Cross-validation results from penalized methods are summarized in Table 5. SVM showed slight superior accuracy in discriminating between VP and PD than PLR and LDA (accuracy = 0.904>0.887>0.884, respectively).

Table 5 Average 10-fold cross-validation performance results for the diagnostic predictive models built with SPM data, given in area under curve (AUC), accuracy, sensitivity (Sens) and specificity (Spec). The methods tested were penalized logistic regression (PLR), penalized discriminant analysis (PDA) and support vector machine (SVM).

Method	AUC	Accuracy	Sens	Spec	Parameters
PLR	0.960	0.887	0.981	0.704	α= 0.1, λ=0.1
PDA	0.878	0.884	0.944	0.769	λ=3
SVM	0.954	0.904	0.954	0.801	C=1

Comparison between l-dopa responders and non-responders

Neither logistic regression with ROI data nor SPM analysis revealed association between [123I]FP-CIT uptake and l-dopa responsiveness in VP cases.

Discussion

In this study, we have provided accurate methods for distinguishing between VP and PD using [^{123}I]FP-CIT SPECT. We developed predictive models using the quantitative data from the SPECT evaluation of a large cohort of patients via two widespread methods: striatal ROI analysis and whole-brain voxel-based analysis.

Our previous study (Benitez-Rivero et al., 2013), along with a similar multicentre study performed in Italy (Antonini et al., 2012), confirmed what previous studies have been postulating for years: vascular parkinsonism is a different and distinguishable entity from PD; however clinical manifestations and imaging patterns are heterogeneous. Nowadays, [^{123}I]FP-CIT SPECT represents a widely extended and helpful tool to aid the physician in the diagnosis of VP, and numerous studies have worked with its visual assessment and ROI quantification (Kalra et al., 2010, Tatsch and Poepperl, 2013). Some authors reported significant differences in the asymmetry index with respect to PD (Zijlmans et al., 2007, Contrafatto et al., 2012), but these studies had a small sample size and the sensitivity was as low as 50%. These results have questioned the accuracy of [^{123}I]FP-CIT SPECT for VP diagnosis, and indeed, a very recent study considered the inclusion of cardiac [^{123}I]MIBG SPECT and smell identification UPSIT test for the differential diagnosis (Navarro-Otano et al., 2014). In our previous study we used the [^{123}I]FP-CIT BP$_{ND}$ values of the most affected putamen, the ipsilateral caudate and the asymmetry index in a clustering method and achieved an accuracy of 82%. However, this approach did not exploit all the information available from the patient and contained in the image, nor provided a generalizable mathematical formula for use by other groups.

In contrast, other studies have successfully applied elegant methods for distinguishing atypical parkinsonisms and other diseases from PD with DAT SPECT imaging. Scherfler et al. used ROI analysis and SPM to extract mean voxel cluster values and introduced its parameters into a stepwise discriminant analysis (Scherfler et al., 2005). Years later, the same group elaborated a computer-assisted image algorithm (CAIA) using voxel data that outperformed a multinomial regression using ROI data (Goebel et al., 2011). In this study, we have investigated images of VP using these sorts of approaches. In the ROI analysis, in agreement with previous studies (Gerschlager et al., 2002, Contrafatto et al., 2012), we found that in PD, in comparison with VP, the striatal DAT availability is markedly reduced and the AI is significantly higher. Logistic regression revealed that the most-affected putamen and the ipsilateral caudate, along with the covariates age, disease duration and H&Y stage, were found to be informative in feeding the predictive model. Cross-validation procedures demonstrated that the algorithms LR, LDA and SVM were excellent classifiers using these variables. In the case of LR, the model obtained a diagnostic accuracy of 90.3%. Moreover, results could be improved to 95% accuracy by thresholding the class probability and creating a pool of doubtful cases. For those cases, we assumed the ROI analysis of [^{123}I]FP-CIT SPECT was inconclusive and that it would be necessary to evaluate the clinical profile and the structural neuroimaging to determine a more reliable diagnosis.

Despite the diagnostic accuracy for the newly developed visual scoring system in our previous work reaching above 94%, we acknowledge that this performance required highly trained nuclear-

medicine specialists, and that the intra and inter-observer rates were not perfect. Although we strongly encourage specialists to train and apply the new visual score, we believe that the application of the LR formula can be more easily used to achieve diagnostic accuracies above 90%. Regarding SPM, the comparison gave significant differences in [^{123}I]FP-CIT uptake in two specular clusters of voxels comprising areas of the striatum. We benefited from this huge content of information to introduce all voxel values together with the covariates into a penalized classification algorithm and found that SVM was able to achieve 90.4% accuracy. Besides, as for the ROI data, it would be possible to raise this accuracy by restricting the allocation to high class probabilities. This method demonstrated that the use of whole-brain voxel data is a powerful alternative with two great advantages with respect to the previous method: no a priori assumptions about the location of the ligand uptake and more importantly, the method are conducted in an unbiased and automated fashion.

It is also important to note that our models made use of basic clinical information, namely age, disease duration and H&Y stage. To the best of our knowledge, none of the previous studies using [^{123}I]FP-CIT SPECT for diagnostic ascertainment has included this information in their models. However, we observed that, apart from being factors directly influencing the radioligand uptake per se, they were simple and accessible but very informative parameters for the diagnosis discrimination. Hence, we recommend its inclusion in the models. We also tested if there was higher striatal ligand uptake in VP cases with negative response to l-dopa treatment versus positive responders as found by (Antonini et al., 2012). Our results were all negative for this association indicating that the [^{123}I]FP-CIT SPECT was not a good predictor of responsiveness to dopamine replacement therapy.

Finally, it is interesting to argue why these models did not reach 100% accuracy. In our opinion there might be a major limitation influencing the accuracy: our gold standard was based on clinical criteria that was blind to the SPECT, and perhaps a few cases were wrongly diagnosed. Some of the cases that were tagged as VP, even-though they fulfilled the criteria for VP when included in the study, had a PD-like pattern in the scan. It is possible that some of these patients truly had VP with an indistinguishable [^{123}I]FP-CIT SPECT from PD, while others had in reality an underlying PD accompanied with cerebrovascular damage. In that case, updating our models would entail an increase in the accuracy and therefore, a boost in the credibility of the SPECT-aided diagnosis. Nevertheless, to confirm this hypothesis it would be necessary to perform a long term follow-up to verify how these patients evolve clinically, or preferentially, an MRI scan or an anatomopathological examination in the most misleading cases.

In conclusion, this study has provided accuracies above 90% in discriminating between VP and PD via two common methods for SPECT evaluation: ROI analysis and SPM. A mathematical formula for the ROI analysis model is given in this manuscript for its evaluation by other groups. Furthermore, our study introduces a method for processing voxel-based data: the use of penalized algorithms implemented in R-packages. This approach provides an automated and therefore objective, fast and efficient solution very beneficial for the nuclear-medicine specialist decision-making. Future work regarding the inclusion of more types of Parkinsonism and its implementation in a distributable application for external evaluation will be performed.

Acknowledgments

References

Antonini A, Vitale C, Barone P, Cilia R, Righini A, Bonuccelli U, Abbruzzese G, Ramat S, Petrone A, Quatrale R, Marconi R, Ceravolo R, Stefani A, Lopiano L, Zappia M, Capus L, Morgante L, Tamma F, Tinazzi M, Colosimo C, Guerra UP (2012) The relationship between cerebral vascular disease and parkinsonism: The VADO study. Parkinsonism & related disorders 18:775-780.

Benamer TS, Patterson J, Grosset DG, Booij J, de Bruin K, van Royen E, Speelman JD, Horstink MH, Sips HJ, Dierckx RA, Versijpt J, Decoo D, Van Der Linden C, Hadley DM, Doder M, Lees AJ, Costa DC, Gacinovic S, Oertel WH, Pogarell O, Hoeffken H, Joseph K, Tatsch K, Schwarz J, Ries V (2000) Accurate differentiation of parkinsonism and essential tremor using visual assessment of [123I]-FP-CIT SPECT imaging: the [123I]-FP-CIT study group. Movement disorders : official journal of the Movement Disorder Society 15:503-510.

Benitez-Rivero S, Marin-Oyaga VA, Garcia-Solis D, Huertas-Fernandez I, Garcia-Gomez FJ, Jesus S, Caceres MT, Carrillo F, Ortiz AM, Carballo M, Mir P (2013) Clinical features and 123I-FP-CIT SPECT imaging in vascular parkinsonism and Parkinson's disease. Journal of neurology, neurosurgery, and psychiatry 84:122-129.

Colloby SJ, O'Brien JT, Fenwick JD, Firbank MJ, Burn DJ, McKeith IG, Williams ED (2004) The application of statistical parametric mapping to 123I-FP-CIT SPECT in dementia with Lewy bodies, Alzheimer's disease and Parkinson's disease. NeuroImage 23:956-966.

Contrafatto D, Mostile G, Nicoletti A, Dibilio V, Raciti L, Lanzafame S, Luca A, Distefano A, Zappia M (2012) [(123) I]FP-CIT-SPECT asymmetry index to differentiate Parkinson's disease from vascular parkinsonism. Acta neurologica Scandinavica 126:12-16.

Erro R, Pappata S, Amboni M, Vicidomini C, Longo K, Santangelo G, Picillo M, Vitale C, Moccia M, Giordano F, Brunetti A, Pellecchia MT, Salvatore M, Barone P (2012) Anxiety is associated with striatal dopamine transporter availability in newly diagnosed untreated Parkinson's disease patients. Parkinsonism & related disorders 18:1034-1038.

FitzGerald PM, Jankovic J (1989) Lower body parkinsonism: evidence for vascular etiology. Movement disorders : official journal of the Movement Disorder Society 4:249-260.

Garcia-Gomez FJ, Garcia-Solis D, Luis-Simon FJ, Marin-Oyaga VA, Carrillo F, Mir P, Vazquez-Albertino RJ (2013) [Elaboration of the SPM template for the standardization of SPECT images with 123I-Ioflupane]. Revista espanola de medicina nuclear e imagen molecular 32:350-356.

Gerschlager W, Bencsits G, Pirker W, Bloem BR, Asenbaum S, Prayer D, Zijlmans JC, Hoffmann M, Brucke T (2002) [123I]beta-CIT SPECT distinguishes vascular parkinsonism from Parkinson's disease. Movement disorders : official journal of the Movement Disorder Society 17:518-523.

Goebel G, Seppi K, Donnemiller E, Warwitz B, Wenning GK, Virgolini I, Poewe W, Scherfler C (2011) A novel computer-assisted image analysis of [123I]beta-CIT SPECT images improves the diagnostic accuracy of parkinsonian disorders. European journal of nuclear medicine and molecular imaging 38:702-710.

Hastie TJ, Tibshirani RJ, Friedman JH (2013) The elements of statistical learning : data mining, inference, and prediction. New York: Springer.

Hughes AJ, Daniel SE, Kilford L, Lees AJ (1992) Accuracy of clinical diagnosis of idiopathic Parkinson's disease: a clinico-pathological study of 100 cases. Journal of neurology, neurosurgery, and psychiatry 55:181-184.

Jellinger KA (2003) Prevalence of cerebrovascular lesions in Parkinson's disease. A postmortem study. Acta neuropathologica 105:415-419.

Kalra S, Grosset DG, Benamer HT (2010) Differentiating vascular parkinsonism from idiopathic Parkinson's disease: a systematic review. Movement disorders : official journal of the Movement Disorder Society 25:149-156.

Lorberboym M, Djaldetti R, Melamed E, Sadeh M, Lampl Y (2004) 123I-FP-CIT SPECT imaging of dopamine transporters in patients with cerebrovascular disease and clinical diagnosis of vascular parkinsonism. Journal of nuclear medicine : official publication, Society of Nuclear Medicine 45:1688-1693.

Navarro-Otano J, Gaig C, Muxi A, Lomena F, Compta Y, Buongiorno MT, Marti MJ, Tolosa E, Valldeoriola F (2014) 123I-MIBG cardiac uptake, smell identification and 123I-FP-CIT SPECT in the differential diagnosis between vascular parkinsonism and Parkinson's disease. Parkinsonism & related disorders 20:192-197.

Nocker M, Seppi K, Donnemiller E, Virgolini I, Wenning GK, Poewe W, Scherfler C (2012) Progression of dopamine transporter decline in patients with the Parkinson variant of multiple system atrophy: a voxel-based analysis of [123I]beta-CIT SPECT. European journal of nuclear medicine and molecular imaging 39:1012-1020.

Rektor I, Rektorova I, Kubova D (2006) Vascular parkinsonism--an update. Journal of the neurological sciences 248:185-191.

Scherfler C, Seppi K, Donnemiller E, Goebel G, Brenneis C, Virgolini I, Wenning GK, Poewe W (2005) Voxel-wise analysis of [123I]beta-CIT SPECT differentiates the Parkinson variant of multiple system atrophy from idiopathic Parkinson's disease. Brain : a journal of neurology 128:1605-1612.

Tatsch K, Poepperl G (2013) Nigrostriatal dopamine terminal imaging with dopamine transporter SPECT: an update. Journal of nuclear medicine : official publication, Society of Nuclear Medicine 54:1331-1338.

Varrone A, Dickson JC, Tossici-Bolt L, Sera T, Asenbaum S, Booij J, Kapucu OL, Kluge A, Knudsen GM, Koulibaly PM, Nobili F, Pagani M, Sabri O, Vander Borght T, Van Laere K, Tatsch K (2013) European multicentre database of healthy controls for [123I]FP-CIT SPECT (ENC-DAT): age-related effects, gender differences and evaluation of different methods of analysis. European journal of nuclear medicine and molecular imaging 40:213-227.

Winikates J, Jankovic J (1999) Clinical correlates of vascular parkinsonism. Archives of neurology 56:98-102.

Zijlmans J, Evans A, Fontes F, Katzenschlager R, Gacinovic S, Lees AJ, Costa D (2007) [123I] FP-CIT spect study in vascular parkinsonism and Parkinson's disease. Movement disorders : official journal of the Movement Disorder Society 22:1278-1285.

Zijlmans JC, Daniel SE, Hughes AJ, Revesz T, Lees AJ (2004) Clinicopathological investigation of vascular parkinsonism, including clinical criteria for diagnosis. Movement disorders : official journal of the Movement Disorder Society 19:630-640.

A Bayesian spatial model for neuroimaging using multiscale functional parcellations

A Bayesian spatial model for neuroimaging using

multiscale functional parcellations

Ismael Huertas,[1] Marianne Oldehinkel,[2,3] Erik S. B. van Oort,[3] David Garcia-Solis,[4,5] Pablo Mir,[1,5] Christian F. Beckmann,[2,3,6+] Andre F. Marquand[2,3,7*+]

1: Instituto de Biomedicina de Sevilla (IBiS), Hospital Universitario Virgen del Rocío / CSIC / Universidad de Sevilla, Seville, Spain

2: Department of Cognitive Neuroscience, Radboud University Medical Centre, Nijmegen, the Netherlands

3: Donders Centre for Cognitive Neuroimaging, Donders Institute for Brain, Cognition and Behaviour, Radboud University, Nijmegen, the Netherlands

4: Servicio de Medicina Nuclear. UDIM. Hospital Universitario Virgen del Rocío, Seville, Spain

5: Centro de Investigación Biomédica en Red sobre Enfermedades Neurodegenerativas (CIBERNED), Spain.

6: Oxford Centre for Functional Magnetic Resonance Imaging of the Brain (FMRIB), University of Oxford, United Kingdom

7: Department of Neuroimaging, Centre for Neuroimaging Sciences, Institute of Psychiatry, King's College London, United Kingdom

*: Corresponding Author. Andre Marquand, Donders Centre for Cognitive Neuroimaging, Donders Institute for Brain, Cognition and Behaviour, Kapittelweg 29, 6525 EN, Nijmegen, the Netherlands. Email: a.f.marquand@fcdonders.ru.nl

+: Shared senior author

Short title: Spatial model using multiscale functional parcels

Abstract

The dominant mass-univariate approach to neuroimaging data analysis uses the voxel as the unit of computation. While convenient, voxels lack biological meaning and their size is arbitrarily determined by the resolution of the image. Moreover, mass-univariate approaches do not model spatial dependencies and result in a large number of statistical estimates which need to be corrected post-hoc. To address these shortcomings, we introduce a multivariate spatial model in which an imaged brain region is assumed to result from a linearly weighted combination of (preferably multiscale) basis functions. The model is estimated using a Bayesian framework so as to automatically find the most accurate and parsimonious combination of basis functions describing the data. We test our framework to predict quantitative SPECT images of striatal dopamine function with a variety of basis sets including generic isotropic functions, anatomical parcellations of the striatum derived from structural MRI atlases, and functional parcellations of the striatum derived from advanced temporal processing of resting state fMRI. We found that a combination of ~50 multiscale functional parcellations - and the corresponding weights - accurately represented the striatal dopamine activity, which gave a substantial reduction of the number of parameters to make inferences as compared with the number of voxels ($V = 4,622$). We also demonstrate the translational validity of our framework to develop clinical applications by constructing parsimonious and accurate models for discriminating parkinsonian disorders. As a conclusion, our spatial model constitutes an elegant alternative to voxel-based approaches in neuroimaging studies; not only are they biologically interpretable, they are also adaptive to high resolutions, represent high dimensions efficiently, and capture multi-range spatial dependencies.

Highlights:

- A multivariate spatial model using brain parcellations as basis functions is proposed
- Brain regions can be modeled as a superposition of their multiscale parcellations
- The obtained parcellations are biologically meaningful and capture spatial dependencies
- The framework allows to develop parsimonious models with accurate clinical application
- The model is computationally efficient, enhances power and adapts to high resolutions

Keywords: Multivariate GLM; Functional parcellations; Spatial statistics; Basis functions;

Spatial statistics; Dopamine transporter SPECT; Parkinsonian disorders.

Introduction

Neuroimaging techniques have become invaluable tools for clinical research and practice in many brain disorders thanks to their ability to noninvasively investigate brain structure and function with relatively high spatial resolution. Data acquisition techniques such as MRI and PET allow the rich spatial structure that emerges from interactions between brain regions to be probed in high detail. However, classical voxel-based mass-univariate methods of analysis fit an independent model for each sampled brain location (i.e. for each voxel) and do not properly account for the spatial properties of the image, effectively disregarding spatial dependencies. The assumption of independence between voxels that mass-univariate analysis entails is rarely true which means that the mass-univariate approach ignores an important source of information encoded by statistical dependencies between brain regions. Furthermore, the mass-univariate approach is also suboptimal because it generates a great number of statistical estimates that depend arbitrarily on the voxel size in the image. These need to be dealt with using complex post-hoc correction methods such as random field theory (Nichols, 2012; Worsley et al., 1996), the accuracy of which has been the subject of significant recent debate (Eklund et al 2016).

In light of these drawbacks, there have been some proposals to take spatial dependencies into account using multivariate approaches, and the field of spatial statistics offers attractive methods in this respect. Various discrete spatial models have been proposed for neuroimaging data (e.g.,Penny et al., 2005; Woolrich et al., 2004) but these generally only provide local smoothing for the parameter estimates from mass-univariate analysis. They do not accommodate long-range dependencies that are intrinsic to neuroimaging data, nor overcome the arbitrary dependence on voxel size or the intricate structure-shape relationships of the brain. A more accurate and flexible approach is the spatial mixed model, in which an additional term, called a spatial random effect, is added to the model. Here, spatial dependencies are typically modeled using a continuous (usually Gaussian) spatial random field. The covariance matrix of this term describes the spatial correlation between all locations (e.g., voxels), and the inversion of this matrix is necessary to obtain suitable estimates under this model (Wikle and Royle, 2002). The immediate problem of applying this approach to neuroimaging data is the computational burden of this calculation. Accordingly, this approach has principally been used in the context of restricted regions of interest (Bowman et al., 2008; Groves et al., 2009) although some studies have made use of data reduction techniques to approximate the underlying spatial process (Hyun et al., 2014; Zhu et al., 2014).

An efficient alternative to model high-dimensional spatial processes is the use of low rank models, in which the covariance matrix is approximated by a reduced number of basis functions (Cressie and Johannesson, 2008). These basis functions can be nonlinear functions, such as radial basis functions (RBFs), b-splines, or wavelets, that are placed all over the spatial domain. In spatial applications, multiple resolutions are typically used to capture both short and long ranges of spatial dependencies. Along this line, Gershman et al., (2011) developed a spatial modeling approach for neuroimaging data, referred to as topographic latent source analysis (TLSA). In TLSA, fMRI data are modeled as a superposition of image sources constructed from adaptive RBFs. The most important benefit of this approach is that it abstracts away from the voxel as a unit of analysis, and instead

performs inferences over underlying neuroanatomical regions. However, in TLSA generic isotropic RBFs are used that do not map cleanly onto their biological sources (i.e. bran nuclei). The approach also requires running heavy optimization machinery in order to fit a given data set.

In this work we address these problems by introducing a new family of spatial functions for neuroimaging studies that more closely reflect the underlying biology. These are based on a novel multiscale functional parcellation of the relevant brain regions derived from resting state fMRI (rsfMRI). More specifically, we propose to use a soft multiscale parcellation obtained from an advanced parcellation strategy known as instantaneous connectivity parcellation (ICP, van Oort et al 2016). Our rationale is based on emerging evidence of temporally independent, spatially overlapping, subnetworks within anatomical regions and functional networks in the human brain (Smith et al., 2012). These subnetworks are believed to represent fine-scale units of computation used by the brain for processing and therefore correspond well with biology. The ICP approach is ideally suited to derive the underlying subnetworks, ICP, is ideally suited to deriving such subnetworks, which we will use as basis functions, for three reasons: first, ICP sub-divides brain networks on the basis of fine-grained temporal similarities instead of temporally averaged correlations. Second, ICP does not impose a spatial contiguity constraint, meaning that brain regions that are not spatially adjacent can still participate in the same subnetwork and third, ICP follows a hierarchical top-down strategy for parcellation, which generates a set of parcels at different levels of granularity which allows us to model multiple ranges of spatial dependencies in the image.

We propose to represent an imaged brain region (or the whole brain) by a linearly weighted sum of basis functions. We propose to use a Bayesian framework - with automatic relevance determination of features and posterior optimization - to automatically find the best subset of bases. The resulted basis functions and the corresponding weights can be used in a second level of analysis to investigate the phenotype of the imaged subjects. To illustrate, we test our framework to predict quantitative SPECT images of the dopamine transporter (DAT) availability in the healthy striatum. DAT imaging allows assessing the integrity of presynaptic dopaminergic neurons of the nigrostriatal pathway and it is widely used in the clinical practice of movement disorders (Tatsch and Poepperl, 2013). We compare a variety of basis sets including: i) generic isotropic bisquare functions; ii) structural parcellations of the striatum derived from the Harvard-Oxford and Oxford-Imanova atlases; and iii) functional parcellations of the striatum obtained from Independent Component Analysis (ICA) and ICP processing of rsfMRI data from the Human Connectome Project (Van Essen et al., 2013). We also develop an example with a real clinical application on how to use our model to construct accurate diagnostic classifiers for parkinsonian disorders.

Our spatial model abstracts away from the voxel as the fundamental unit of analysis, it is generic, and can be adapted to investigate other brain regions and research questions. Moreover, the proposed methodology provides the additional benefits: (i) biological interpretability of the computation units – spatial functions over the voxel - in the analyses (ii) a substantial reduction in the number of parameters for making inferences in neuroimaging studies, which consequently reduces correction penalties and enhances power; (iii) a faithful representation of the complex spatial structure of neuroimaging data in low dimensions (iv) a quantification of the uncertainty in

the predictions thanks to the bayesian nature of the approach (v) a method to quantify the value of different parcellation schemes in terms of the accuracy with which they can represent neuroimaging data. In this work we propose and demonstrate the validity of ICP basis set to make inferences in functional neuroimaging. Importantly, the multiscale nature of the ICP algorithm allows to efficiently capture the multiple ranges of spatial correlation in the brain. This enables to model spatially non-stationary correlation structures and long range dependencies in the data. These are both very challenging for classical spatial statistical models, yet are inherent properties of brain organization (Glasser et al 2016).

Methods

Notational preliminaries

Throughout this section and what follows, we use bold lowercase characters to denote vectors (**a**), bold uppercase letters to denote matrices (**A**), plain letters to denote scalars (*A* or *a*), where we generally reserve lowercase letters for indexing and uppercase letters for fixed quantities.

Statistical model formulation

We use a flexible regression framework to model neuroimaging data in the spatial domain. To achieve this, we first reshape the preprocessed and masked three dimensional data volumes from each of S subjects into a vector $\mathbf{y}_s$ of dimension V, where $s = 1, \dots, S$. Our aim is to predict these data using a set of basis functions $\{\boldsymbol{\phi}_m(\mathbf{x})\}_{m=1}^{M}$, that vary over the spatial domain, $\mathbf{x}$, which for simplicity we take here to be coordinates in the Cartesian coordinate system. While these could be subject specific, here we employ a common set of basis functions across all subjects (described below). We consider that $\mathbf{y}_s$ results from a linear combination M spatial basis functions plus a noise term:

$$\mathbf{y}_s = \sum_{m=1}^{M} \mathrm{w}_{m,s}\phi_m(\mathbf{x}) + \varepsilon$$

where, $\mathbf{w}_s = \left[w_{1,s}, \dots, w_{M,s}\right]^T$ is an M-dimensional vector of regression coefficients (weights) that are specific to each subject s and are adjusted to predict the class labels as accurately as possible. ε represents additive Gaussian noise $\varepsilon \sim \mathcal{N}(0, \beta^{-1})$ with β denoting the noise precision (i.e. inverse variance).[1] In this paper, we cast this problem in the context of Bayesian hierarchical models, where prior distributions are placed over model parameters of interest. This provides several important benefits: most importantly, Bayesian models account for the uncertainty in the parameter estimates and provide implicit regularization of model parameters. They also provide a simple and elegant method to combine data from multiple subjects via a shared prior over the regression coefficients ($\mathbf{w}_s$) as outlined below.

In the first instance, we place a prior distribution over the regression coefficients only ($\mathbf{w}_s$). This yields a hierarchical generative model that can be succinctly summarized by the joint likelihood, which factorises in the following way:

$$p(\mathbf{Y}, \boldsymbol{\Phi}, \mathbf{W}|\boldsymbol{\alpha}, \beta) = \prod_{s=1}^{S} p(\mathbf{y}_s|\boldsymbol{\Phi}, \beta, \mathbf{w}_s)p(\mathbf{w}_s|\boldsymbol{\alpha}) \tag{1}$$

Here, $\boldsymbol{\Phi}$ is a $V \times M$ matrix that collects all the basis functions, $\mathbf{W} = [\mathbf{w}_1, \dots, \mathbf{w}_N]$ is an $M \times S$ matrix that collects the weight vectors for each subject and $\mathbf{Y}$ is a $V \times S$ matrix collecting the neuroimaging

---

[1] Throughout this paper it is more convenient to work with precisions and precision matrices rather than covariances and covariance matrices.

data for all subjects. We assume a Gaussian prior over the weights for each subject, such that $p(\mathbf{w}_s|\boldsymbol{\alpha}) = \mathcal{N}(\mathbf{w}_s|\boldsymbol{\mu}, \boldsymbol{\Lambda}_{\boldsymbol{\alpha}}^{-1})$. Here,the precision matrix, $\boldsymbol{\Lambda}_{\boldsymbol{\alpha}}$ (inverse covariance matrix, i.e.$\boldsymbol{\Lambda}_{\boldsymbol{\alpha}}^{-1} = \boldsymbol{\Sigma}_{\boldsymbol{\alpha}}$), is shared across subjects and we make it explicit that it depends on a vector of hyperparameters ($\boldsymbol{\alpha} = [\alpha_1, \dots, \alpha_M]^T$). Without loss of generality, we also assume that the prior mean, $\boldsymbol{\mu}$, is zero. For the model in equation (1), the precision matrix is taken to be diagonal and is parameterized with an independent parameter for each basis function (α_m) along the leading diagonal. These parameters control the precision of each basis function, constituting an 'automatic relevance determination' prior (ARD; Mackay, 1995). Under this prior, the independent parameters for each basis function allow non-informative and redundant basis functions to be down-weighted and informative ones to be emphasized in a consistent manner across subjects. We could also take this one step further and apply priors over the precision parameters that further encourage them towards sparsity, which is the basis for the relevance vector machine (Tipping, 2001). However, we consider in our case that we do not have sufficient prior knowledge as to whether we should expect the model to be sparse. Therefore, we estimate the precision parameters from the model in equation (1) in an unconstrained manner, using an empirical Bayesian approach, described in the next section. The basic set up of this model is schematized in Figure 1.

Figure 1. (A) The basic spatial model in matrix notation: the *S* neuroimaging vectors of dimension *V* (**Y**) result from a linear combination of *M* basis functions (**Φ**) and the corresponding weights (**W**). (B) Diagram of the model: DATSCAN images in the striatum are modeled as a superposition of *M* weighted striatal basis functions. A zero-mean Gaussian prior with precision α_m is placed over each weight, which determine the importance of each basis function for predicting the data.

The model specified by equation (1) is appealing due to its simplicity, but it does not fully account for the uncertainty in the parameter estimates because it places a prior distribution on the weight vector coefficients only. It also does not properly account for spatial correlations between basis functions. To address these problems, we employ a full Bayesian treatment of the problem, where weplace prior distributions over all variables of interest and explicitly model correlations between basis functions. This gives rise to a hierarchical generative model in which the joint likelihood factorises in the following way:

$$p(\mathbf{Y}, \mathbf{\Phi}, \mathbf{W}, \mathbf{\Lambda}_{\alpha}, \beta | \theta_{\beta}, \theta_{\alpha}) = p(\beta | \theta_{\beta}) p(\mathbf{\Lambda}_{\alpha} | \theta_{\alpha}) \prod_{s=1}^{S} p(\mathbf{y}_s | \mathbf{X}, \beta, \mathbf{w}_s) p(\mathbf{w}_s | \mathbf{\Lambda}_{\alpha})$$

(2)

In this case, we have extended the generative model in equation (1) to accommodate correlations between the basis functions by allowing off-diagonal entries in $\mathbf{\Lambda}_{\alpha}$ (and therefore also $\mathbf{\Sigma}_{\alpha}$).We thenplace priors over the precision matrix of the ARD coefficients ($p(\mathbf{\Lambda}_{\alpha} | \theta_{\alpha})$) and the noise precision ($p(\beta | \theta_{\beta})$) in addition to the weights, where θ_{α} and θ_{β} denote the parameters of prior distributions for $\alpha$and β. More specifically, we specify that the prior over the weights has the same Gaussian form as before: $p(\mathbf{w}_s | \mathbf{\Lambda}_{\alpha}) = \mathcal{N}(\mathbf{w}_s | \mathbf{0}, \mathbf{\Lambda}_{\alpha}^{-1})$, the prior over the ARD precision matrixhas a Wishartdistribution $p(\mathbf{\Lambda}_{\alpha} | \theta_{\alpha}) = \mathcal{W}ish(\mathbf{\Lambda}_{\alpha} | N, \mathbf{P})$where N denotes the prior degrees of freedom and $\mathbf{P}$ denotes the prior precision.[2] Finally, we specify that the prior over the regression coefficients has the form of a Gamma distribution $p(\beta | \theta_{\beta}) = \mathcal{G}am(\beta | a, b)$), where a and b are shape and rate parameters. This choice of priors greatly simplifies the inference in this model because it facilitates an efficient Gibbs sampling framework that capitalizes on the conjugacy of these distributions as described in section 2.4.

Model estimation and inference: Empirical Bayes

For both of the models considered here (equations (1) and (2)), inference proceeds by estimating the posterior distribution over all parameters of interest. This is straightforward for thebasic model specified in equation (1), because for fixed α and β the posterior distribution over $\mathbf{W}$ can be computed in closed form according to Bayes' rule. For the model in equation (1), the posterior can be written as:

$$p(\mathbf{W}|\mathbf{Y}, \mathbf{\Phi}, \alpha, \beta) = \frac{\text{likelihood} \times \text{prior}}{\text{marginal likelihood}} = \frac{\prod_S p(\mathbf{y}_s | \mathbf{\Phi}, \mathbf{w}_s, \beta) \, p(\mathbf{w}_s | \alpha)}{p(\mathbf{Y}|\mathbf{\Phi}, \alpha, \beta)}$$

---

[2]Throughout this paper, we use a parameterisation of the Wishart distribution over $D \times D$ matrices whereby $\mathcal{W}ish(\mathbf{X}|N, \mathbf{P}) = K|\mathbf{P}|^{N/2}|\mathbf{X}|^{(N-D-1)/2} \exp\left[-\frac{1}{2}\text{tr}(\mathbf{XP})\right]$, where $K^{-1} = 2^{ND/2}\pi^{D(D-1)/4} \prod_{d=1}^{D} \Gamma[(N+1-d)/2]$. Here N denotes the degrees of freedom and $\mathbf{P}$ is a symmetric, positive definite precision matrix.

It is straightforward to show (see e.g. (Bishop, 2006)) that by combining a factorised Gaussian prior and Gaussian likelihood, the posterior is also a factorisedGaussian, such that $p(\mathbf{W}|\mathbf{Y}, \mathbf{\Phi}, \alpha, \beta) = \prod_s p(\mathbf{w}_s|\mathbf{y}_s, \mathbf{\Phi}, \alpha, \beta)$.The posterior weight vector for each subject ($\mathbf{w}_s$)can then be written as:

$$p(\mathbf{w}_s|\mathbf{y}_s, \mathbf{\Phi}, \alpha, \beta) = \mathcal{N}(\mathbf{w}_s|\overline{\mathbf{w}}_s, \mathbf{A}^{-1})$$

$$\mathbf{A} = \beta\mathbf{\Phi}^{\mathrm{T}}\mathbf{\Phi} + \mathbf{\Lambda}_\alpha$$

$$\overline{\mathbf{w}}_s = \beta\mathbf{A}^{-1}\mathbf{\Phi}^{\mathrm{T}}\mathbf{y}_s \tag{3}$$

Now, in order to calculate this posterior distribution, it is necessaryestimateoptimal values for the hyperparameters α and β. For the model in Equation (1), we achieve this using an empirical Bayes, or type-II maximum likelihood approach in which we work with point estimates of the hyperparameters (Bishop, 2006; Tipping, 2004). For models with relatively small numbers of basis functions, this approach is relatively efficient, although the computational cost does not scale well to models with a large number of basis functions (see below for further details). This is done by optimising the logarithm of thedenominator of Bayes rule, namely the log marginal likelihood, with respect to the hyperparameters. The intuition behind this approach is that the marginal likelihood describes the probability of the data ($\mathbf{Y}$) after integrating out the dependence on the parameters ($\mathbf{W}$). As such, it embodies a tradeoff between model fit and model complexity and so by maximizing the marginal likelihood, one obtains an optimal balance between the two. In this case, the marginal likelihood can also be computed in closed form. This takes the following form, where we have taken advantage of the independence of subjects and have omitted the dependence on $\mathbf{\Phi}$ for notational clarity:

$$
\begin{aligned}
\log p(\mathbf{Y}|\alpha, \beta) &= \log \int p(\mathbf{Y}|\mathbf{W}, \beta)\, p(\mathbf{W}|\alpha) d\mathbf{W} \\
&= \frac{SV}{2}\log\beta - \frac{SV}{2}\log 2\pi - \frac{S}{2}\log|\mathbf{\Lambda}_\alpha| - \frac{S}{2}\log|\mathbf{A}| \\
&\quad - \frac{\beta}{2}\sum_{s=1}^{S}(\mathbf{y}_s - \mathbf{\Phi}\overline{\mathbf{w}}_s)^T(\mathbf{y}_s - \mathbf{\Phi}\overline{\mathbf{w}}_s) - \overline{\mathbf{w}}_s^T\mathbf{\Lambda}_\alpha\overline{\mathbf{w}}_s
\end{aligned}
\tag{4}
$$

To find α and β we employ a conjugate gradient optimization scheme as described in (Rasmussen and Williams, 2006). This requires the derivatives of the objective function given in equation (4), which can be found by applying standard identities for derivatives of expressions involving matrices and are given in the appendix.

There are two key insights to note from the model specified by equations (1), (3) and (4). First, equation (1) embodies the assumption that subjects are independent realizations from the same distribution. This means that while the hyperparameters are shared across a group of subjects, the

weights are estimated independently for each of S subjects. This provides a simple way to induce coupling between subjects via their shared reliance on 7a common set of hyperparameters. More generally, one could also employ multi-task learning (Bonilla et al., 2008; Caruana, 1997; Marquand et al., 2014) to couple the data from different subjects which does not require an independence assumption. However, this would be computationally costly so we do not pursue it here. Second, equation (3) shows that the posterior variance for the weights does not depend on the value of the response variables ($\mathbf{y}_s$), only on the basis functions ($\boldsymbol{\Phi}$) and noise precision (β). Since we have chosen these to be fixed across subjects, this can lead to considerable computational improvements if this is accounted for in the implementation. In other words, it is not necessary to recompute the noise precision for each subject, only the posterior mean. For the remainder of this work, we refer to the approach where the model in equation (1) is fit using by optimising the objective function in equation (4) as 'Empirical Bayes'.

Model estimation and inference: Full Bayes

For the model in equation (2), we adopt an alternative Markov chain Monte Carlo (MCMC) inference approach. This is highly desirable because it can accurately quantify the uncertainty over all variables in the model and allows a richer hierarchical model to be specified over the parameters. In more detail, we employ a blocked Gibbs sampling algorithm to estimate the full posterior distribution over quantities of interest, rather than point estimates. This is achieved by repeatedly sampling from the full conditional distribution of each block of variables conditioned on the current estimates of all the others. This breaks a complex, high-dimensional distribution into simpler, low-dimensional problems, which can be sampled by conventional methods. Moreover, we choose conjugate prior distributions for each block of parameters which means that the full conditional distribution for each block of parameters can be computed exactly and has a known distributional form, which makes them easy to sample. In more detail, for each of $t = 1, \ldots, T$ iterations in the Markov chain, we draw samples from the full conditional distributions for $\mathbf{W}$, β, and $\boldsymbol{\Lambda}_\alpha$ based on the current estimates for the other parameters. This is achieved by repeatedly sampling from the full conditional distributions given below, where we use a superscript to denote the iteration number and again suppress the dependence on $\boldsymbol{\Phi}$:

$$p(\mathbf{W}^{(t+1)}|\boldsymbol{\Lambda}_\alpha^{(t)}, \beta^{(t)}, \mathbf{Y}) = \prod_{s=1}^{S} \mathcal{N}\left(\mathbf{w}_s^{(t+1)}\middle|\overline{\mathbf{w}}_s^{(t+1)}, (\mathbf{A}^{-1})^{(t+1)}\right) \tag{5a}$$

$$p(\beta^{(t+1)}|\boldsymbol{\Lambda}_\alpha^{(t)}, \mathbf{W}^{(t)}, \mathbf{Y}) = \mathcal{G}am\left(\beta^{(t+1)}\middle|a + \frac{SV}{2}, b + \frac{1}{2}\sum_s \left(\mathbf{y}_s - \boldsymbol{\Phi}\mathbf{w}_s^{(t)}\right)^T \left(\mathbf{y}_s - \boldsymbol{\Phi}\mathbf{w}_s^{(t)}\right)\right) \tag{5b}$$

$$p(\boldsymbol{\Lambda}_\alpha^{(t+1)}|\mathbf{W}^{(t)}, \beta^{(t)}, \mathbf{Y}) = \mathcal{W}ish\left(\boldsymbol{\Lambda}_\alpha^{(t+1)}\middle|N + S, \mathbf{P} + \sum_s \mathbf{w}_s^{(t)}\left(\mathbf{w}_s^{(t)}\right)^T\right) \tag{5c}$$

For many applications, the computational cost of MCMC methods is high relative to alternative methods. However, is important to note that equation (2) is linear in the parameters. As a result, the Gibbs sampling approach described above is highly efficient and converges rapidly to the target

distribution, as will be shown below. For the remainder of this paper we will refer to the estimation of equation (2) using equations (5a-c) as 'Full Bayes'.

Spatial basis functions

In this work we consider five approaches for constructing basis functions for the spatial model. These consisted of:two data-driven functionalparcellations of the striatum based on (i) a recently developed instantaneous connectivity parcellationapproach (van Oort et al 2016) and (ii) agroup-level independent component analysis (ICA); (iii) a set of generic basis functions widely used in spatial applications (Cressie and Johannesson, 2008) plustwo anatomical parcellationsof the striatum, derived from (iv) the probability maps derived from the structural MRI-based Harvard-Oxford (HO) atlas, and finally (iv) the DTI-based Oxford-Imanova (OI) atlas. Both anatomical atlases are available in FSL (http://fsl.fmrib.ox.ac.uk/fsl). These basis sets are described next and their most important characteristics are summarized in Table 1 below:

Table 1: Summary of the different basis sets evaluated in this work

Name	Type	Data driven	Multi-scale	N basis functions
ICP	Functional	Yes	Yes	464
ICA	Functional	Yes	No	464
Bisquare	Generic	No	Yes	681
Harvard-Oxford	Structural	No	No	4
Oxford-Imanova	Structural	No	No	7

Instantaneous connectivity parcellation derived basis functions

We obtained a multiscale functional parcellation of the bilateral striatum by applying ICP to restingstate fMRI of 100 participants from the Human Connectome Project (HCP)(Van Essen et al., 2013), preprocessed using the HCP minimal processing pipelines (Glasser et al 2013). The ICP approachis described in detail elsewhere (Oldehinkel et al., 2016; van Oort et al., 2016)but we provide a brief overview here. ICP is based on the assumption that voxels that form a subregion within a larger region exhibit similar, yet slightly different time courses compared to the other voxels in the larger region. The aim of ICP is therefore to divide the larger region into smaller, functionally homogenous sub-regions based on their temporal signature.The differences between these temporal signatures may be subtle, so in order to increase sensitivity for such differences, we analyse the dynamics of the 'instantaneous' modes of connectivity, reflecting the voxel-to-region differences in functional connectivity. In essence, we amplify the differences in (groups of) voxel time series by comparing them to a shared reference, here taken to be thegrand mean average time course of the original region selected for parcellation.

Pearson correlation is the most widely used metric to quantify functional connectivity between brain regions or voxels. In such types of analysis, themeasure of association is based on temporal averaging, which hides the rich dynamic information present in resting fMRI data. With ICP, we expand upon the basic Pearson correlation by considering the sequence of events across time. This proceeds by temporally 'unfolding' the time-averaged correlation between each voxel and the reference timeseries. For normalized time-series(i.e. having zero mean and unit standard deviation)of length T, the Pearson correlation between time courses **x** and **y**can be written as the mean of the element-wise (Hadamard) product between them, i.e.:

$$\rho_{x,y} = \frac{1}{T}\sum_{t=1}^{T} x_t y_t$$

The essential intuition underlying the ICP method is that we analyse the time-resolved instantaneous connectivity between a regionally-specific reference time series and all voxels' time series within the same region.In contrast to Pearson correlation, we do not perform temporal averaging over the quantity given above. This enables us to make use of the instantaneous temporal dynamics to sub-divide the original region into a set of subregions, based on the assumption that the temporal dynamics are also spatially structured. We derive a set of spatial modes describing this structure by feeding the temporally unfolded timecourse of each voxel with the reference timecourse into a group-level independent component analysis (ICA)as implemented in the FSL MELODIC software (Jenkinson et al 2012). While we could also use this decomposition to derive a piece-wise constant parcellation (see van Oort et al, 2016), these are not well suited for use as spatial basis functions. Instead, we use a set of real-valued quantities describing the relative confidence by which each voxel can be assigned to each parcel (i.e. soft parcellation) which form the set of candidate basis functions (**Φ**) for our spatial model.

The ICP algorithm described above requires that the model order of the ICA decomposition be specified, although various approaches may be used to select the model order automatically (van Oort et al, 2016). In this work, we employ ICP do develop a multi-scale parcellation. Thus, for the striatum, we obtained subdivisions from model orders ofM_d= {2,…,30}, generating a total of M = 464 basis functions ($\sum_{d=2}^{30} M_d$).

Independent Component Analysis derived basis functions

To act as a reference method, we compared the ICP method described above to a standard group-level ICA decomposition.This allowed us to assess the value of the multi-scale nature of the ICP-derived basis set for modelling neuroimaging data.For this we estimated a group-level ICA decomposition from the resting state data derived from the bilateral striatum from the same 100 subjects from the HCP dataset and after the same preprocessing. We then estimated a group-level ICA from the concatenated data from all subjects and runs with the dimensionality fixed to the same total value as for the ICP analysis above (M = 464). This generates a large number of basis functions with spatially very focal support (i.e., each having limited spatial extent). The question of

whether the dimensionality of these two basis sets is functionally equivalent is revisited in the discussion.

Generic local bisquare basis functions

As second reference method, we evaluated the ability of a generic basis set commonly used in classical spatial applications (Cressie and Johannesson, 2008). This involves tiling multi-resolutional basis functions all over the spatial domain to capture the multiple ranges of spatial correlation (Cressie and Johannesson, 2008; Nychka et al., 2014). This reference method is therefore useful to assess the value of data-driven basis functions that aim to recapitulate the underlying biology with respect to basis functions that are simply multi-scale. Following Cressie and Johannesson (2008), we use local bisquare functions for this purpose. These take the form:

$$\phi_{m_d}(\mathbf{x}) = \begin{cases} \left[1 - \left(\frac{1}{r_d}\|\mathbf{x} - \mathbf{c}_{m_d}\|\right)^2\right]^2, & if \;\; \|\mathbf{x} - \mathbf{c}_{m_d}\| \leq r_d \\ \qquad\qquad 0 & otherwise \end{cases} \tag{6}$$
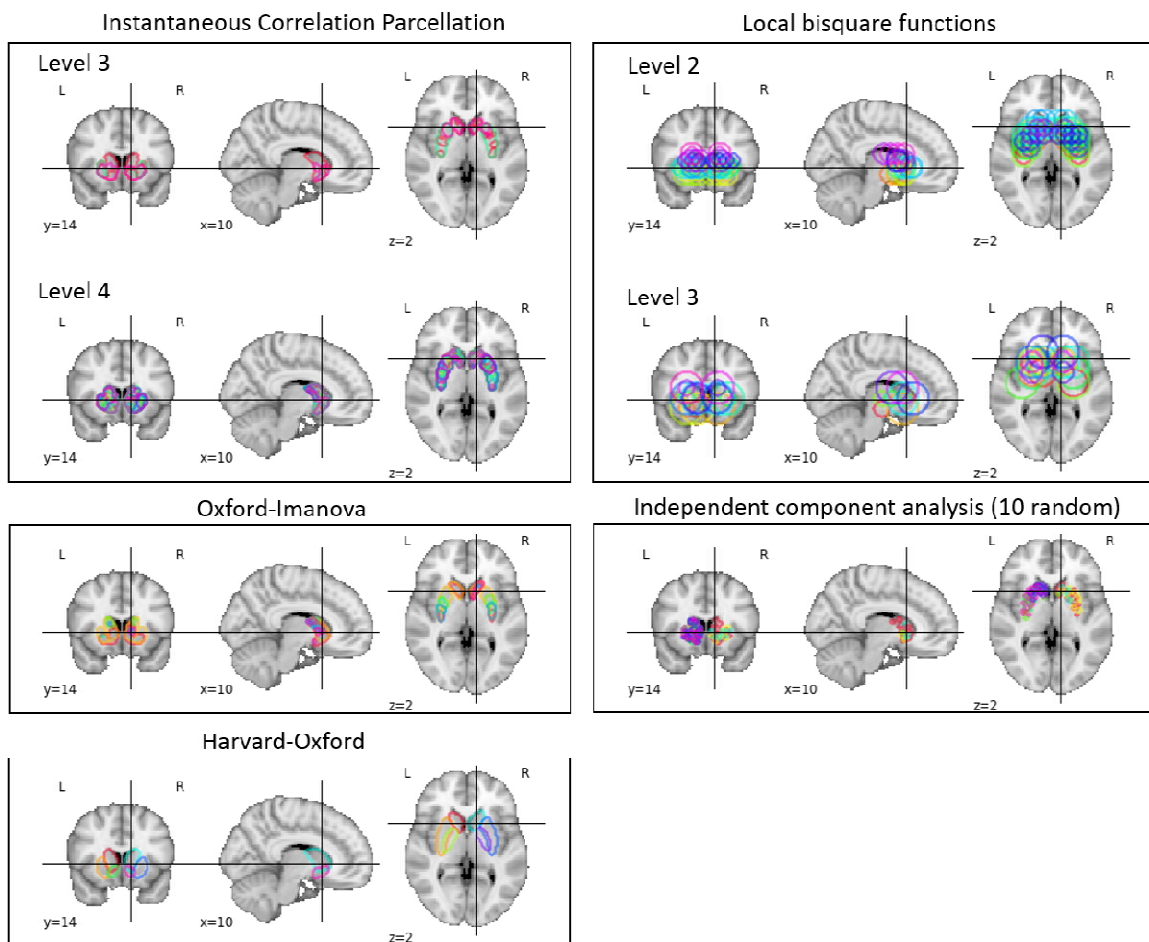
Here, the $\phi_{m_d}(\mathbf{x})$ are the individual spatially-dependent basis functions, which are indexed by $m_d = 1, \dots, M_d$ at the d-th detail level where again $M = \sum_d M_d$. The centres of each basis function are denoted by $\mathbf{c}_{m_d}$ and r_d denotes $1.5 \times$ the Euclidean distance between centre points at the d-th detail level. Intuitively, this basis function set can be considered as similar to a radial basis functions but with finite support across space. Here we choose three detail levels, having $r_d = \{6mm, 12mm, 18mm\}$, $M_d = \{589, 72, 20\}$ and therefore yielding a total of 681 basis functions. Note that the total model order is slightly higher than the model order of the data-driven basis sets, but it was not possible to obtain an exact match because it is necessary to tile the entire space with basis functions.

Anatomical basis functions

For the anatomical atlases, we used the probability maps derived from: the 4 anatomical subdivisions (left and right putamen and caudate) from the MRI-based Harvard-Oxford (HO) atlas, and the 7 subdivisions from the connectivity DTI-based Oxford-Imanova (OI) atlas, supplied with the FSL software package v.5.0.9 (http://fsl.fmrib.ox.ac.uk/fsl).

Figure 2 shows examples of the different basis sets used to model activity in the striatum. There are some characteristics that are worth commenting on: First, the soft nature of the parcellations fits with the idea that functional networks can be spatially overlapping (Smith et al., 2012). Thus, these parcellation schemes accommodate for the fact that one spatial unit may be involved in multiple, functionally relevant networks. With regard to the specific basis sets, the ICP and ICA basis sets are functional and data-driven and aim to derive the underlying units for the basis set on the basis of

the underlying functional anatomy. They differ in that ICP provides a multi-resolutional set of parcels, allowing brain units of varying sizes and with substantial spatial overlap to be combined to accurately model brain data. In contrast, the ICA basis set is derived from a single high-dimensional decomposition, so the parcels are all quite small and have lower spatial overlap. The local bisquare basis set does not use biology, but instead places basis functions across a regular grid and across multiple spatial scales. The anatomical basis sets are data-driven on the basis of structural anatomy, but are neither multi-scale nor functional. The intuition underlying these basis sets is that function to a certain extent recapitulates structure.

Instantaneous Correlation Parcellation

Level 3

Level 4

Local bisquare functions

Level 2

Level 3

Oxford-Imanova

Independent component analysis (10 random)

Harvard-Oxford

Figure 2. Basis functions used to model activity in the striatum. For the high-dimensional basis sets (independent component analysis, instantaneous connectivity parcellation and local bisquare functions), only examples are shown. Note also that the basis sets have not been masked to assist visualization.

Correlation between features

Another important consideration for the model we present here is that collinearity between predictor variables (here, basis functions) in linear regression models complicates the interpretation of the resulting regression coefficients (Kraha et al., 2012). There are two essential problems when covariates are highly collinear: (i) although unbiased, the regression coefficients

have a high variance and can therefore be sensitive to slight variations in the data. This is because there are many combinations of collinear covariates that can predict the data equally well. (ii) Care must be taken in the interpretation of high magnitude coefficients because a high magnitude coefficient can arise because a covariate is directly useful in predicting the data or because it acts as a 'suppressor' variable (Kraha et al., 2012); that is, that it helps to cancel out noise or mismatch in other covariates (Haufe et al., 2014). We perform two specific analyses to alleviate these concerns. First, we evaluate the reproducibility of the coefficients under different splits of the data, and second we present structure coefficients that show the univariate correlation between the predictors and each covariate. These are a standard tool in linear regression models to assist interpretation of regression coefficients in the presence of collinearity (Kraha et al., 2012).

Model testing

We applied our spatial model to study dopamine function in the striatum as measured by DATSCAN, which is a reliable imaging test for the identification of nigrostriatal degeneration. This scan is accurate and widely used in clinical practice for the diagnosis of Parkinson's disease (PD) and its differentiation from other movement disorders without presynaptic dopaminergic loss (e.g., essential tremor and drug-induced parkinsonism). However, the discrimination of PD from other parkinsonian disorders such as progressive supranuclear palsy (PSP) is way more challenging and current standard methods of assessments of this image do not allow to make this differential diagnosis (Tatsch and Poepperl, 2013).

We elaborate two illustrative examples in the following. We first show a proof-of-concept example in which we use our method to obtain an accurate low-dimensional representation of the striatum using DATSCAN of normal controls. Second, we develop a translational clinical example using images from different parkinsonian disorders including Parkinson's disease and progressive supranuclear palsy. We show how to use our framework to build efficient classifiers in the discrimination of these diseases.

Low-dimensional representation of the healthy striatum

In this example we sought to develop a spatial model able to accurately fit the DATSCAN of normal controls using a reduced set of basis functions and their corresponding weights. We compared the model performance in this task for the five candidate basis sets (ICP, ICA, bisquare, HO and OI).

Subjects

We included a total of 100 subjects (52% males, 60 ± 7 years) reported as normal by nuclear medicine specialists and who were scanned with [^{123}I]FP-CIT SPECT at Hospital Virgen del Rocio, Sevilla, Spain. Details about the SPECT scanner and acquisition protocol can be found in a previous work (Huertas-Fernandez et al., 2014). SPECT images were spatially normalized into standard space using a custom template (http://www.nitrc.org/projects/spmtemplates). No smoothing was applied.

Model set-up and evaluation

The bilateral striata of the scans were masked using a manually delineated region template of dimension V=4622 (https://www.nitrc.org/projects/striatalvoimap). Data from the striata of the

N=100 normal subjects were vectorised to form **Y** ($V \times N$) and intensity standardized to have zero mean and unit standard deviation. Each of these is associated with an independent weight vector, collected in the matrix **W** ($M \times N$) but were dependent on a common set of hyperparameters as decribed above. We formed **Φ** for each basis set (**Φ**$_{ICP}$, **Φ**$_{ICA}$, **Φ**$_{bisquare}$, **Φ**$_{HO}$, **Φ**$_{OI}$) and each basis function was smoothed with an 8 mm Gaussian kernel to emulate the point spread function of the SPECT scanner (Cot, et al., 2004).

We evaluated the model performance by assessing the mean cross-validated explained variance (ten repeats of split-half) as a function of the model order ($M' << M$). For the anatomical basis sets (HO and OI) the model order was fixed (4 and 7, respectively). For the other basis sets (ICP, ICA and bisquare) the basis functions were ordered by relevance based on ARD estimation in order to construct a complexity/accuracy tradeoff curve. Thus, for M'=1, the model included only the most relevant bases; for M'=20, the model included the 20 top relevant bases, etc. To check these models in greater detail, we computed a spatial Pearson correlation coefficient (*rho*) between most relevant functions to check redundancy the correlation between the α_m across the 10 splits as a measure of reproducibility.

Discrimination of parkinsonian disorders

In this example we used our framework to build spatial models with the different basis sets (ICP, ICA, bisquare, HO and OI) for classification purposes. We tested the models to discriminate the following classes: i) normal controls from PD; ii) PD (in early stages) from PSP and iii) PSP subtypes (RS vs. PAGF). We also computed the classification performance of a classical voxel-wise classifier (i.e., using all the voxels) in order to have a non-spatial approach as a reference.

Subjects
We included next to the 100 NC subjects described in the previous section, 100 patients with PD (63% males, 63 ± 12 years); 50 of them in early stage (disease duration 3 ± 2 years) and the other 50 in late stage (disease duration 13 ± 5 years); and 53 patients with PSP (73 ± 7 years; disease duration 3 ± 2 years). Forty-three of the PSP patients presented with the classical Richardson Syndrome (PSP-RS), whereas the other 10 presented with a pure akinesia and gait-freezing (PSP-PAGF) phenotype. All patients were also scanned at the same site. The diagnosis of PD was made using the UK Parkinson's Disease Society Brain Bank clinical diagnostic criteria and the PSP patients were diagnosed and labeled based on established clinical criteria (Williams et al., 2005).

Model set-up and evaluation
The model set-up pipeline was the same as for the previous example to form **Φ** for the different basis sets. We also formed the output matrix **Y** for the disease groups (i.e., **Y**$_{PD}$ and **Y**$_{PSP}$) as we did for the normal controls in the previous section. Once the matrix **W** was determined for each group, we used the weights in a second level of analyses to build the binary classifiers for the comparisons between normal controls and PD, PD (early stage) and PSP, and between the PSP subtypes (RS vs. PAGF). We used Bayesian logistic regression with ARD prior to select the most discriminating features (weights and basis functions). The classification performance was evaluated through the area under curve (AUC).

Results

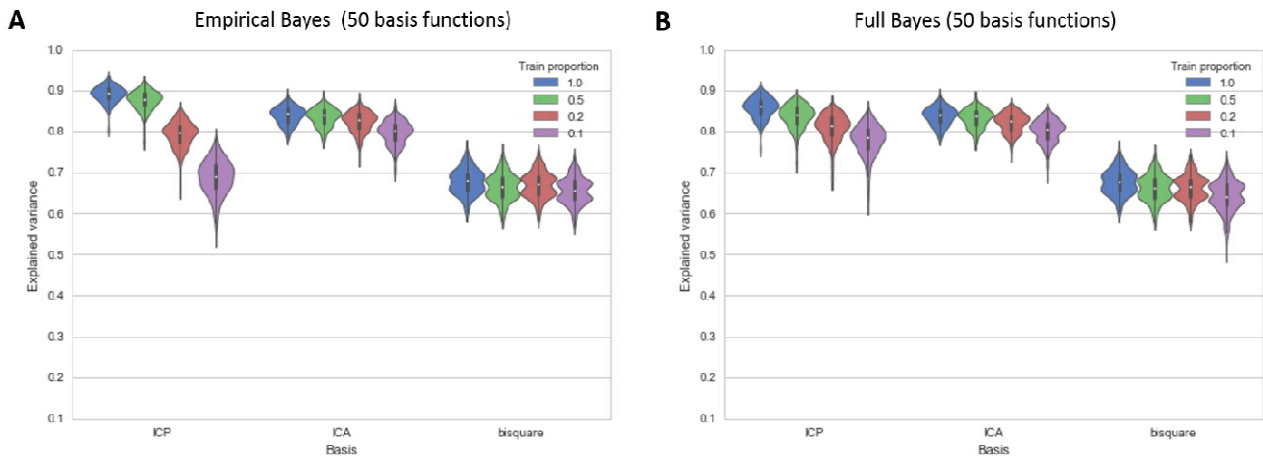## Overall performance of different basis sets and models

Dopamine function in the striatum of normal subjects scanned with DATSPECT could be highly accurately predicted ($R^2 > 90\%$) using multiple different basis sets and inference algorithms. The relative performance of the different methods is summarized in Figure 3 in terms of proportion of variance explained. This shows that: (i) all higher order basis (ICP, ICA and bisquare) sets predicted the DATSCAN data extremely accurately, whereas (ii) the anatomical basis sets were substantially less accurate; (iii) as expected, the predictive performance of all methods drops as a smaller proportion of spatial data points are available to train the model; (iv) for the ICP basis set, in which basis functions have high spatial correlation, the Empirical Bayesian approach overfits, but the full Bayesian approach does not. Finally, (v) for the full basis set, the ICA and bisquare basis sets are slightly more accurate than the ICP basis set.
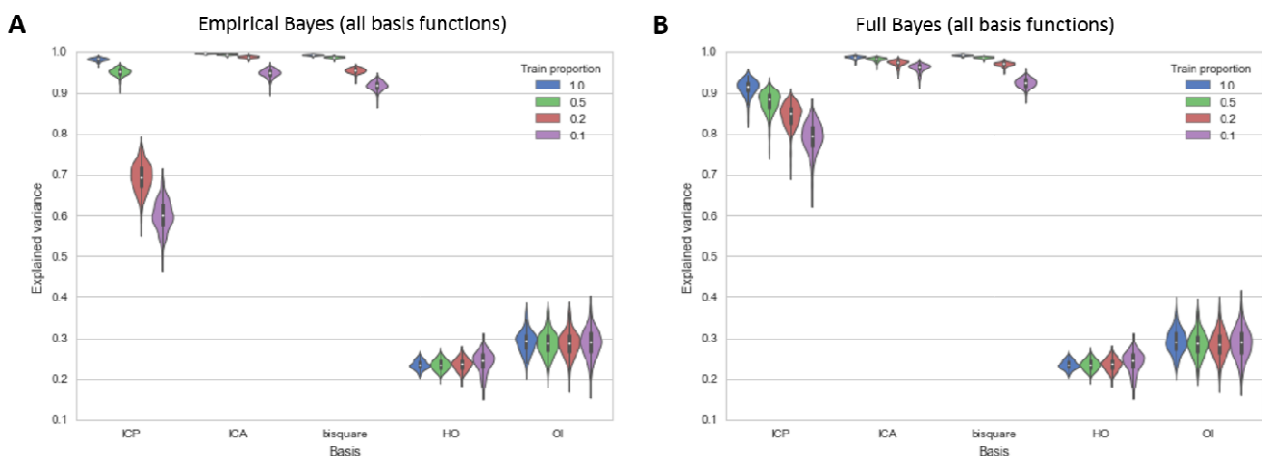
Figure 3. Total variance explained by the Empirical Bayes approach (A) and the Full Bayesian approach (B) for models with a complete set of basis functions.

Performance of different basis sets as a function of model order

It is crucial to derive a basis set that explains the data accurately and parsimoniously (i.e. using few basis functions). For example, it is reasonable to expect that more parsimonious models will lead to improved sensitivity in subsequent analyses. While there are various possible heuristics to select the most informative basis functions, a natural and effective approach is to select basis functions on the basis of their ARD coefficients, which is also the strategy employed by the relevance vector machine (Tipping, 2001). Figure 4 shows the performance of the high-order models on the basis of the 50 most informative basis functions according to this metric. In contrast to Figure 3, this shows that at lower model orders the data-driven basis sets (ICP and ICA) dominate the generic bisquare basis set, where they explain approximately 20% more variance in the data

Figure 4. Total variance explained by the Empirical Bayes approach (A) and the Full Bayesian approach (B) for models using only the top 50 basis functions.

To explore this further, we next chart the performance of the different basis sets as a function of the number of basis functions included (Figure 5). This plot was generated by sequentially adding basis functions to the model on the basis of their ARD coefficient estimated from the entire dataset. For simplicity, these models were trained using the empirical Bayes approach although similar conclusions were reached using the full Bayesian approach. This shows that at high model orders, all basis sets perform at ceiling. More importantly, Figure 5 shows that the data-driven basis sets (ICP and ICA) perform better than the generic basis set across most model orders, indicating that the data-driven basis sets give rise to more parsimonious models of brain function. Note also that the anatomical basis sets perform poorly across nearly all model orders for which they were applied. This speaks against the possibility that their poor performance is solely related to low model order. There is a relatively small difference between the different data-driven parcellations although ICP outperforms ICA both at very low model orders (< 5) and at moderate model orders (between 15-75 basis functions).
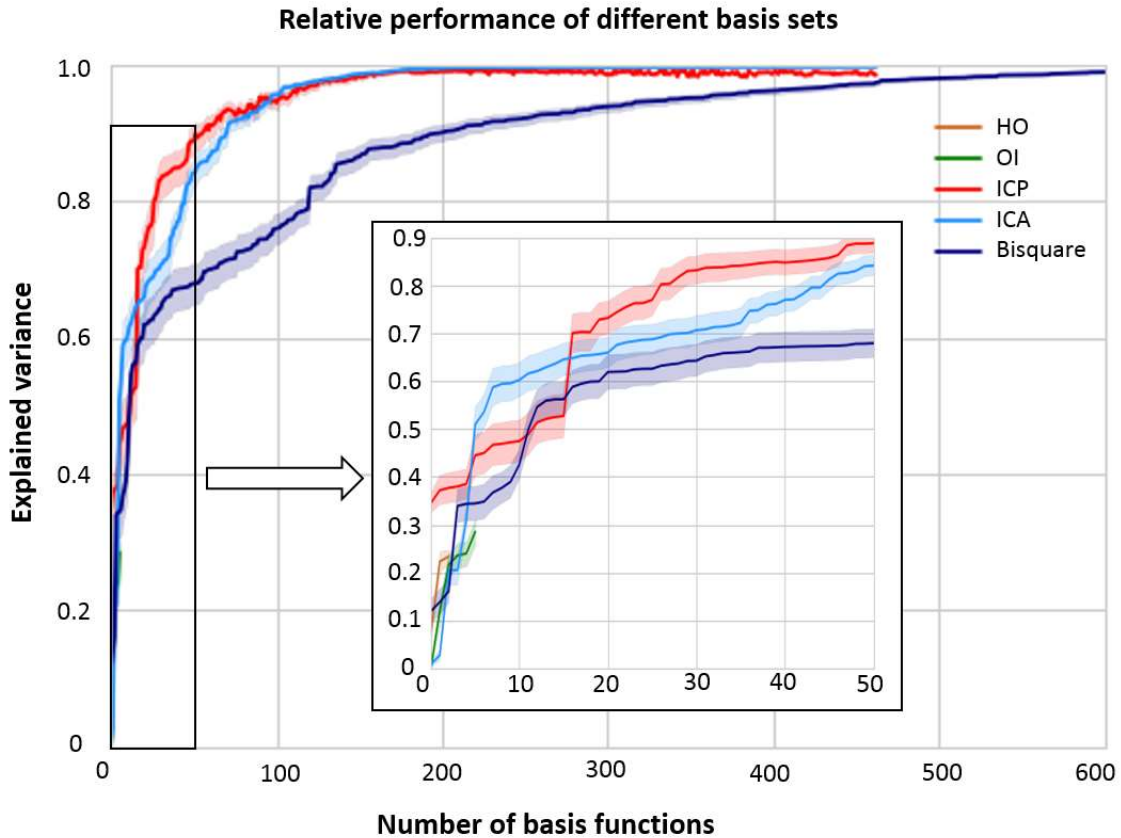
Figure 5. Explained variance (mean ± standard deviation) as a function of the number of basis functions included in the model. Inset shows a zoom on the performance of all methods at low model orders.

Low-dimensional representation of the striatum

An important benefit of this approach is to provide a low-dimensional representation of the data. As an illustrative example, the ARD coefficients from the ICP model produced a relatively sparse set of basis functions relevant for predicting striatal dopamine function. For visualization purposes, we show these by deriving a 'relevance score' from the empirical Bayesian estimates (Figure 6A), where we divide the absolute value of α_m for each basis function with respect to the maximum (α_m^{MAX}). These largely correspond with the posterior variance derived from a full Bayesian model having a diagonal covariance matrix (Figure 6B). This shows that there were relatively few basis function with high relevance (e.g., m = 1, 5, 65, and 434), and – importantly – the top ranked basis functions had also high structure coefficients (Supplementary Figure S1), which confirms the relevance of these variables for the model and rules out the possibility of these high coefficients being driven by suppressor effects.
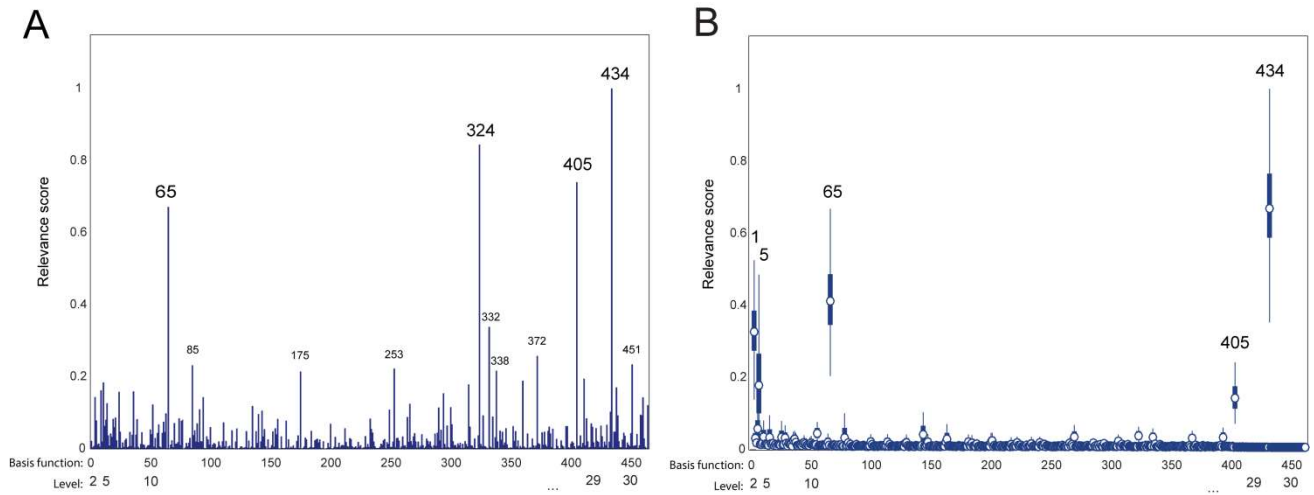
Figure 6. (A) Normalized relevance of the *M* weights using Empirical Bayes (B) Posterior variances of the weights using Full Bayes. Each weight correspond to a basis function obtained from instantaneous connectivity parcellation into into *d* = {2,…,30} levels. These different levels of parcellation are denoted by bars along the x-axis.

Figure 7 illustrates that the top-ranked basis functions largely mapped different regions of the striatum and with different spatial lengthscales (i.e. smoothness). The basis functions 1, 65 and 434 were spatially located covering major regions of the caudate, ventral striatum and putamen, respectively. Hence, the combination of these basis functions capture different spatial features and varying ranges of spatial correlation, respectively. Finally, note that there were relevant basis functions across multiple scales of parcellation.
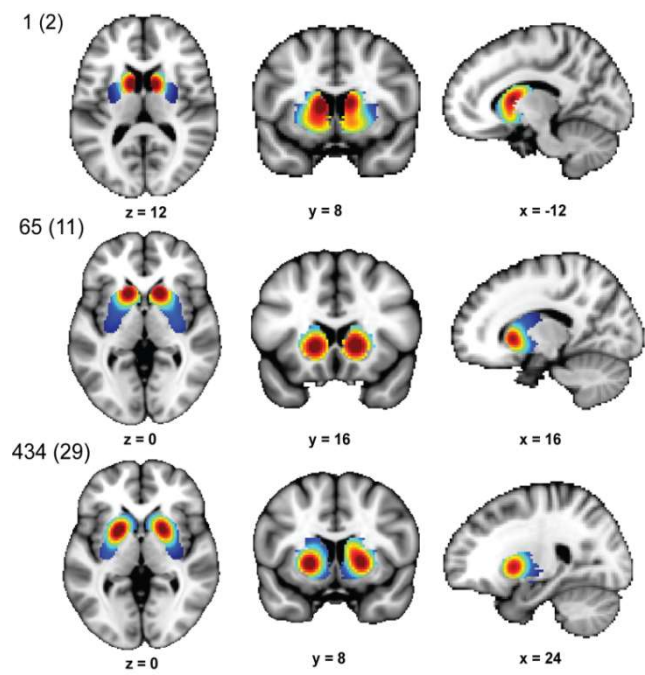
Figure 7. A selection of the top ranked basis function with coordinates given in MNI space. Notation: basis function number (level).

Discrimination of parkinsonian disorders

The area under curve for the three tested binary classifiers using the different basis set is shown in Table 2. The discrimination between PD and normal controls is a relatively straightforward classification problem on the basis of DATSCAN images and we observed that all methods performed approximately equally well at ceiling levels. The discrimination between PD and PSP is known to be very challenging using DATSCAN and this was reflected in our results. We obtained a moderate classification performance across basis sets, being the voxel approach the most accurate with AUC = 0.85. Paradoxically, when we trained the classifiers to differentiate the PSP subtypes (RS vs PAGF) we found that the voxel approach produced the worst performance (AUC = 0.45) while the ICP basis set clearly outperformed (AUC = 0.88). This suggests that some classification tasks where group differences have a strong spatial component may require from spatial methods over voxel approaches to capture these subtle spatial differences.

Table 2. Area under curve of classifiers trained to discriminate parkinsonian disorders

| Basis set	PD vs NC	PD vs PSP	RS vs PAGF
ICP	0.99	0.78	0.88
ICA	0.93	0.65	0.56
Bisquare	0.99	0.76	0.75
Harvard-Oxford	0.99	0.79	0.76
Oxford-Imanova	0.99	0.82	0.57
Raw voxels	1	0.85	0.42

One of the benefits of using brain parcellations to build basis sets is the interpretability of the discriminative features. We illustrate in Figure 8 two of the top-ranked discriminative ICP basis functions for PD and PSP. The basis functions for distinguishing PD from NC were centered on the putamen and the ventral striatum whereas for PSP (vs. PD) were rather centered on the caudate. This observation is in accordance with the distinct pattern of degeneration seen in these entities, which may be important in the development of disease biomarkers in machine learning approaches.
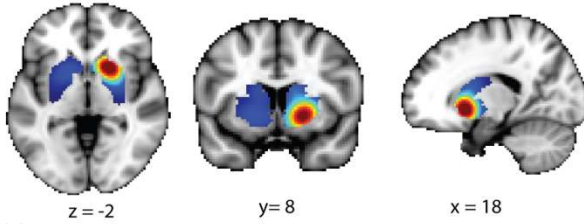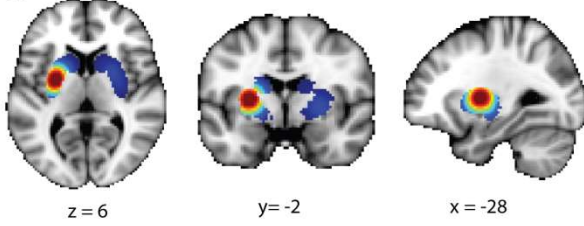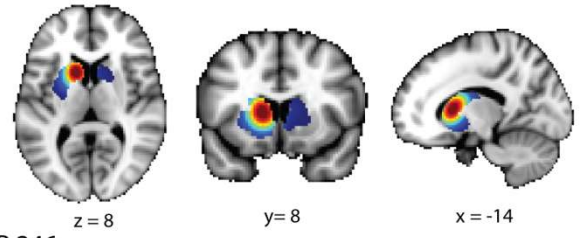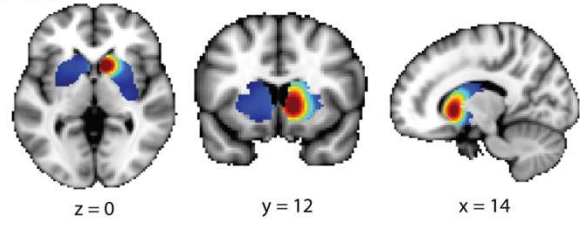
Figure 8. Representation of ICP discriminative basis functions between normal controls and Parkinson's disease and between Parkinson's disease and progressive supranuclear palsy.

Discussion

In this work we presented a new spatial modeling approach for the analysis of neuroimaging data that entails characterizing spatially distributed effects as a linear superposition of multiscale functional basis functions. This framework provides an elegant alternative to classical mass-univariate approaches and provides several advantages including: (i) a gain in interpretability since the units of analysis have a stronger biological basis relative to voxels or generic basis functions (van Oort et al., 2016); (ii) the ability to utilise information from multiple data modalities; (iii) a great reduction of the number of statistical tests, leading to enhanced statistical power and consequent benefit from high-resolution acquisitions; (iv) incorporation of multi-resolutional spatial information in the image, thus capturing not only local dependencies but also long range interactions; and (v) a method to automatically identify meaningful subregions/subnetworks. In addition, our approach provides a method by which alternative parcellation approaches can be compared quantitatively, which enabled us to demonstrate that the ICP approach we employ to create basis functions provided more accurate models of brain function for a given model order than anatomical parcellation schemes predominantly used in the field.

The gain in interpretation provided by our method comes from the fact that the units of analysis used by many current approaches (e.g., the voxel in classical mass-univariate analysis, and the RBFs employed in current spatial approaches such as TLSA) do not have a direct biological interpretation. In contrast, we propose to partition the brain into multiscale functional networks and to use these as primary regressors in the statistical analyses. This builds upon the idea that these networks can represent the elementary units of computation used by the brain. Importantly, we were able to assess this quantitatively because our approach provides a full spatial statistical model for the observed imaging data and therefore can be used to quantitatively compare different parcellation approaches (e.g. by comparing the accuracy with which different approaches can predict the observed imaging data). In this example, we showed that for a given model order, the ICP basis set provided more accurate predictions for unseen subjects than other basis sets. This result is very important and allows us to draw the following conclusions of ICP strategy for spatial models: (i) the superiority over bisquare functions reinforces our hypothesis that biologically meaningful parcellations extracted from human brain function outperform mathematically-generated generic functions; (ii) the superiority over anatomical parcellations, even at same model order, indicates that functional imaging modalities can be better explained with brain function than with brain structure. Moreover, the flexibility of fMRI processing allowed to reach higher model orders which further increased performance; (iii) the superiority of ICP over ICA, two methods extracting basis functions the from the same data, revealed the importance of the multiscale nature of ICP to build spatial models as it is recommended in spatial theory (Cressie and Johannesson, 2008); and remarkably (iv) the fact that oxygen consumption (BOLD fMRI) was accurate to explain dopamine function (DATSCAN) suggests that ICP parcellations may closely reflect the true underlying biology of human brain function.

In this work we employ soft parcellations to construct a neural basis set, which provides several advantages over the common approach of hard partitioning the brain using clustering techniques. For example, soft parcellations mitigate the risk of mixing signals from different brain regions if the definition of the spatial parcels is inaccurate and also allow one spatial unit to be involved in different networks (see e.g. Figure 1) and allow for a more gradual transition in underlying organization. We combine this with a principled method to select the most informative basis given the data and the experimental question, and further show in that these subdivisions can not only more accurately represent brain activity relative to other parcellation methods but also have a clear correspondence with physiological processes. For example, in line with the documented striatal uptake loss pattern in DATSCAN (Tatsch and Poepperl, 2013), we have seen functional parcellations located in the putamen that are discriminative for PD (vs. normal controls), and in the caudate for PSP (vs. PD). The weights associated with these basis functions can be used to investigate the association with phenotypic variables and may constitute a new potential avenue for the development of imaging biomarkers.

The reduction in the number of parameters is substantial with respect to voxel-based univariate approaches. For example, we were able to accurately model ($R^2 > 90\%$) the striatum of normal controls with only $M = 50$ basis functions ($M <<V$, where $V = 4622$). An advantage of this reduction is a lower multiple comparisons penalty and therefore a gain in statistical power. The number of basis functions and therefore the multiple comparison correction for univariate analyses will depend on the number of subdivisions conducted with ICP. For our example applications we subdivided the striatum into up to 30 parts, but this value can be different based on prior hypothesis or knowledge about the level of granularity of certain region or network. Oort et al propose to use split-half reproducibility to learn about the optimal granularity of the parcellation. In any case, the number of subdivisions will always be much lower than the number of voxels so the gain in statistical power will always be substantial. This enables the detection of effects with smaller sample sizes. Also, in contrast to voxel-based approaches, the number of parameters and consequently, the multiple comparison penalty does not increase with spatial resolution. In fact, using our method increases in spatial resolution can potentially yield spatially richer basis functions.

In addition to being highly accurate, our method is computationally efficient and highly scalable relative to other spatial statistical approaches for neuroimaging data (Bowman et al., 2008; Hyun et al., 2014; Zhu et al., 2014). For example, in TLSA, activations are modeled using radial basis functions, each of which requires both location and spatial bandwith parameters to be set resulting in many hyperparameters that have to be optimised given the data. In contrast, our set of basis functions have empirically-defined amplitudes and lengthscales and the optimisation step refers only to the hyperparameters of the weights and not to the configuration of the functions per se. As such, our approach can efficiently scale to high-resolution whole-brain prediction, where it may make use of hierarchically defined whole-brain atlases (e.g. van Oort, 2014). Another important property of our method is the improved modeling of the spatial information contained in the image. The spatial correlation between locations, especially between distant voxels, is not properly modeled by voxel-based approaches. In this sense, the multiscale nature of ICP allows to capturing

both local spatial dependencies and long-range interactions, which can yield improved sensitivity relative to voxel-wise approaches (Bowman et al 2008). This could be noted in PSP subtype classification example where the classifier using the raw voxels gave very poor performance, which may indicate that that particular classification task required from richer spatial information to detect subtle differences. However, we have seen that ICP may not always be (e.g., PD vs all PSP) the best basis set for all the applications and indeed we recommend to test our spatial model with other types of basis set for further applications. For example, fine-grained parcels obtained from ultra-high resolution MRI can be used to develop spatial models for structural MRI (Iglesias et al., 2015; Keuken et al., 2014). Multi-modal parcellation methods (e.g. Glasser et al., 2016) are also good candidates for the basis set, although such parcellations are often not multi-resolutional, which is disadvantageous for modeling spatial dependencies across multiple scales.

Finally, our approach is generic and is able to accommodate the most common types of designs and questions in neuroimaging studies. We provide a framework that can be easily applied to modeling groups of related scans so that studies involving case-control, multiple groups or task fMRI experiments can be easily accommodated. The weights (**W**) obtained can be used in further analyses to compare groups or investigate quantitative measures with parametric statistics or machine learning techniques. This provides additional benefits to those noted above, including the ability to use information encoded by spatial correlation. We demonstrated the value and the flexibility of our approach by using it to construct classifiers with different basis sets that were able to accurately distinguish PD patients from controls. This degree of accuracy is comparable to what is obtained using current procedures in the diagnostic workflow of PD and other neurodegenerative parkinsonisms (e.g. putamen quantification; Tatsch and Poepperl, 2013), so this example is only intended to validate our method using a well-established clinical application. Furthermore, our approach can also be used to provide new insights into disease mechanisms. For example, it would be interesting to use our model to investigate the correlation between the degeneration of fine striatal subnetworks with specific symptoms in parkinsonism, such as rigidity, gait disorder or dyskinesias.

In summary, in this paper we presented a methodological framework for spatial modeling in neuroimaging with multiple advantages relative to existing approaches. In future work we would like to investigate other neuroimaging modalities and other brain regions. The framework we present is very generic and can be used to explore traits or symptoms in any brain disorder from a new perspective and has high potential to lead to methods that can be translated to real clinical practice.

Appendix

The derivatives of the log marginal likelihood with respect to the hyperparameters are given below

$$\frac{\partial}{\partial \beta} \log p(\mathbf{Y}|\boldsymbol{\alpha}, \beta) \quad = \frac{SV}{2\beta} - \frac{S}{2} \text{tr}[\mathbf{A}^{-1}\boldsymbol{\Phi}^T\boldsymbol{\Phi}]$$

$$- \sum_{s=1}^{S} \frac{1}{2} \mathbf{y}_s^T \mathbf{y}_s + \frac{1}{2} \mathbf{y}_s^T \boldsymbol{\Phi}\mathbf{b}_s + \frac{1}{2} \overline{\mathbf{w}}_s^T \boldsymbol{\Phi}^T \boldsymbol{\Phi}\overline{\mathbf{w}}_s + \beta \mathbf{b}_s^T \boldsymbol{\Phi}^T \boldsymbol{\Phi}\overline{\mathbf{w}}_s$$

$$+ \mathbf{b}_s^T \boldsymbol{\Lambda}_{\boldsymbol{\alpha}} \overline{\mathbf{w}}_s$$

$$\frac{\partial}{\partial \alpha_m} \log p(\mathbf{Y}|\boldsymbol{\alpha}, \beta) \quad = -\frac{S}{2} \text{tr}\left[\boldsymbol{\Lambda}_{\boldsymbol{\alpha}} \frac{\partial \boldsymbol{\Lambda}_{\boldsymbol{\alpha}}^{-1}}{\partial \alpha_m}\right] - \frac{S}{2} \text{tr}\left[\mathbf{A}^{-1} \frac{\partial \boldsymbol{\Lambda}_{\boldsymbol{\alpha}}}{\partial \alpha_m}\right]$$

$$+ \sum_{s=1}^{S} \beta \mathbf{c}_s^T \boldsymbol{\Phi}^T \mathbf{y}_s - \beta \mathbf{c}_s^T \boldsymbol{\Phi}^T \boldsymbol{\Phi}\overline{\mathbf{w}}_s - \mathbf{c}_s^T \boldsymbol{\Lambda}_{\boldsymbol{\alpha}} \overline{\mathbf{w}}_s - \frac{1}{2} \overline{\mathbf{w}}_s^T \frac{\partial \boldsymbol{\Lambda}_{\boldsymbol{\alpha}}}{\partial \alpha_m} \overline{\mathbf{w}}_s$$

where:

$$\mathbf{b}_s = (\mathbf{I} - \beta \mathbf{A}^{-1}\boldsymbol{\Phi}^T\boldsymbol{\Phi})\mathbf{A}^{-1}\boldsymbol{\Phi}^T \mathbf{y}_s$$

$$\mathbf{c}_s = \beta \frac{\partial \mathbf{A}^{-1}}{\partial \alpha_m} \boldsymbol{\Phi}^T \mathbf{y}_s$$

Acknowledgments

Conflict of Interest

CFB is director and shareholder in SBGNeuroLtd.

References

Bishop, C.M., 2006. Pattern Recognition and Machine Learning, Pattern Recognition. doi:10.1117/1.2819119

Bonilla, E., Chai, K.M., Williams, C., 2008. Multi-task Gaussian Process Prediction. Adv. Neural Inf. Process. Syst. 20, 153–160.

Bowman, F.D., Caffo, B., Bassett, S.S., Kilts, C., 2008. A Bayesian hierarchical framework for spatial modeling of fMRI data. Neuroimage 39, 146–156. doi:10.1016/j.neuroimage.2007.08.012

Caruana, R., 1997. Multitask Learning. Mach. Learn. 28, 41–75. doi:10.1023/A:1007379606734

Cot, A., Sempau, J., Pareto, D., Bullich, S., Pavia, J., Calvino, F., Ros, D., 2004. Study of the point spread function (PSF) for 123I SPECT imaging using Monte Carlo simulation. Phys Med Biol 49, 3125–3136. doi:10.1088/0031-9155/49/14/007

Cressie, N., Johannesson, G., 2008. Fixed rank kriging for very large spatial data sets. J. R. Stat. Soc. Ser. B Stat. Methodol. 70, 209–226. doi:10.1111/j.1467-9868.2007.00633.x

Eklund, A., Nichols, T. E., Knutsson, H. 2011 Cluster failure: why fMRI inferences for spatial extent have inflated false positive rates. PNAS 113, 7900-5 doi:10.1073/pnas.1602413113

Gershman, S.J., Blei, D.M., Pereira, F., Norman, K.A., 2011. A topographic latent source model for fMRI data. Neuroimage 57, 89–100. doi:10.1016/j.neuroimage.2011.04.042

Glasser, M.F., Coalson, T.S., Robinson, E.C., Hacker, C.D., Harwell, J., Yacoub, E., Ugurbil, K., Andersson, J., Beckmann, C.F., Jenkinson, M., Smith, S.M., Van Essen, D.C., 2016. A multi-modal parcellation of human cerebral cortex. Nature 1–11. doi:10.1038/nature18933

Groves, A.R., Chappell, M.A., Woolrich, M.W., 2009. Combined spatial and non-spatial prior for inference on MRI time-series. Neuroimage 45, 795–809. doi:10.1016/j.neuroimage.2008.12.027

Guyon, I., Elisseeff, a, 2003. An introduction to variable and feature selection. J. Mach. Learn. Res. 3, 1157–1182. doi:10.1162/153244303322753616

Haufe, S., Meinecke, F., Gorgen, K., Dahne, S., Haynes, J.D., Blankertz, B., Biebmann, F., 2014. On the interpretation of weight vectors of linear models in multivariate neuroimaging. Neuroimage 87, 96–110. doi:10.1016/j.neuroimage.2013.10.067

Huertas-Fernandez, I., Garcia-Gomez, F.J., Garcia-Solis, D., Benitez-Rivero, S., Marin-Oyaga, V.A., Jesus, S., Caceres-Redondo, M.T., Lojo, J.A., Martin-Rodriguez, J.F., Carrillo, F., Mir, P., 2014. Machine learning models for the differential diagnosis of vascular parkinsonism and Parkinson's disease using [123I]FP-CIT SPECT. Eur. J. Nucl. Med. Mol. Imaging 42, 112–119. doi:10.1007/s00259-014-2882-8

Hyun, J.W., Li, Y., Gilmore, J.H., Lu, Z., Styner, M., Zhu, H., 2014. SGPP: Spatial Gaussian predictive process models for neuroimaging data. Neuroimage 89, 70–80. doi:10.1016/j.neuroimage.2013.11.018

Iglesias, J.E., Augustinack, J.C., Nguyen, K., Player, C.M., Player, A., Wright, M., Roy, N., Frosch, M.P., McKee, A.C., Wald, L.L., Fischl, B., Van Leemput, K., 2015. A computational atlas of the hippocampal formation using ex vivo, ultra-high resolution MRI: Application to adaptive segmentation of in vivo MRI. Neuroimage 115, 117–137.

doi:10.1016/j.neuroimage.2015.04.042

Keuken, M.C., Bazin, P.L., Crown, L., Hootsmans, J., Laufer, A., Muller-Axt, C., Sier, R., van der Putten, E.J., Schafer, A., Turner, R., Forstmann, B.U., 2014. Quantifying inter-individual anatomical variability in the subcortex using 7T structural MRI. Neuroimage 94, 40–46. doi:10.1016/j.neuroimage.2014.03.032

Kraha, A., Turner, H., Nimon, K., Zientek, L.R., Henson, R.K., 2012. Tools to support interpreting multiple regression in the face of multicollinearity. Front. Psychol. 3. doi:10.3389/fpsyg.2012.00044

Mackay, D., 1995. Probable networks and plausible predictions — a review of practical Bayesian methods for supervised neural networks, Network: Computation in Neural Systems. doi:10.1088/0954-898X/6/3/011

Marquand, A.F., Brammer, M., Williams, S.C.R., Doyle, O.M., 2014. Bayesian multi-task learning for decoding multi-subject neuroimaging data. Neuroimage 92, 298–311. doi:10.1016/j.neuroimage.2014.02.008

Nichols, T.E., 2012. Multiple testing corrections, nonparametric methods, and random field theory. Neuroimage 62, 811–815. doi:10.1016/j.neuroimage.2012.04.014

Nychka, D., Bandyopadhyay, S., Hammerling, D., Lindgren, F., Sain, S., 2014. A multi-resolution Gaussian process model for the analysis of large spatial data sets. J. Comput. Graph. Stat. 0. doi:10.1080/10618600.2014.914946

Oldehinkel, M., Beckmann, C.F., Pruim, R.H.R., van Oort, E.S.B., Franke, B., Hartman, C.A., Hoekstra, P.J., Oosterlaan, J., Heslenfeld, D., Buitelaar, J.K., Mennes, M., 2016. Attention-Deficit/hyperactivity disorder symptoms coincide with altered striatal connectivity. Biol. Psychiatry Cogn. Neurosci. Neuroimaging 1–11. doi:10.1016/j.bpsc.2016.03.008

Penny, W.D., Trujillo-Barreto, N.J., Friston, K.J., 2005. Bayesian fMRI time series analysis with spatial priors. Neuroimage 24, 350–362. doi:10.1016/j.neuroimage.2004.08.034

Rasmussen, E., Williams, K.I., 2006. Gaussian processes for machine learning. MIT Press 248.

Smith, S.M., Miller, K.L., Moeller, S., Xu, J., Auerbach, E.J., Woolrich, M.W., Beckmann, C.F., Jenkinson, M., Andersson, J.L.R., Glasser, M.F., Van Essen, D.C., Feinberg, D.A., Yacoub, E.S., Ugurbil, K., 2012. Temporally-independent functional modes of spontaneous brain activity. Proc. Natl. Acad. Sci. U. S. A. 109, 3131–6. doi:10.1073/pnas.1121329109

Tatsch, K., Poepperl, G., 2013. Nigrostriatal dopamine terminal imaging with dopamine transporter SPECT: an update. J. Nucl. Med. 54, 1331–8. doi:10.2967/jnumed.112.105379

Tipping, M.E., 2004. Bayesian inference: An introduction to principles and practice in machine learning. Adv. Lect. Mach. Learn. 1–19. doi:10.1162/15324430152748236

Tipping, M.E., 2001. Sparse Bayesian Learning and the Relevance Vector Machine. J. Mach. Learn. Res. 1, 211–244. doi:10.1162/15324430152748236

Van Essen, D.C., Smith, S.M., Barch, D.M., Behrens, T.E.J., Yacoub, E., Ugurbil, K., 2013. The WU-Minn Human Connectome Project: An overview. Neuroimage 80, 62–79. doi:10.1016/j.neuroimage.2013.05.041

Van Oort, E. S. B., Mennes, M., Kumar, V. J. Grodd, W., Beckman, C. F. Human brain parcellation using time courses of instantaneous correlations ArXiV, 1609.04636

Van Oort, E. S. B., Mennes, M., Beckmann, C. F. (2014) Hierarchical atlas of human functional architecture using instantaneous correlation parcellations. 20th Meeting of the Organization for Human Brain Mapping, Hamburg, Germany

Wikle, C., Royle, J., 2002. Spatial statistical modeling in biology. Mississauga, EOLSS Publ. Co. Ltd 1– 27.

Woolrich, M.W., Jenkinson, M., Brady, J.M., Smith, S.M., 2004. Fully Bayesian Spatio-Temporal Modeling of FMRI Data. IEEE Trans. Med. Imaging 23, 213–231. doi:10.1109/TMI.2003.823065

Worsley, K.J., Marrett, S., Neelin, P., Vandal, a C., Friston, K.J., Evans, a C., 1996. A unified statistical approach for determining significant voxels in images of cerebral activation. {H}uman {B}rain {M}apping 4, 58–73. doi:10.1162/NECO_a_00006-Arleo

Zhu, H., Fan, J., Kong, L., 2014. Spatially Varying Coefficient Model for Neuroimaging Data with Jump Discontinuities. J. Am. Stat. Assoc. 109, 1084–1098. doi:10.1080/01621459.2014.881742

Probabilistic intensity normalization of dopamine SPECT images via Variational mixture of Gamma distributions

Probabilistic intensity normalization of dopamine SPECT images via Variational mixture of Gamma distributions

Alberto Llera*[1], Ismael Huertas*[2], Pablo Mir[2], Christian F. Beckmann[3,4]

1: Donders Centre for Cognitive Neuroimaging, Donders Institute for Brain, Cognition and Behaviour, Radboud University, Nijmegen, the Netherlands

2: Instituto de Biomedicina de Sevilla (IBiS), Hospital Universitario Virgen del Rocío / CSIC / Universidad de Sevilla, Seville, Spain

3: Department of Cognitive Neuroscience, Radboud University Medical Centre, Nijmegen, the Netherlands

4: Oxford Centre for Functional Magnetic Resonance Imaging of the Brain (FMRIB), University of Oxford, United Kingdom

* Shared first autorship

Abstract

Dopamine transporter SPECT images show substantial variability in intensity caused not only by physiological inter-individual differeces but also by device and acquisition-related factors. However, the current standard to assess these images, based on regional quantification of the striatal uptake, does not efficiently harmonize this heterogeneity in intensity and thus these quantities can be unequivalent across Gamma cameras. In this work we present a method to intensity normalize these images. We propose to reparametrize the voxels values of a certain scan according to a mixture model of Gamma distributions learnt from healthy subjects acquired with the same camera. The reparametrization is based on the cumulative density function of the distribution modeling the specific uptake so values are re-casted into the probabilistic interval [0,1]. We found that our method equalized image intensities and, as a consequence, it improved (with respect to the current standard) the discrimination ability between Parkinson disease subjects and healthy controls when images from different cameras were pooled together. Moreover, our approach allowed the use of voxel-based classifiers that further improved performance with respect to those regional-based. Our results indicated that our normalization schema was useful to alleviate bias and facilitated the generalization of algorithms when multi-site datasets are merged. The proposed methodology may constitute a key pre-processing step in multi-center studies using this type of images.

Introduction

The imaging of the dopamine transporter (DAT) with nuclear medicine techniques, such as SPECT or PET, is a very useful and widespread tool for the diagnosis of Parkinson's disease (PD) and other neurodegenerative parkinsonisms (Tatsch and Poepperl, 2013). In these diseases, there is a progressive degeneration of the dopaminergic neurons in the nigrostriatal pathway, which projects from the substantia nigra to the striatum. DATs are located at the presynaptic nerve terminals and are responsible for reuptake of dopamine in the synapses of these neurons to the striatum. Hence, DAT imaging allows to *in-vivo* visualizing the state of these projections and thus determining the presence of neuronal degeneration (Booij et al., 2012). DATs can be imaged with molecular binding agents such as the cocaine derivative 123I-labelled 2β-carbomethoxy-3β-(4-iodophenyl)-N-(3-fluoropropyl) nortropane (^{123}I-FP-CIT or ^{123}I-ioflupane). This molecule is stable 3–6 h after its administration and best imaged 3–4 h post-injection, which makes it ideal for clinical use. In fact, its use was approved by the European Medicines Agency in 2000 and by the Food and Drug Administration in the United States in January 2011 (Djang et al., 2012).

DAT SPECT images present a high intensity variability from scan to scan caused by multiple factors, including both physiological factors such as metabolism, age and gender, and acquisition-related factors such as machine, scanning protocol and image reconstruction (Varrone et al., 2013). The current standard method of assessment of these images consists of the quantification of tracer binding in the main striatal regions of interest (ROI), namely putamen and caudate, through the calculation of the striatal binding ratio (SBR). In this calculation, the tracer binding in specific regions (i.e., the striatum) is normalized to the tracer binding in non-specific regions. The non-specific region refers to a region where the DATs are poorly expressed, commonly the occipital cortex or the cerebellum (Badiavas et al., 2011). The SBR of a particular ROI is then formulated as:

$$SBR_{ROI} = \frac{C_{ROI} - C_{NSB}}{C_{NSB}}$$

where C_{ROI} is the mean count per voxel in the ROI (whole striatum, putamen or caudate) and C_{NSB} represents the mean count per voxel in the non-specific region.

However, this ROI-based normalization schema is making assumptions about the intensity distribution in these ROIs that are not fully true and therefore this method may introduce bias. An illustrative example of this problem occurred in the European multicentre database of healthy controls for ^{123}I-FP-CIT SPECT (ENC-DAT), where different sites produced statistically significant SBR values (Varrone et al., 2013). These large SBR differences, probably caused by the use of different Gamma cameras and settings, make these values not directly comparable and consequently the variable "site" should be introduced as a covariate in further analyses to account for these differences, which is also a suboptimal choice. Furthermore, these differences may affect the reproducibility of the accuracy of neuroimaging-based machine learning algorithms out of the

tested data-set. This lack of generalization may therefore affect the reliability of software aiding clinical decision-making.

One group has made recent efforts to alleviate these inter-subject intensity differences in these images using more sophisticated voxel-based approaches and with very good results (Salas-Gonzalez et al., 2013, Brahim et al., 2014, Brahim et al., 2015). While these methods provide a substantial improvement with respect to the SBR, they were applied to subjects that were acquired at the same site. Thus, it is uncertain whether these methods deal efficiently with the larger differences that are caused by distinct acquisition pipelines. Furthermore, the normalized intensity values, although harmonized, are still dependent on the values generated by that particular acquisition set-up.

In this work we propose to reparametrize the intensity values of DAT SPECT to a fixed and universal interval [0,1] using a probabilistic normalization technique. More specifically, we propose to model a normative image histogram of a specific acquisition set-up (e.g., a site) with a mixture model of Gamma distributions using healthy subjects. Then, a certain image (also pathologic, e.g., with PD) acquired with those parameters can be fitted to that normative model to be quantified.

The Gamma distribution modeling the specific uptake region is a related measure to the probability of activation of a given voxel. We reparametrize each voxel value according to the cumulative density function of that Gamma distribution. We used images from a public repository and acquired at multiples sites to test our method. We demonstrate that our nomalization procedure brings the following benefits: i) alleviates differences across scans/sites and ii) provide a universally comparable intensity range for the measurement of the striatum tracer binding. This latter benefit is crucial not only to allow comparing numeric results across sites/studies but also to build unbiased and generalizable algorithms with these scans.

Methods

Dataset

In this work we make use of DAT SPECT images obtained from the Parkinson's Progression Markers Initiative (PPMI) repository (www.ppmi-info.org). PPMI is a public-private partnership funded by the Michael J. Fox Foundation for Parkinson's Research and funding partners. This project involves more than 30 clinical sites worldwide and DAT SPECT is one of the imaging test that are being collected. These conditions make this multi-center repository an ideal example to reflect the heterogenity of real world data and to test our method for intensity harminization. We randomly selected 1342 DAT SPECT scans corresponding to 210 healthy controls and 1132 PD patients acquired at 24 different sites. These scans were acquired with 7 different cameras from a variety of manufacturers, including: (1) MARCONI 3000XP, (2) PHILIPS BrightView, (3) SIEMENS Encore2, (4) SIEMENS IP2, (5) PICKER HERMES Workstation, (6) GE MILLENNIUM MG and (7) GE VARICAM (Table 1). All brain images were spatially normalized to MNI152 standard space using the standard procedure in FSL (http://fsl.fmrib.ox.ac.uk/fsl).

Table 1. Number of control and PD images, and sites per camera. Note: some sites have more than one camera.

	MARCONI	PHILIPS	SIEMENS		PICKER	GE	
	3000XP	BrightView	Encore2	IP2	HERMES	MILLENNIUM	VARICAM
Sites (N)	1	3	14	6	4	1	2
	Controls						
N	15	21	90	30	31	14	9
sex (M/F)	9 / 6	15 / 6	60 / 30	15 / 15	23 / 8	10 / 4	6 / 3
age (years)	60 ± 11	62 ± 13	62 ± 10	59 ± 11	61 ± 13	55 ± 13	64 ± 13
	PD						
N	179	133	494	128	108	61	29
sex (M/F)	128 / 51	65 / 68	309 / 185	97 / 31	68 / 40	44 / 17	20 / 9
age (years)	62 ± 10	68 ± 9	63 ± 10	61 ± 9	63 ± 9	60 ± 11	58 ± 11

Raw image intensity

The histogram of DAT SPECT images is characterized by a positive-valued distribution with two prominent features: i) a broad main component with positive mode bulk at low values corresponding to the background intensity, namely the non-specific uptake region; and ii) a right-skewed long tail at higher intensity values than the former and which corresponds to the activation voxels, namely the specific uptake region.
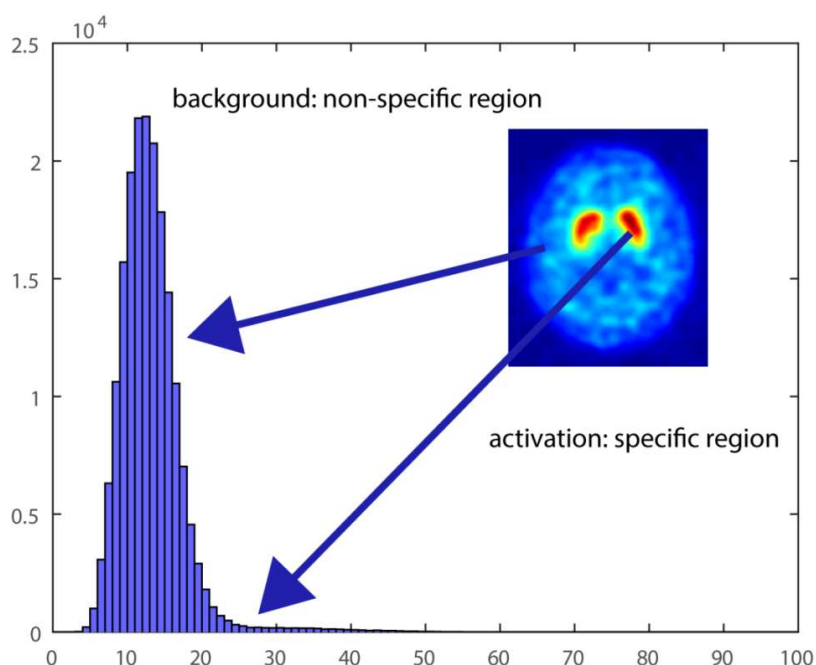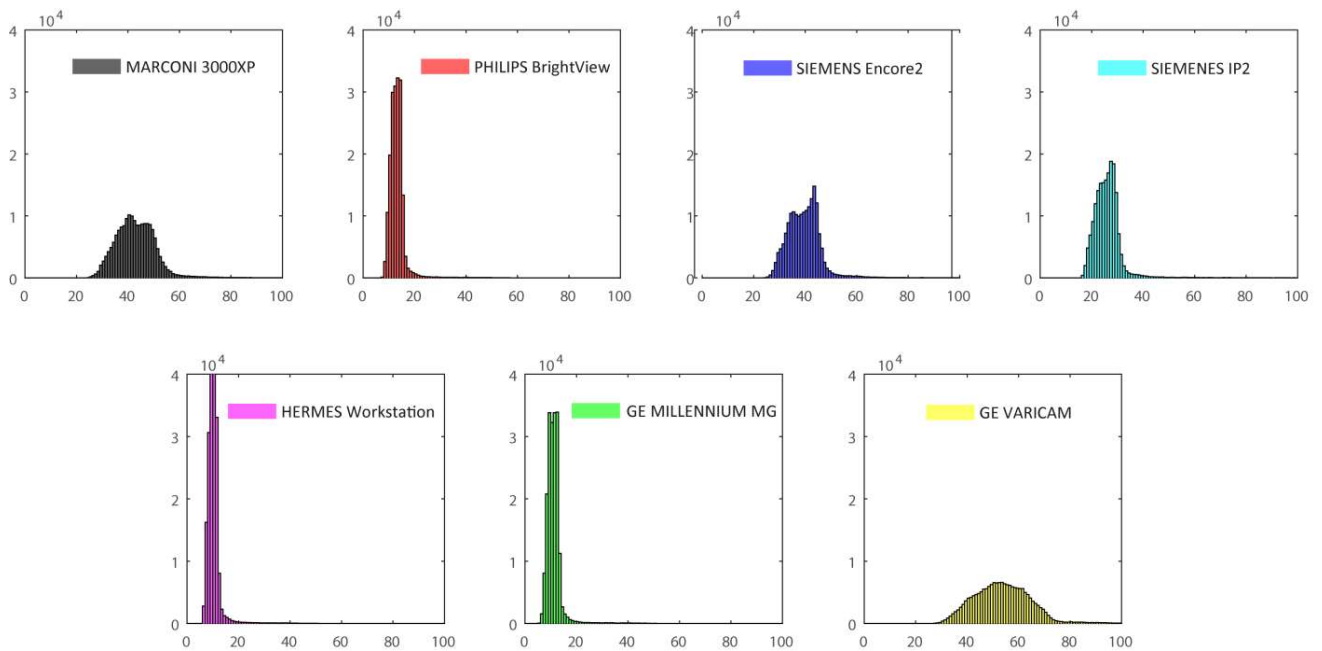

Figure 1. Intensity histogram of a DAT SPECT image from a normal control

Inter-scan variability

The intensity values of this type of images heavily depend on a variety of factors including both physiological-related such as age, sex and metabolism and device-related such as camera hardware and acquisition protocol. One of the largest source of variability is the imaging system (i.e., the camera), although images acquired with the same camera but with different acquisition parameters may give very different intensity profiles. Since in our dataset there are some sites with no or very few healthy controls to reliably model its intensity profile, we have grouped the images in our analyses by camera for both simplicity and sample size considerations. Figure 1 shows the mean histogram of the healthy controls for each camera, which illustrates the large variation in intensity profiles.

Beyond the camera, there are also other factors regarding acquisition set-up and parameters such as the collimators, the pixel size or the reconstruction algorithm that can influence this variability. Hence, the true intensity profile may be set-up specific rather than camera-specific. We have illustrated this concept in Figure 3, where the mean histogram of healthy controls acquired with SIEMENS Encore2 camera at 12 different sites (thus, 12 potential different set-ups) were plotted. It can be noted that there are at least three different profiles indicating that sites using the same camera produce different intensity profiles. In particular, the site 290 (turquoise) and the sites 12 (orange) and 73 (green) cluster separately from the other sites.

Figure 2. Mean histogram of the healthy controls DAT SPECT images of each camera
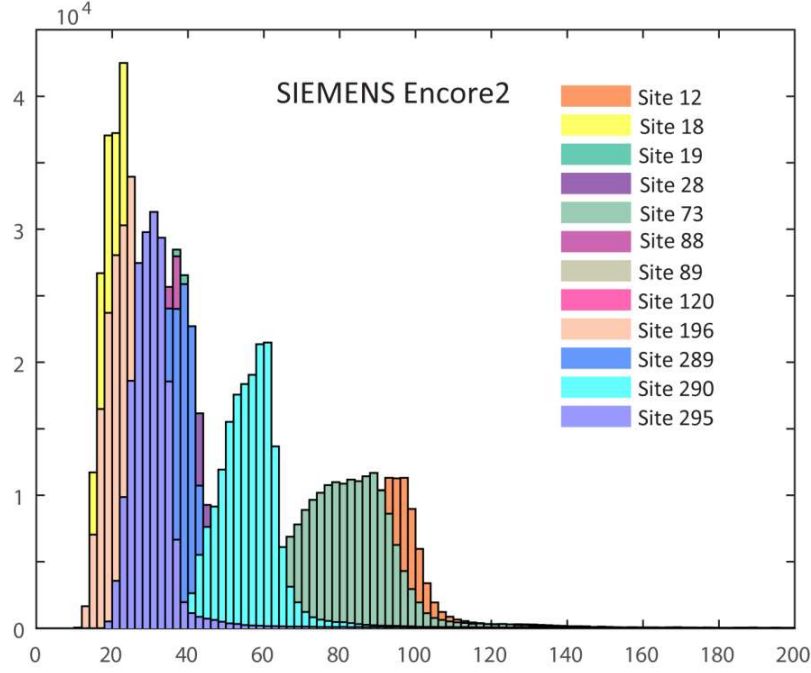
Figure 3. Mean histogram of the healthy controls DAT SPECT images of SIEMENS Encore2 camera acquired at 12 different sites.

Intensity normalization with Gamma mixture model

We propose to intensity normalize DAT SPECT images by a re-parametrization of the voxel values to the interval [0,1]. To this end, we propose to fit the image histogram to a mixture model of Gamma distributions. Each voxel value will be based on the cumulative density function (CDF) of the Gamma distribution function modeling the specific region of healthy subjects (i.e., the healthy striatum). In this way, each voxel intensity will represent the probability of activation, being 1 the highest value seen.

Formally, let $X = \{x_1, \dots, x_{S_1}, \dots, x_S\}$ represent neuroimaging vectors corresponding to DAT SPECT images from $S \in N$ subjects; from which the first S_1 subjects are healthy controls and the remaining have some pathology e.g. Parkinson's disease (PD). For each subject s, the vector $x_s = (x_1^s, \dots, x_n^s)$ represents the measurements at the $n \in V$ spatial locations in the brain (voxels). This methods consists of three main steps:

1. Subject-wise scaling with respect to the its mode $\bar{x}_j^s = \dfrac{x_j^s}{M_s}$ for $j \in \{1, \dots, n\}$ and $s \in \{1, \dots, S\}$, where M_s denotes the mode of the subject.

2. Learning the parameters of the Gamma mixture model using images from healthy subjects of a particular camera. We consider a mixture model of three Gamma components of the form:

$$p\,(x|\pi, \Theta) = \prod_{n=1}^{N} \sum_{k=1}^{3} \pi_k G_k(x_n \Theta_k)$$

where $\Theta_k = \{s_k, r_k\}$ are the shape and scale parameters of the three Gamma components and $\pi = \{\pi_1, \pi_2, \pi_3\}$ are the mixing proportions.

Thus, a DAT SPECT image histogram can be represented as the mixture of three Gamma distributions, two modeling the background (Figure 4 left) and one modeling the specific uptake (Figure 4 right). The model parameters were learnt using a Variational Bayesian approach. The model order (k=3) was estimated by evaluating the Free Energy of the models with different numbers of components.
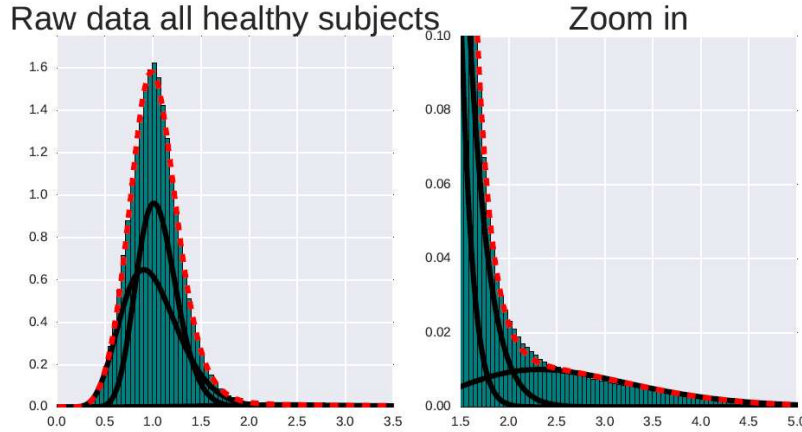
Figure 4. Mixture of three Gamma distributions to fit mean instensity histogram of DAT SPECT images from healthy subjects.

3. We compute the CDF of the Gamma distribution modeling the specfic region and substitute each voxel value by its value according to:

$$\bar{x}_j^s = \frac{1}{r_3^{s_3}\Gamma(s_3)} \int_0^{\bar{x}_j^s} t^{s_3-1} \exp\left(\frac{-t}{r_3}\right) dt, \ j \in \{1,\dots,n\}, s \in \{1,\dots,S\}$$

We will denote this re-parametrization as CDF-based intensity normalization (Figure 4). Importantly, this approach provides a great advantage with respect to other classical normalization approaches based on probability density functions: it keeps the probabilistic interpretation of the data while preserving a monotonic transformation, i.e. voxels near the mode have equal probablity of activation than voxels in the right tail.
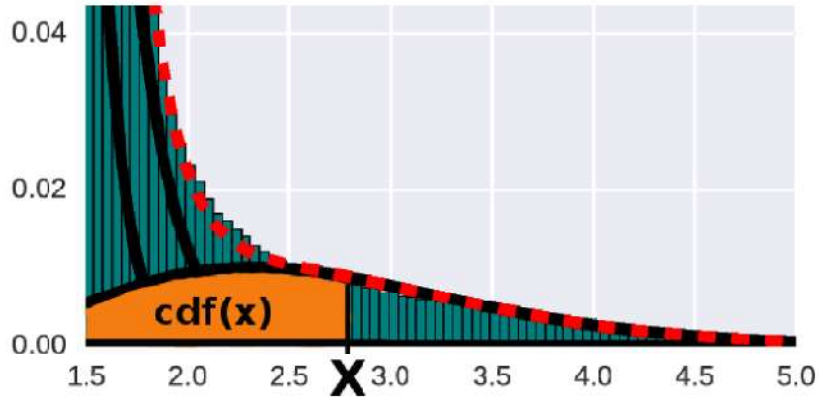
Figure 5. Cumulative Density Function (CDF) of the Gamma distribution modeling the specfic region. Each voxel value (x) will be replaced by its value under this distribution cdf (x).

Statistical analyses

In order to investigate the harmonization ability of our newly proposed method, we compared across cameras the intensity values of the primary subregions studied in DAT SPECT, namely putamen and caudate, before and after applying both the classical SBR and the Gamma CDF normalization. We made these comparisons only for healthy controls to avoid confounding the differences between cameras with the potential differences in PD severity. We used ANOVA and Tukey post-hoc analyses to identify differences between the imaging variables across cameras. The significance threshold was set to 0.007 (0.05/7) according to Bonferroni correction.

We also examined the performance of a simple classifier to distinguish between healthy controls and PD when using multi-center data. We run logistic regression using bilateral putamen and caudate variables for both SBR and Gamma CDF normalization, and the mean area under curve (AUC) after a 10-fold cross-validation schema was calculated. In addition, since striatal voxel values are normalized after CDF reparametrization, we also run logistic regression using all the voxels in the striatum to compare the performance between ROI- and voxel-based classification. To deal with the high dimensionality, we penalized the regression with L1 regularization.

Results

The Gamma CDF normalization schema provided a reparametrization of the intensity values of the DAT SPECT images to the interval [0, 1] for all cameras, and the corresponding intensity histograms were fairly equalized (Figure 6). An image example before and after normalization is shown in Figure 7. We observed that our normalization method produced a contrast enhancement of the image.
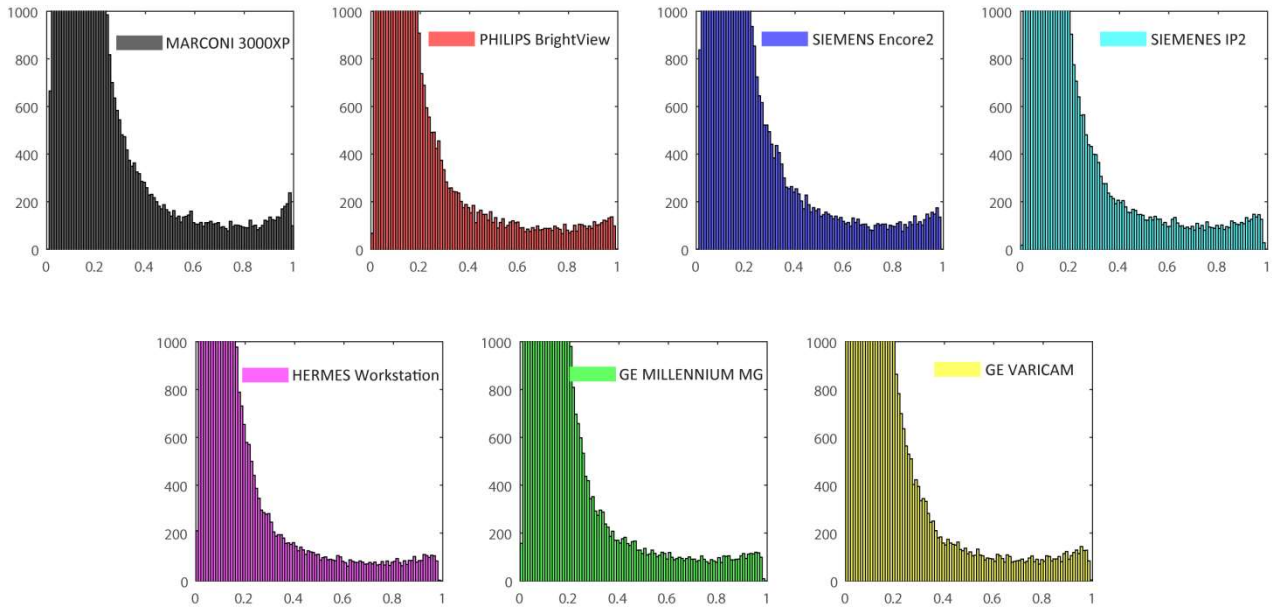
Figure 6. Mean histogram of the healthy controls DAT SPECT images of each camera after CDF-based normalization.
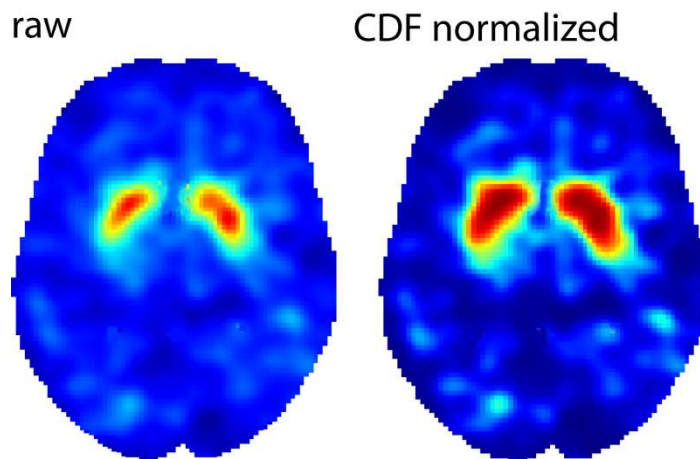
Figure 7. Example of the DAT SPECT image before (raw) and after normalization (CDF normalized).

Striatal intensity

The descriptive values for striatal intensity values (both raw and after normalization) across cameras are shown in Table 2. In healthy controls, we found significant differences in the mean striatal raw intensity values between many of the cameras. There were not differences in either sex and age indicating that these differences were not confounded by demographics. We observed that both SBR and CDF-based normalization schemas alleviated most of these differences although some differences remained. After SBR, differences remained between the camera MARCONI 3000XP and Encore2 and IP2 SIEMENS cameras (p<0.001). After CDF, differences remained between HERMES Workstation (Encore2 and IP2) and the cameras MARCONI 3000XP and SIEMENS Encore 2 (p<0.001).

Discrimination between healthy controls and PD

The results of the classifiers are summarized in Table 3. We observed that, when using SBR quantification, the performance of the classifiers was slightly poorer when scans from multiple sites/set-ups were pooled together. AUC values ranged from 0.83 to 0.93 being higher for classifiers contructed with images from a single site. Importantly, we found a significant improvement in performance when the ROI-based classifiers were built with striatal intensities after our proposed Gamma CDF normalization. For example, the AUC for IP2, HERMES and VARICAM classifiers remarkably increased by >10%. Moreover, since CDF normalization reparametrized the intensities at the voxel level to a unique interval [0, 1] for all scans, the classification performance was further enhanced to AUC = [0.95-1] by the use of voxel-based classiffiers.

Table 2. Demographics and mean caudate and putamen intensities for raw image, and after striatal binding ratio (SBR) and Gamma cumulative density function (CDF) normalization methods for healthy controls and PD patients.

		MARCONI	PHILIPS	SIEMENS		PICKER	GE	
		3000XP[1]	BrightView[2]	Encore2[3]	IP2[4]	HERMES[5]	MILLENNIUM[6]	VARICAM[7]
Controls	N	15	21	90	30	31	14	9
	raw caudate	$113 \pm 21^{2,4,5,6}$	$33 \pm 7^{1,3,7}$	$95 \pm 54^{2,4,5,6}$	$62 \pm 37^{1,3,7}$	$27 \pm 8^{1,3,7}$	$28 \pm 5^{1,3,7}$	$142 \pm 42^{2,4,5,6}$
	raw putamen	$101 \pm 18^{2,4,5,6}$	$29 \pm 6^{1,3,7}$	$87 \pm 49^{2,4,5,6}$	$56 \pm 35^{1,3,7}$	$24 \pm 7^{1,3,7}$	$25 \pm 4^{1,3,7}$	$130 \pm 38^{2,4,5,6}$
	SBR caudate	$2.37 \pm 0.51^{3,4}$	2.02 ± 0.47	1.78 ± 0.37^{1}	1.79 ± 0.33^{1}	2.20 ± 0.54	2.08 ± 0.49	2.20 ± 0.51
	SBR putamen	$1.99 \pm 0.41^{3,4}$	1.70 ± 0.36	1.53 ± 0.30^{1}	1.52 ± 0.27^{1}	1.80 ± 0.41	1.73 ± 0.32	1.94 ± 0.38
	CDF caudate	0.77 ± 0.04^{5}	0.72 ± 0.06	0.77 ± 0.06^{5}	0.74 ± 0.07	$0.71 \pm 0.07^{1,3}$	0.71 ± 0.07	0.72 ± 0.08
	CDF putamen	0.69 ± 0.04^{5}	0.62 ± 0.05	0.67 ± 0.06^{5}	0.64 ± 0.07	$0.60 \pm 0.06^{1,3}$	0.61 ± 0.05	0.65 ± 0.07
PD	N	179	133	494	128	108	61	29
	raw caudate	93 ± 23	29 ± 12	75 ± 43	58 ± 32	27 ± 11	22 ± 6	108 ± 31
	raw putamen	82 ± 20	26 ± 11	67 ± 38	51 ± 27	23 ± 9	19 ± 4	92 ± 25
	SBR caudate	1.43 ± 0.39	1.15 ± 0.48	1.19 ± 0.36	1.22 ± 0.35	1.42 ± 0.46	1.22 ± 0.51	1.61 ± 0.41
	SBR putamen	1.13 ± 0.30	0.93 ± 0.39	0.95 ± 0.29	0.96 ± 0.29	1.07 ± 0.36	0.94 ± 0.38	1.21 ± 0.27
	CDF caudate	0.61 ± 0.11	0.54 ± 0.14	0.60 ± 0.13	0.53 ± 0.13	0.49 ± 0.13	0.59 ± 0.13	0.57 ± 0.12
	CDF putamen	0.46 ± 0.09	0.40 ± 0.11	0.45 ± 0.10	0.38 ± 0.11	0.32 ± 0.10	0.43 ± 0.10	0.41 ± 0.08

Superscripts indicate post-hoc differences (p<0.007) between Gamma cameras

Table 3. Mean area under curve for controls vs PD classifiers using ROI striatal variables with SBR and CDF normalization and all striatal voxels with CDF normalization.

	ALL	MARCONI	PHILIPS	SIEMENS		PICKER	GE	
		3000XP	BrightView	Encore2	IP2	HERMES	MILLENNIUM	VARICAM
Sites (N)	24	1	3	14	6	4	1	2
AUC SBR (ROI)	0.86	0.93	0.88	0.86	0.87	0.83	0.90	0.87
AUC CDF (ROI)	0.89	0.90	0.95	0.89	0.95	0.93	0.90	0.98
AUC CDF (voxel)	0.98	1	0.99	0.98	0.97	0.95	0.96	1

Discussion

In this work we have introduced a probabilistic normalization schema valid for DAT SPECT images based on Bayesian mixture of Gamma distributions. We showed that the proposed methodology provides a reparameterization of the data in the interval [0,1] which effectively equalize the intensity histograms of the images procedent from different cameras and acquisition set-ups. Remarkably, our normalization step boosted up to >10% the discrimination ability between controls and PD when images from multiple sites/cameras were pooled together. Our method is also extensible to other modalities of functional imaging following the activation/background paradigm such as other SPECT radioligands or PET.

Data harmonization is a key element in the generation of reliable and reproducible results in science. In fact, recent years have seen an increase in alarming signals regarding the lack of replicability in neuroimaging research (Gorgolewski and Poldrack, 2016, Poldrack et al., 2017). There are many factors influencing this problem, some subject-related such as the variability in the collection of phenotypic data and the inherent heterogeneity in disease, but also the acquisition hardware and data analysis methods can play a major role. Unfortunately, this lack of standardization may generate site- or study-specific neuroimaging findings and estimates and therefore cause irreproducible and non-generalizable results.

We have observed this phenomenon in DAT SPECT data from PPMI repository, where the diagnostic classification performance between controls and PD varied from 83% to 93% when images from different sites were pooled and a suboptimal harmonization method such as the SBR was used. This variability suggests that the classification algorithms were biased (partly) due to the variability in intensity across sites/acquisition set-ups. We found that our normalization method was helpful to alleviate this bias and as a result the diagnostic performance of the same ROI-based algorithms improved to 89%-98%. Furthermore, in contrast to the classical SBR operating at the ROI level, our normalization method provided a reparametrization at the voxel level which allowed us to create voxel-based algorithms that further increased classification performance up to 95%-100%.

An additional benefit of our method with respect to the SBR and also other recently proposed voxel-based normalization methods is the reparametrization to a unique and universal interval [0, 1]. SBR values are commonly in the range [0,5-4] depending on the camera, and some previous studies have found significant differences in these values across sites, thus limitating the capacity of pooling them. Recently proposed voxel-based aproches (Salas-Gonzalez et al., 2013, Brahim et al., 2014, Brahim et al., 2015), while effective for harmonization, are still dependent on the intensities of the analyzed dataset and thus ROI intensities would require from an extra step to compare the obtained values with other datasets. We have seen that our method alleviates differences in striatal intensity across cameras (although not in a optimal way yet). In this way, mean ROI intensities (e.g., putamen and caudate) can be directly compared across studies and pooled for meta-analysis purposes. In our next work we will refine our method to further improve this homogeneization.

In summary, we have proposed an objective and automated intensity normalization method, based on a mixture model Gamma distributions that may constitute a key pre-processing step to analyze DAT SPECT images. In this work we have demonstrated that our method provides important advantages that are crucial for: i) pooling DAT SPECT images (especially multi-site) and ii) creating unbiased and generalizable neuroimaging-based machine learning algorithms with this type of images.

References

Badiavas K, Molyvda E, Iakovou I, Tsolaki M, Psarrakos K, Karatzas N (2011) SPECT imaging evaluation in movement disorders: far beyond visual assessment. European journal of nuclear medicine and molecular imaging 38:764-773.

Booij J, Teune LK, Verberne HJ (2012) The role of molecular imaging in the differential diagnosis of parkinsonism. The quarterly journal of nuclear medicine and molecular imaging : official publication of the Italian Association of Nuclear Medicine 56:17-26.

Brahim A, Gorriz JM, Ramirez J, Khedher L (2014) Linear intensity normalization of DaTSCAN images using Mean Square Error and a model-based clustering approach. Studies in health technology and informatics 207:251-260.

Brahim A, Ramirez J, Gorriz JM, Khedher L, Salas-Gonzalez D (2015) Comparison between Different Intensity Normalization Methods in 123I-Ioflupane Imaging for the Automatic Detection of Parkinsonism. PloS one 10:e0130274.

Djang DS, Janssen MJ, Bohnen N, Booij J, Henderson TA, Herholz K, Minoshima S, Rowe CC, Sabri O, Seibyl J, Van Berckel BN, Wanner M (2012) SNM practice guideline for dopamine transporter imaging with 123I-ioflupane SPECT 1.0. Journal of nuclear medicine : official publication, Society of Nuclear Medicine 53:154-163.

Gorgolewski KJ, Poldrack RA (2016) A Practical Guide for Improving Transparency and Reproducibility in Neuroimaging Research. PLoS biology 14:e1002506.

Poldrack RA, Baker CI, Durnez J, Gorgolewski KJ, Matthews PM, Munafo MR, Nichols TE, Poline JB, Vul E, Yarkoni T (2017) Scanning the horizon: towards transparent and reproducible neuroimaging research. Nature reviews Neuroscience 18:115-126.

Salas-Gonzalez D, Gorriz JM, Ramirez J, Illan IA, Lang EW (2013) Linear intensity normalization of FP-CIT SPECT brain images using the alpha-stable distribution. NeuroImage 65:449-455.

Tatsch K, Poepperl G (2013) Nigrostriatal dopamine terminal imaging with dopamine transporter SPECT: an update. Journal of nuclear medicine : official publication, Society of Nuclear Medicine 54:1331-1338.

Varrone A, Dickson JC, Tossici-Bolt L, Sera T, Asenbaum S, Booij J, Kapucu OL, Kluge A, Knudsen GM, Koulibaly PM, Nobili F, Pagani M, Sabri O, Vander Borght T, Van Laere K, Tatsch K (2013) European multicentre database of healthy controls for [123I]FP-CIT SPECT (ENC-DAT): age-related effects, gender differences and evaluation of different methods of analysis. European journal of nuclear medicine and molecular imaging 40:213-227.
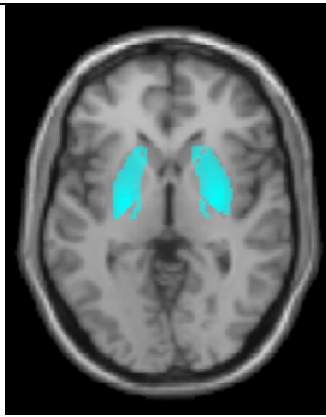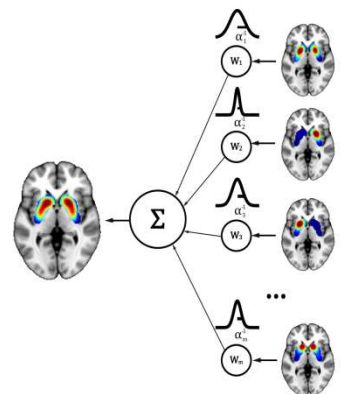
Discussion

Discussion

Globally, we have learnt and contributed with new results and concepts to field of clinical neuroimaging in movement disorders. We have tested some hypotheses of current debate in the literature such as the role of some genes in cognitive impairment, the role of uric acid in PD motor subtypes or the utility of the DAT SPECT to differentiate PD from other parkinsonisms. Also, we have developed new methods for image processing and pattern recognition in neuroimaging making use of cutting-edge concepts in this field of expertise. Some of these results are very relevant in my opinion and far beyond the state-of-the-art. The Table below shows the impressive evolution of the methods that I used to apply when I started to work with these images back in 2012 and how we evaluate these images now in 2017. This evolution is also seen in the pros and cons of each approach. We have passed from using the classical ROI-based calculation, which performs poorly and misses a lot of information due to the averaging; to using voxel-wise methods that are more accurate and richer in information but characterized by being prone to overfitting because the p>>N problem of dimensionality; to finally working with spatial models that are accurate and information-rich, work in low dimensions, and account for spatial correlation.

2012   2017

	ROI-based	**Voxel-wise**	**Spatial models**
Method	$SBR_{ROI} = \dfrac{C_{ROI} - C_{NSB}}{C_{NSB}}$	**Discriminative: SVM, LDA**	**Probabilistic: Bayesian optimization**
Information	Poor	Rich	Rich
Performance	Low	High	High
Parsimony	Yes	No	Yes
Dimensions / overfitting risk	Low	High	Low
Spatial correlation	No	No	Yes

Table. Evolution of the methodology to assess DATSCAN images during the thesis

In the following, I will summarize the discussions of the works presented, one by one:

Regarding **the role of uric acid in Parkinson's disease subtypes,** our data are in accordance with previous studies supporting this role. The largest studies exploring this relationship are PRECEPT and DATATOP (Schwarzschild et al., 2008, Ascherio et al., 2009), two longitudinal clinical trials conducted in the US that found that PD patients with lower levels of UA at baseline suffered from faster rates of clinical progression, including greater declines in the UPDRS total score and striatal DAT availability. Also, a recently published meta-analysis including 13,000 PD patients has provided a reliable effect size of this association (Wen et al., 2017). Given the fact that it is also known that PIGD PD patients have a worse disease course than TD PD patients, it was not surprising to see that UA levels differed between these subtypes. A recent study conducted in PD patients from Thailand showed that UA differed between PD subtypes (Lolekha et al., 2015). There is also some evidence, although weak, that UA levels correlate with striatal DAT (Spiegel et al., 2007, Schillaci et al., 2011).

Despite all this evidence, it still remains unclear how the course of UA is during the clinical progression. To the best of my knowledge, the majority of the conducted studies have cross-sectionally evaluated early and late stage patients, but any study has assessed longitudinally both UA and clinical state in the same group of patients. DATATOP for example tracked the clinical course with UPDRS but UA was not further tracked from baseline. In our study we evaluated UA and clinical state at late stages, but we also retrospectively verified the initial stages of these patients. We observed that 100% of TD had a tremor onset, but there was also a non-negligible proportion of patients that converted from a tremor-dominant onset to an intermediate phenotype (45% of I) or even to PIGD (25% of PIGD) during the course of the disease. Although unfortunately we did not count with UA in these initial stages, it would be very interesting to study whether these proportion of conversion from TD to PIGD are also aligned with drops in the levels of UA.

Regarding **the role of the studied genetic factors in cognitive impairment in PD**, we have provided new findings, and also both supported and contradicted some previous findings. In this line, notorious works have been performed, although there are conflicting results and the exact role of these risk genetic factors is unclear.

The CamPaING study longitudinally assessed 142 PD patients in the United Kingdom during 10 years, where they found MAPT H1 to be associated with dementia whereas no relationship was found for COMT Val158Met, SNCA rs356219 and APOE4 (Williams-Gray et al., 2013). On the other hand, the study by Mata et al. performed exhaustive neuropsychological assessments in 1079 PD patients from 6 academic centers in the United States and found a consistent association of APOE4 with cognitive impairment across several domains, whereas no role was found for MAPT H1 and SNCA rs356219 (Mata et al., 2014). The role of *GBA* seems to be clearer since several studies have consistently found that deleterious variants are associated with a worse disease progression including cognitive deficits and dementia (Winder-Rhodes et al., 2013, Mata et al., 2016). In particular for this gene, the debate is more focus on the role of some non-pathogenic variants and polymorphism.

Our long-term of dementia support the findings of Mata et al. role of APOE4 and GBA deleterious variants. Our assessment of striatal provides new insights about the role of these genetic factors. We hypothesized that a detrimental effect of certain genetic risk factors in striatal depletion could negatively influence the state of the frontrostriatal loop and therefore constitute a risk factor for dysexecutive syndrome. APOE2, SNCA rs356219, COMT Val158Met and GBA deleterious variants were found to be associated, which in line studies supporting the role of APOE2 and SNCA rs356219 in PD pathogenesis (Huang et al., 2004, Pihlstrom and Toft, 2011) and COMT Val158Met in dopamine metabolism (Wu et al., 2012).

Regarding **the diagnosis of vascular parkinsonism,** the study herein presented, along with our previous study on VP (Benitez-Rivero et al., 2013) and a similar multicentre study performed in Italy (Antonini et al., 2012), have confirmed what it has been postulated for years: VP is a different and distinguishable entity from PD; however clinical manifestations and imaging patterns are very heterogeneous, which make the diagnosis very challenging.

The heterogeneity in VP there included a high proportion of normal scans (up to 37% has been reported) (Antonini et al., 2012), the location of striatal dopamine deficit may depend on the cerebrovascular lesion, which can vary from patient to patient, and also a non-neglibile percent (16%) with a very similar imaging pattern than PD (Benitez-Rivero et al., 2013). ROI-based comparisons between VP and PD have found lower striatal DAT and higher asymmetry indices in PD, but these group-level differences are not sufficient to establish a specific diagnosis at the single subject level (Contrafatto et al., 2012). Our study attempted to make this pattern recognition of VP profile in DAT imaging more automated, and indeed it is the first study in the literature using both ROI and voxel data to discriminate the two entities using machine learning algorithms. Although the results are very good for this binary comparison (90% accuracy, which might be even higher due few possible clinical mislabelling a PD as VP in early stages)

Nevertheless, it should be noted that this diagnostic specificity for VP may be poor in a multi-class classifier with other unknown movement disorders. For example, if >30% of VP scans are visually classified as normal the differential diagnosis with essential tremor may be inaccurate. In this regard, spatial modelling from work 4) constitutes a promising approach to deal with these complex patterns and spatial heterogeneity. This approach has the potential to identify subtle spatial patterns disregarded by the human eye. In future work, it would be very interesting to test whether these models are able to model the spatial heterogeneity and what is even more challenging, to notice differences between normal scans in essential tremor and VP.

Regarding **the use of spatial models for neuroimaging,** we have provided a new framework to analyze brain images that potentially address many of the problems that convey the use of the voxel. In this regard, although the use of the voxel has provided great advances in our understanding of the brain in health and disease during already two decades, criticism due to three major reasons: i) the voxel is a mere resolution unit without biological meaning and ii) voxel-wise approaches generate a massive amount of statistical estimates that which may reduce power to

detect signals; and iii) brain regions interact with other non-spatially-contiguous regions and these interactions are disregarded with univariate approaches.

There have been recent efforts to overcome these limitations, including multivariate approaches such as multivariate pattern analysis (MVPA), which eludes the assumption of independence between voxels, and other similar spatial models such as Topographic Latent Source Analysis (TLSA) which is constructed with radial basis functions (Gershman et al., 2011). A main difference between our work and TLSA is the nature if the basis functions, being generic in TLSA whereas our work introduces a new family of basis functions extracted from brain function. Our framework provides an elegant alternative to classical mass-univariate and approaches using generic basis functions including the following advantages: (i) a gain in biological interpretability; (ii) the ability to utilise information from multiple data modalities; (iii) a great reduction of the number of statistical tests; (iv) incorporation of multi-resolutional spatial information in the image; and (v) a method to automatically identify meaningful subregions/subnetworks. Our approach is generic and it is also possible to employ many other types of basis set such as, fine-grained parcels obtained from ultra-high resolution MRI (Keuken et al., 2014) or multi-modal parcellations (Glasser et al., 2016). Although a possible disadvantage of other methods with respect to ICP family basis set, is that if parcellations are not defined at different levels of granurality, the spatial dependencies across multiple scales may not be properly captured.

The weights associated with the basis functions, which implicitly encode spatial information, can be used in further analyses to compare groups or investigate quantitative measures with parametric statistics or machine learning techniques. Hence, these spatial-wise weights can have diagnostic utility and provide new insights into disease mechanisms. For example in DAT imaging in PD, loss in mean putamen uptake is known to be associated with motor symptoms in general. It would be interesting if future work to use our model to find subnetworks associated with more specific symptoms, such as rigidity, gait disorder or dyskinesias.

Lastly, regarding **the intensity normalization of DAT SPECT images,** we provide an effective method to harmonize intensity across cameras. There are two major limitations of the current standard to normalize and quantify these images, namely the striatal binding ratio (SBR): i) it is ROI-based, and therefore voxel-based approaches cannot applied with these normalization schema; and ii) it makes assumptions about the intensity distribution of the image that are not fully true, and indeed previous studies have shown that different Gamma cameras can produce different striatal SBR (Varrone et al., 2013). Thus, these factors limitate the capacity to: i) compare studies or pool images from different sites; and ii) to create voxel-based algorithms with these images. As a consequence, this lack of standardization may have generated site- or study-specific neuroimaging findings and estimates that might unfortunately be irreproducible and non-generalizable.

We have observed this phenomenon in DAT SPECT data from PPMI repository, where the diagnostic classification performance between controls and PD varied from 83% to 93% when images from different sites were pooled and a suboptimal harmonization method such as the SBR was used. We found that our normalization method was helpful to alleviate this bias and as a result the diagnostic performance of the same ROI-based algorithms improved to 89%-98%. Furthermore,

in contrast to the classical SBR operating at the ROI level, our normalization method provided a reparametrization at the voxel level which allowed us to create voxel-based algorithms that further increased classification performance up to 95%-100%.

An additional benefit of our method is the reparametrization to a unique and universal interval [0, 1]. SBR values are commonly in the range [0,5-4] depending on the camera, and the absolute values of recently proposed voxel-based aproches (Salas-Gonzalez et al., 2013, Brahim et al., 2014, Brahim et al., 2015), while effective for harmonization, are still dependent on the intensities of the analyzed dataset. By reparametrizating the image to an harmonized interval [0,1], mean ROI intensities (e.g., putamen and caudate) will be always comparable across studies and could be pooled for meta-analyses.

Conclusions

Conclusions

1. Parkinson's disease patients who present with a tremor onset and maintain predominance of tremor, or, to a lesser extent, an intermediate phenotype, have higher levels of uric acid and striatal DAT binding than those who develop postural instability and gait disorder phenotype. Low levels of this natural antioxidant may lead to a lesser degree of neuroprotection and could therefore influence motor phenotype and the clinical course

2. *APOE2* allele, and the polymorphisms *SNCA rs356219* and *COMT Val158Met* influence striatal dopaminergic depletion; *APOE4* allele influences dementia and deleterious variants in *GBA* influence both. The dichotomy of the dual syndromes may be driven by a broad dichotomy in these genetic factors

3. The imaging of DAT with SPECT is a useful tool for discriminating vascular parkinsonism from Parkinson's disease. The use of machine learning algorithms using either the regional striatal quantification or the voxel-wise data of the striatum gives high discrimination accuracy. Hence, objective and automated algorithms can be deployed to aid the differential diagnosis of these two parkinsonisms

4. The use of multivariate spatial models using a linear superposition of basis functions constitutes an elegant and efficient method to analyze brain images. The model is flexible and can be adapted to test different families of basis functions. The coefficients associated with the basis functions can be utilized to create accurate classification and regression models with clinical application.

5. Multi-resolutional parcellations of brain regions, such as the ones generated with the instantaneous correlation parcellation (ICP) method, are an effective family of basis functions to build spatial models. These models offers unpredecent benefits with respect to classical mass-univariate voxel methods, including: biological interpretability, computational efficience, and multi-range spatial correlation modeling.

6. The proposed Bayesian analysis framework for neuroimaging analysis - with automatic relevance determination of features and posterior distribution optimization - allows to automatically identifying meaningful brain subregions/subnetworks for phenotypic outcomes and properly quantifying the uncertainty over the predictions.

7. The intensity histogram of a DAT SPECT image can be efficiently modeled as a mixture model of Gamma distributions. The parameters shaping the Gamma distributions can be used to harmonize the image intensity at the voxel level even when the scans were acquired with different Gamma cameras.

8. The cumulative density function of the Gamma distribution modeling the specific uptake can be used to re-cast the voxel intensity into a new – and universal – normalized feature space between 0 and 1. The proposed reparameterization drastically improves the accuracy of PD diagnosis when images from different cameras are pooled. Therefore, this harmonization method may constitute a key pre-processing step for multi-center studies and studies aiming at developing generalizable clinical applications

Conclusiones

1. Los pacientes de enfermedad de Parkinson que debutan con temblor y mantienen un predominio del temblor en el transcurso de la enfermedad, tienen mayores niveles de ácido úrico y dopamina estriatal que aquellos que desarrollan un fenotipo motor con predominio del trastorno de la marcha y la inestabilidad postural. Niveles bajos de este antioxidante natural pueden disminuir los niveles de neuroprotección y por tanto influenciar el fenotipo motor y el curso clínico.

2. *El alelo APOE2*, y los polimorfismos *SNCA rs356219* y *COMT Val158Met* se asocian con degeneración dopaminergica estriatal; el alelo *APOE4* se asocia con el desarrollo de demencia; y las variantes deletereas en *GBA* se asocian con ambos procesos. La dicotomía de los síndromes duales puede estar conducida por una dicotomía en dichos factores genéticos.

3. El SPECT con [^{123}I]FP-CIT es una herramienta útil para diferenciar el parkinsonismo vascular de la enfermedad de Parkinson. El uso de algoritmos de aprendizaje automático ya sea con variables de captación estriatal o con información estriatal a nivel de voxel, permiten crear modelos con gran exactitud diagnóstica. Por tanto, dicho diagnóstico diferencial podría ser asistido con algoritmos objetivos y automáticos.

4. El uso de modelos multivariados espaciales usando superposición lineal de funciones base constituye una aproximación eficiente y elegante para el análisis de neuroimagen. El modelo es flexible y puede ser adaptado para probar distintas familias de funciones base. Los coeficientes asociados a las funciones base se pueden utilizar para crear modelos de classificación y regresión con aplicación clínica.

5. Las parcelaciones multiescala de regiones cerebrales, tales como aquellas generadas por el método de parcelación por correlaciones instantáneas (ICP), son una familia de funciones base efectivapara el desarrollo de modelos espaciales. Esgtos modelos ofrecen ventajes sin precedentes con respecto el método clásico univeado basado en vóxel, incluyendo: interpretabilidad biológica, eficiencia computacional y modelado de la correlacion espacial a múltiples niveles de granularidad.

6. El método Bayesiano propuesto para el análisis de neuroimagen – usando determinación automática de variables relevantes y optimización de la distribución a posteriori – permite identificar automáticamente las regiones y/o redes cerebrales que se asocian con variables fenotípicas a la vez que cuantificar la incertidumbre de las predicciones.

7. El histograma de intensidad del SPECT con [^{123}I]FP-CIT puede ser modelado de manera eficiente con on modelo mixto de distribuciones Gamma. Los parámetros que dan forma a dichas distribuciones Gamma pueden ser utilizados para armonizar la intensidad de la imagen a nivel de vóxel incluso cuando las imágenes han sido adquiridas con cámaras Gamma distintas.

8. La función de densidad acumulada de la distribución Gamma que modela la región específica puede ser usada para reparametrizar la intensidad de voxel a un nuevo espacio normalizado – y universal – entre 0 y 1. Dicha reparametrización mejora de manera drástica el diagnóstico de enfermedad de Parkinson cuando se crean clasificadores con imágenes de distintas cámaras Gamma. Por tanto, la normalización propuesta puede constituir un paso de pre-procesado clave en estudios multicéntricos y en el desarrollo de aplicaciones clínicas reproducibles.

References

Aarsland D, Bronnick K, Fladby T (2011) Mild cognitive impairment in Parkinson's disease. Current neurology and neuroscience reports 11:371-378.

Alcalay RN, Levy OA, Waters CC, Fahn S, Ford B, Kuo SH, Mazzoni P, Pauciulo MW, Nichols WC, Gan-Or Z, Rouleau GA, Chung WK, Wolf P, Oliva P, Keutzer J, Marder K, Zhang X (2015) Glucocerebrosidase activity in Parkinson's disease with and without GBA mutations. Brain : a journal of neurology 138:2648-2658.

Antonini A, Vitale C, Barone P, Cilia R, Righini A, Bonuccelli U, Abbruzzese G, Ramat S, Petrone A, Quatrale R, Marconi R, Ceravolo R, Stefani A, Lopiano L, Zappia M, Capus L, Morgante L, Tamma F, Tinazzi M, Colosimo C, Guerra UP (2012) The relationship between cerebral vascular disease and parkinsonism: The VADO study. Parkinsonism & related disorders 18:775-780.

Ascherio A, LeWitt PA, Xu K, Eberly S, Watts A, Matson WR, Marras C, Kieburtz K, Rudolph A, Bogdanov MB, Schwid SR, Tennis M, Tanner CM, Beal MF, Lang AE, Oakes D, Fahn S, Shoulson I, Schwarzschild MA, Parkinson Study Group DI (2009) Urate as a predictor of the rate of clinical decline in Parkinson disease. Archives of neurology 66:1460-1468.

Badiavas K, Molyvda E, Iakovou I, Tsolaki M, Psarrakos K, Karatzas N (2011) SPECT imaging evaluation in movement disorders: far beyond visual assessment. European journal of nuclear medicine and molecular imaging 38:764-773.

Beckmann CF, Smith SM (2004) Probabilistic independent component analysis for functional magnetic resonance imaging. IEEE transactions on medical imaging 23:137-152.

Benamer TS, Patterson J, Grosset DG, Booij J, de Bruin K, van Royen E, Speelman JD, Horstink MH, Sips HJ, Dierckx RA, Versijpt J, Decoo D, Van Der Linden C, Hadley DM, Doder M, Lees AJ, Costa DC, Gacinovic S, Oertel WH, Pogarell O, Hoeffken H, Joseph K, Tatsch K, Schwarz J, Ries V (2000) Accurate differentiation of parkinsonism and essential tremor using visual assessment of [123I]-FP-CIT SPECT imaging: the [123I]-FP-CIT study group. Movement disorders : official journal of the Movement Disorder Society 15:503-510.

Benitez-Rivero S, Marin-Oyaga VA, Garcia-Solis D, Huertas-Fernandez I, Garcia-Gomez FJ, Jesus S, Caceres MT, Carrillo F, Ortiz AM, Carballo M, Mir P (2013) Clinical features and 123I-FP-CIT SPECT imaging in vascular parkinsonism and Parkinson's disease. Journal of neurology, neurosurgery, and psychiatry 84:122-129.

Booij J, Teune LK, Verberne HJ (2012) The role of molecular imaging in the differential diagnosis of parkinsonism. The quarterly journal of nuclear medicine and molecular imaging : official publication of the Italian Association of Nuclear Medicine 56:17-26.

Brahim A, Gorriz JM, Ramirez J, Khedher L (2014) Linear intensity normalization of DaTSCAN images using Mean Square Error and a model-based clustering approach. Studies in health technology and informatics 207:251-260.

Brahim A, Ramirez J, Gorriz JM, Khedher L, Salas-Gonzalez D (2015) Comparison between Different Intensity Normalization Methods in 123I-Ioflupane Imaging for the Automatic Detection of Parkinsonism. PloS one 10:e0130274.

Brockmann K, Srulijes K, Pflederer S, Hauser AK, Schulte C, Maetzler W, Gasser T, Berg D (2015) GBA-associated Parkinson's disease: reduced survival and more rapid progression in a prospective longitudinal study. Movement disorders : official journal of the Movement Disorder Society 30:407-411.

Brooks DJ, Piccini P (2006) Imaging in Parkinson's disease: the role of monoamines in behavior. Biological psychiatry 59:908-918.

Colloby SJ, O'Brien JT, Fenwick JD, Firbank MJ, Burn DJ, McKeith IG, Williams ED (2004) The application of statistical parametric mapping to 123I-FP-CIT SPECT in dementia with Lewy bodies, Alzheimer's disease and Parkinson's disease. NeuroImage 23:956-966.

Contrafatto D, Mostile G, Nicoletti A, Dibilio V, Raciti L, Lanzafame S, Luca A, Distefano A, Zappia M (2012) [(123) I]FP-CIT-SPECT asymmetry index to differentiate Parkinson's disease from vascular parkinsonism. Acta neurologica Scandinavica 126:12-16.

Cressie N, Johannesson G (2008) Fixed rank kriging for very large spatial data sets. Journal of the Royal Statistical Society Series B: Statistical Methodology 70:209-226.

Chen X, Burdett TC, Desjardins CA, Logan R, Cipriani S, Xu Y, Schwarzschild MA (2013) Disrupted and transgenic urate oxidase alter urate and dopaminergic neurodegeneration. Proceedings of the National Academy of Sciences of the United States of America 110:300-305.

Chen X, Wu G, Schwarzschild MA (2012) Urate in Parkinson's disease: more than a biomarker? Current neurology and neuroscience reports 12:367-375.

de la Fuente-Fernandez R (2013) Imaging of Dopamine in PD and Implications for Motor and Neuropsychiatric Manifestations of PD. Frontiers in neurology 4:90.

Djang DS, Janssen MJ, Bohnen N, Booij J, Henderson TA, Herholz K, Minoshima S, Rowe CC, Sabri O, Seibyl J, Van Berckel BN, Wanner M (2012) SNM practice guideline for dopamine transporter imaging with 123I-ioflupane SPECT 1.0. Journal of nuclear medicine : official publication, Society of Nuclear Medicine 53:154-163.

Dorsey ER, Constantinescu R, Thompson JP, Biglan KM, Holloway RG, Kieburtz K, Marshall FJ, Ravina BM, Schifitto G, Siderowf A, Tanner CM (2007) Projected number of people with Parkinson disease in the most populous nations, 2005 through 2030. Neurology 68:384-386.

Eggers C, Pedrosa DJ, Kahraman D, Maier F, Lewis CJ, Fink GR, Schmidt M, Timmermann L (2012) Parkinson subtypes progress differently in clinical course and imaging pattern. PloS one 7:e46813.

Eklund A, Nichols TE, Knutsson H (2016) Cluster failure: Why fMRI inferences for spatial extent have inflated false-positive rates. Proceedings of the National Academy of Sciences of the United States of America 113:7900-7905.

Emre M, Aarsland D, Brown R, Burn DJ, Duyckaerts C, Mizuno Y, Broe GA, Cummings J, Dickson DW, Gauthier S, Goldman J, Goetz C, Korczyn A, Lees A, Levy R, Litvan I, McKeith I, Olanow W, Poewe W, Quinn N, Sampaio C, Tolosa E, Dubois B (2007) Clinical diagnostic criteria for dementia associated with Parkinson's disease. Movement disorders : official journal of the Movement Disorder Society 22:1689-1707; quiz 1837.

Erro R, Pappata S, Amboni M, Vicidomini C, Longo K, Santangelo G, Picillo M, Vitale C, Moccia M, Giordano F, Brunetti A, Pellecchia MT, Salvatore M, Barone P (2012) Anxiety is associated

with striatal dopamine transporter availability in newly diagnosed untreated Parkinson's disease patients. Parkinsonism & related disorders 18:1034-1038.

Ezquerra M, Campdelacreu J, Gaig C, Compta Y, Munoz E, Marti MJ, Valldeoriola F, Tolosa E (2008) Lack of association of APOE and tau polymorphisms with dementia in Parkinson's disease. Neuroscience letters 448:20-23.

Federoff M, Jimenez-Rolando B, Nalls MA, Singleton AB (2012) A large study reveals no association between APOE and Parkinson's disease. Neurobiology of disease 46:389-392.

FitzGerald PM, Jankovic J (1989) Lower body parkinsonism: evidence for vascular etiology. Movement disorders : official journal of the Movement Disorder Society 4:249-260.

Foltynie T, Brayne C, Barker RA (2002) The heterogeneity of idiopathic Parkinson's disease. Journal of neurology 249:138-145.

Garcia-Gomez FJ, Garcia-Solis D, Luis-Simon FJ, Marin-Oyaga VA, Carrillo F, Mir P, Vazquez-Albertino RJ (2013) [Elaboration of the SPM template for the standardization of SPECT images with 123I-Ioflupane]. Revista espanola de medicina nuclear e imagen molecular 32:350-356.

Gegg ME, Burke D, Heales SJ, Cooper JM, Hardy J, Wood NW, Schapira AH (2012) Glucocerebrosidase deficiency in substantia nigra of parkinson disease brains. Annals of neurology 72:455-463.

Gerschlager W, Bencsits G, Pirker W, Bloem BR, Asenbaum S, Prayer D, Zijlmans JC, Hoffmann M, Brucke T (2002) [123I]beta-CIT SPECT distinguishes vascular parkinsonism from Parkinson's disease. Movement disorders : official journal of the Movement Disorder Society 17:518-523.

Gershman SJ, Blei DM, Pereira F, Norman KA (2011) A topographic latent source model for fMRI data. NeuroImage 57:89-100.

Glasser MF, Coalson TS, Robinson EC, Hacker CD, Harwell J, Yacoub E, Ugurbil K, Andersson J, Beckmann CF, Jenkinson M, Smith SM, Van Essen DC (2016) A multi-modal parcellation of human cerebral cortex. Nature 536:171-178.

Goebel G, Seppi K, Donnemiller E, Warwitz B, Wenning GK, Virgolini I, Poewe W, Scherfler C (2011) A novel computer-assisted image analysis of [123I]beta-CIT SPECT images improves the diagnostic accuracy of parkinsonian disorders. European journal of nuclear medicine and molecular imaging 38:702-710.

Goker-Alpan O, Masdeu JC, Kohn PD, Ianni A, Lopez G, Groden C, Chapman MC, Cropp B, Eisenberg DP, Maniwang ED, Davis J, Wiggs E, Sidransky E, Berman KF (2012) The neurobiology of glucocerebrosidase-associated parkinsonism: a positron emission tomography study of dopamine synthesis and regional cerebral blood flow. Brain : a journal of neurology 135:2440-2448.

Gorgolewski KJ, Poldrack RA (2016) A Practical Guide for Improving Transparency and Reproducibility in Neuroimaging Research. PLoS biology 14:e1002506.

Goris A, Williams-Gray CH, Clark GR, Foltynie T, Lewis SJ, Brown J, Ban M, Spillantini MG, Compston A, Burn DJ, Chinnery PF, Barker RA, Sawcer SJ (2007) Tau and alpha-synuclein in susceptibility to, and dementia in, Parkinson's disease. Annals of neurology 62:145-153.

Hastie TJ, Tibshirani RJ, Friedman JH (2013) The elements of statistical learning : data mining,

inference, and prediction. New York: Springer.

Helmich RC, Hallett M, Deuschl G, Toni I, Bloem BR (2012) Cerebral causes and consequences of parkinsonian resting tremor: a tale of two circuits? Brain : a journal of neurology 135:3206-3226.

Hershey LA, Feldman BJ, Kim KY, Commichau C, Lichter DG (1991) Tremor at onset. Predictor of cognitive and motor outcome in Parkinson's disease? Archives of neurology 48:1049-1051.

Huang X, Chen PC, Poole C (2004) APOE-[epsilon]2 allele associated with higher prevalence of sporadic Parkinson disease. Neurology 62:2198-2202.

Huertas-Fernandez I, Garcia-Gomez FJ, Garcia-Solis D, Benitez-Rivero S, Marin-Oyaga VA, Jesus S, Caceres-Redondo MT, Lojo JA, Martin-Rodriguez JF, Carrillo F, Mir P (2015) Machine learning models for the differential diagnosis of vascular parkinsonism and Parkinson's disease using [(123)I]FP-CIT SPECT. European journal of nuclear medicine and molecular imaging 42:112-119.

Hughes AJ, Daniel SE, Ben-Shlomo Y, Lees AJ (2002) The accuracy of diagnosis of parkinsonian syndromes in a specialist movement disorder service. Brain : a journal of neurology 125:861-870.

Hughes AJ, Daniel SE, Kilford L, Lees AJ (1992) Accuracy of clinical diagnosis of idiopathic Parkinson's disease: a clinico-pathological study of 100 cases. Journal of neurology, neurosurgery, and psychiatry 55:181-184.

Jankovic J, McDermott M, Carter J, Gauthier S, Goetz C, Golbe L, Huber S, Koller W, Olanow C, Shoulson I, et al. (1990) Variable expression of Parkinson's disease: a base-line analysis of the DATATOP cohort. The Parkinson Study Group. Neurology 40:1529-1534.

Jellinger KA (2003) Prevalence of cerebrovascular lesions in Parkinson's disease. A postmortem study. Acta neuropathologica 105:415-419.

Jesus S, Huertas I, Bernal-Bernal I, Bonilla-Toribio M, Caceres-Redondo MT, Vargas-Gonzalez L, Gomez-Llamas M, Carrillo F, Calderon E, Carballo M, Gomez-Garre P, Mir P (2016) GBA Variants Influence Motor and Non-Motor Features of Parkinson's Disease. PloS one 11:e0167749.

Jesus S, Perez I, Caceres-Redondo MT, Carrillo F, Carballo M, Gomez-Garre P, Mir P (2013) Low serum uric acid concentration in Parkinson's disease in southern Spain. European journal of neurology 20:208-210.

Kaasinen V, Kinos M, Joutsa J, Seppanen M, Noponen T (2014) Differences in striatal dopamine transporter density between tremor dominant and non-tremor Parkinson's disease. European journal of nuclear medicine and molecular imaging 41:1931-1937.

Kalia LV, Lang AE (2015) Parkinson's disease. The Lancet 386:896-912.

Kalra S, Grosset DG, Benamer HT (2010) Differentiating vascular parkinsonism from idiopathic Parkinson's disease: a systematic review. Movement disorders : official journal of the Movement Disorder Society 25:149-156.

Kehagia AA, Barker RA, Robbins TW (2013) Cognitive impairment in Parkinson's disease: the dual syndrome hypothesis. Neuro-degenerative diseases 11:79-92.

Keuken MC, Bazin PL, Crown L, Hootsmans J, Laufer A, Muller-Axt C, Sier R, van der Putten EJ,

Schafer A, Turner R, Forstmann BU (2014) Quantifying inter-individual anatomical variability in the subcortex using 7 T structural MRI. NeuroImage 94:40-46.

Kiferle L, Ceravolo R, Giuntini M, Linsalata G, Puccini G, Volterrani D, Bonuccelli U (2014) Caudate dopaminergic denervation and visual hallucinations: evidence from a (1)(2)(3)I-FP-CIT SPECT study. Parkinsonism & related disorders 20:761-765.

Lewis SJ, Foltynie T, Blackwell AD, Robbins TW, Owen AM, Barker RA (2005) Heterogeneity of Parkinson's disease in the early clinical stages using a data driven approach. Journal of neurology, neurosurgery, and psychiatry 76:343-348.

Lolekha P, Wongwan P, Kulkantrakorn K (2015) Association between serum uric acid and motor subtypes of Parkinson's disease. Journal of clinical neuroscience : official journal of the Neurosurgical Society of Australasia 22:1264-1267.

Lorberboym M, Djaldetti R, Melamed E, Sadeh M, Lampl Y (2004) 123I-FP-CIT SPECT imaging of dopamine transporters in patients with cerebrovascular disease and clinical diagnosis of vascular parkinsonism. Journal of nuclear medicine : official publication, Society of Nuclear Medicine 45:1688-1693.

Mata IF, Leverenz JB, Weintraub D, Trojanowski JQ, Chen-Plotkin A, Van Deerlin VM, Ritz B, Rausch R, Factor SA, Wood-Siverio C, Quinn JF, Chung KA, Peterson-Hiller AL, Goldman JG, Stebbins GT, Bernard B, Espay AJ, Revilla FJ, Devoto J, Rosenthal LS, Dawson TM, Albert MS, Tsuang D, Huston H, Yearout D, Hu SC, Cholerton BA, Montine TJ, Edwards KL, Zabetian CP (2016) GBA Variants are associated with a distinct pattern of cognitive deficits in Parkinson's disease. Movement disorders : official journal of the Movement Disorder Society 31:95-102.

Mata IF, Leverenz JB, Weintraub D, Trojanowski JQ, Hurtig HI, Van Deerlin VM, Ritz B, Rausch R, Rhodes SL, Factor SA, Wood-Siverio C, Quinn JF, Chung KA, Peterson AL, Espay AJ, Revilla FJ, Devoto J, Hu SC, Cholerton BA, Wan JY, Montine TJ, Edwards KL, Zabetian CP (2014) APOE, MAPT, and SNCA genes and cognitive performance in Parkinson disease. JAMA neurology 71:1405-1412.

McNeill A, Wu RM, Tzen KY, Aguiar PC, Arbelo JM, Barone P, Bhatia K, Barsottini O, Bonifati V, Bostantjopoulou S, Bressan R, Cossu G, Cortelli P, Felicio A, Ferraz HB, Herrera J, Houlden H, Hoexter M, Isla C, Lees A, Lorenzo-Betancor O, Mencacci NE, Pastor P, Pappata S, Pellecchia MT, Silveria-Moriyama L, Varrone A, Foltynie T, Schapira AH (2013) Dopaminergic neuronal imaging in genetic Parkinson's disease: insights into pathogenesis. PloS one 8:e69190.

Moccia M, Pappata S, Erro R, Picillo M, Vitale C, Amboni M, Longo K, Palladino R, Barone P, Pellecchia MT (2015) Uric acid relates to dopamine transporter availability in Parkinson's disease. Acta neurologica Scandinavica 131:127-131.

Mollenhauer B, Rochester L, Chen-Plotkin A, Brooks D (2014) What can biomarkers tell us about cognition in Parkinson's disease? Movement disorders : official journal of the Movement Disorder Society 29:622-633.

Muellner J, Gharrad I, Habert MO, Kas A, Martini JB, Cormier-Dequaire F, Tahiri K, Vidailhet M, Meier N, Brice A, Schuepbach M, Mallet A, Hartmann A, Corvol JC (2015) Dopaminergic denervation severity depends on COMT Val158Met polymorphism in Parkinson's disease. Parkinsonism & related disorders 21:471-476.

Navarro-Otano J, Gaig C, Muxi A, Lomena F, Compta Y, Buongiorno MT, Marti MJ, Tolosa E, Valldeoriola F (2014) 123I-MIBG cardiac uptake, smell identification and 123I-FP-CIT SPECT in the differential diagnosis between vascular parkinsonism and Parkinson's disease. Parkinsonism & related disorders 20:192-197.

Neumann J, Bras J, Deas E, O'Sullivan SS, Parkkinen L, Lachmann RH, Li A, Holton J, Guerreiro R, Paudel R, Segarane B, Singleton A, Lees A, Hardy J, Houlden H, Revesz T, Wood NW (2009) Glucocerebrosidase mutations in clinical and pathologically proven Parkinson's disease. Brain : a journal of neurology 132:1783-1794.

Nichols TE (2012) Multiple testing corrections, nonparametric methods, and random field theory. NeuroImage 62:811-815.

Nocker M, Seppi K, Donnemiller E, Virgolini I, Wenning GK, Poewe W, Scherfler C (2012) Progression of dopamine transporter decline in patients with the Parkinson variant of multiple system atrophy: a voxel-based analysis of [123I]beta-CIT SPECT. European journal of nuclear medicine and molecular imaging 39:1012-1020.

Nombela C, Rowe JB, Winder-Rhodes SE, Hampshire A, Owen AM, Breen DP, Duncan GW, Khoo TK, Yarnall AJ, Firbank MJ, Chinnery PF, Robbins TW, O'Brien JT, Brooks DJ, Burn DJ, group I-Ps, Barker RA (2014) Genetic impact on cognition and brain function in newly diagnosed Parkinson's disease: ICICLE-PD study. Brain : a journal of neurology 137:2743-2758.

Obeso JA, Rodriguez-Oroz MC, Rodriguez M, Arbizu J, Gimenez-Amaya JM (2002) The basal ganglia and disorders of movement: pathophysiological mechanisms. News in physiological sciences : an international journal of physiology produced jointly by the International Union of Physiological Sciences and the American Physiological Society 17:51-55.

Oh M, Kim JS, Kim JY, Shin KH, Park SH, Kim HO, Moon DH, Oh SJ, Chung SJ, Lee CS (2012) Subregional patterns of preferential striatal dopamine transporter loss differ in Parkinson disease, progressive supranuclear palsy, and multiple-system atrophy. Journal of nuclear medicine : official publication, Society of Nuclear Medicine 53:399-406.

Oldehinkel M, Beckmann CF, Pruim RH, van Oort ES, Franke B, Hartman CA, Hoekstra PJ, Oosterlaan J, Heslenfeld D, Buitelaar JK, Mennes M (2016) Attention-Deficit/Hyperactivity Disorder symptoms coincide with altered striatal connectivity. Biological psychiatry : cognitive neuroscience and neuroimaging 1:353-363.

Orru G, Pettersson-Yeo W, Marquand AF, Sartori G, Mechelli A (2012) Using Support Vector Machine to identify imaging biomarkers of neurological and psychiatric disease: a critical review. Neuroscience and biobehavioral reviews 36:1140-1152.

Pagonabarraga J, Kulisevsky J, Llebaria G, Garcia-Sanchez C, Pascual-Sedano B, Martinez-Corral M, Gironell A (2010) PDD-Short Screen: a brief cognitive test for screening dementia in Parkinson's disease. Movement disorders : official journal of the Movement Disorder Society 25:440-446.

Paulus W, Jellinger K (1991) The neuropathologic basis of different clinical subgroups of Parkinson's disease. Journal of neuropathology and experimental neurology 50:743-755.

Pereira F, Mitchell T, Botvinick M (2009) Machine learning classifiers and fMRI: a tutorial overview. NeuroImage 45:S199-209.

Pihlstrom L, Toft M (2011) Genetic variability in SNCA and Parkinson's disease. Neurogenetics 12:283-293.

Pirker W (2003) Correlation of dopamine transporter imaging with parkinsonian motor handicap: how close is it? Movement disorders : official journal of the Movement Disorder Society 18 Suppl 7:S43-51.

Poldrack RA, Baker CI, Durnez J, Gorgolewski KJ, Matthews PM, Munafo MR, Nichols TE, Poline JB, Vul E, Yarkoni T (2017) Scanning the horizon: towards transparent and reproducible neuroimaging research. Nature reviews Neuroscience 18:115-126.

Rajput AH, Voll A, Rajput ML, Robinson CA, Rajput A (2009) Course in Parkinson disease subtypes: A 39-year clinicopathologic study. Neurology 73:206-212.

Ravina B, Marek K, Eberly S, Oakes D, Kurlan R, Ascherio A, Beal F, Beck J, Flagg E, Galpern WR, Harman J, Lang AE, Schwarzschild M, Tanner C, Shoulson I (2012) Dopamine transporter imaging is associated with long-term outcomes in Parkinson's disease. Movement disorders : official journal of the Movement Disorder Society 27:1392-1397.

Reijnders JS, Ehrt U, Lousberg R, Aarsland D, Leentjens AF (2009) The association between motor subtypes and psychopathology in Parkinson's disease. Parkinsonism & related disorders 15:379-382.

Rektor I, Rektorova I, Kubova D (2006) Vascular parkinsonism--an update. Journal of the neurological sciences 248:185-191.

Robbins TW, Cools R (2014) Cognitive deficits in Parkinson's disease: a cognitive neuroscience perspective. Movement disorders : official journal of the Movement Disorder Society 29:597-607.

Rodriguez-Oroz MC, Jahanshahi M, Krack P, Litvan I, Macias R, Bezard E, Obeso JA (2009) Initial clinical manifestations of Parkinson's disease: features and pathophysiological mechanisms. The Lancet Neurology 8:1128-1139.

Rosenberg-Katz K, Herman T, Jacob Y, Giladi N, Hendler T, Hausdorff JM (2013) Gray matter atrophy distinguishes between Parkinson disease motor subtypes. Neurology 80:1476-1484.

Rossi C, Frosini D, Volterrani D, De Feo P, Unti E, Nicoletti V, Kiferle L, Bonuccelli U, Ceravolo R (2010) Differences in nigro-striatal impairment in clinical variants of early Parkinson's disease: evidence from a FP-CIT SPECT study. European journal of neurology 17:626-630.

Salas-Gonzalez D, Gorriz JM, Ramirez J, Illan IA, Lang EW (2013) Linear intensity normalization of FP-CIT SPECT brain images using the alpha-stable distribution. NeuroImage 65:449-455.

Samii A, Nutt JG, Ransom BR (2004) Parkinson's disease. Lancet 363:1783-1793.

Scherfler C, Seppi K, Donnemiller E, Goebel G, Brenneis C, Virgolini I, Wenning GK, Poewe W (2005) Voxel-wise analysis of [123I]beta-CIT SPECT differentiates the Parkinson variant of multiple system atrophy from idiopathic Parkinson's disease. Brain : a journal of neurology 128:1605-1612.

Schillaci O, Chiaravalloti A, Pierantozzi M, Di Pietro B, Koch G, Bruni C, Stanzione P, Stefani A (2011) Different patterns of nigrostriatal degeneration in tremor type versus the akinetic-rigid and mixed types of Parkinson's disease at the early stages: molecular imaging with 123I-FP-CIT SPECT. International journal of molecular medicine 28:881-886.

Schillaci O, Pierantozzi M, Filippi L, Manni C, Brusa L, Danieli R, Bernardi G, Simonetti G, Stanzione P (2005) The effect of levodopa therapy on dopamine transporter SPECT imaging with(123)I-FP-CIT in patients with Parkinson's disease. European journal of nuclear medicine and molecular imaging 32:1452-1456.

Schlesinger I, Schlesinger N (2008) Uric acid in Parkinson's disease. Movement disorders : official journal of the Movement Disorder Society 23:1653-1657.

Schwarzschild MA, Marek K, Eberly S, Oakes D, Shoulson I, Jennings D, Seibyl J, Ascherio A, Parkinson Study Group PI (2011) Serum urate and probability of dopaminergic deficit in early "Parkinson's disease". Movement disorders : official journal of the Movement Disorder Society 26:1864-1868.

Schwarzschild MA, Schwid SR, Marek K, Watts A, Lang AE, Oakes D, Shoulson I, Ascherio A, Parkinson Study Group PI, Hyson C, Gorbold E, Rudolph A, Kieburtz K, Fahn S, Gauger L, Goetz C, Seibyl J, Forrest M, Ondrasik J (2008) Serum urate as a predictor of clinical and radiographic progression in Parkinson disease. Archives of neurology 65:716-723.

Selikhova M, Williams DR, Kempster PA, Holton JL, Revesz T, Lees AJ (2009) A clinico-pathological study of subtypes in Parkinson's disease. Brain : a journal of neurology 132:2947-2957.

Seto-Salvia N, Clarimon J, Pagonabarraga J, Pascual-Sedano B, Campolongo A, Combarros O, Mateo JI, Regana D, Martinez-Corral M, Marquie M, Alcolea D, Suarez-Calvet M, Molina-Porcel L, Dols O, Gomez-Isla T, Blesa R, Lleo A, Kulisevsky J (2011) Dementia risk in Parkinson disease: disentangling the role of MAPT haplotypes. Archives of neurology 68:359-364.

Sidransky E, Nalls MA, Aasly JO, Aharon-Peretz J, Annesi G, Barbosa ER, Bar-Shira A, Berg D, Bras J, Brice A, Chen CM, Clark LN, Condroyer C, De Marco EV, Durr A, Eblan MJ, Fahn S, Farrer MJ, Fung HC, Gan-Or Z, Gasser T, Gershoni-Baruch R, Giladi N, Griffith A, Gurevich T, Januario C, Kropp P, Lang AE, Lee-Chen GJ, Lesage S, Marder K, Mata IF, Mirelman A, Mitsui J, Mizuta I, Nicoletti G, Oliveira C, Ottman R, Orr-Urtreger A, Pereira LV, Quattrone A, Rogaeva E, Rolfs A, Rosenbaum H, Rozenberg R, Samii A, Samaddar T, Schulte C, Sharma M, Singleton A, Spitz M, Tan EK, Tayebi N, Toda T, Troiano AR, Tsuji S, Wittstock M, Wolfsberg TG, Wu YR, Zabetian CP, Zhao Y, Ziegler SG (2009) Multicenter analysis of glucocerebrosidase mutations in Parkinson's disease. The New England journal of medicine 361:1651-1661.

Smith SM, Miller KL, Moeller S, Xu J, Auerbach EJ, Woolrich MW, Beckmann CF, Jenkinson M, Andersson J, Glasser MF, Van Essen DC, Feinberg DA, Yacoub ES, Ugurbil K (2012) Temporally-independent functional modes of spontaneous brain activity. Proceedings of the National Academy of Sciences of the United States of America 109:3131-3136.

Spiegel J, Hellwig D, Samnick S, Jost W, Mollers MO, Fassbender K, Kirsch CM, Dillmann U (2007) Striatal FP-CIT uptake differs in the subtypes of early Parkinson's disease. Journal of neural transmission 114:331-335.

Sun CC, Luo FF, Wei L, Lei M, Li GF, Liu ZL, Le WD, Xu PY (2012) Association of serum uric acid levels with the progression of Parkinson's disease in Chinese patients. Chinese medical journal 125:583-587.

Tatsch K, Poepperl G (2013) Nigrostriatal dopamine terminal imaging with dopamine transporter SPECT: an update. Journal of nuclear medicine : official publication, Society of Nuclear

Medicine 54:1331-1338.

Tipping ME (2004) Bayesian inference: An introduction to principles and practice in machine learning. Advanced lectures on machine Learning 1-19.

Van Essen DC, Smith SM, Barch DM, Behrens TEJ, Yacoub E, Ugurbil K (2013) The WU-Minn Human Connectome Project: An overview. NeuroImage 80:62-79.

Varrone A, Dickson JC, Tossici-Bolt L, Sera T, Asenbaum S, Booij J, Kapucu OL, Kluge A, Knudsen GM, Koulibaly PM, Nobili F, Pagani M, Sabri O, Vander Borght T, Van Laere K, Tatsch K (2013) European multicentre database of healthy controls for [123I]FP-CIT SPECT (ENC-DAT): age-related effects, gender differences and evaluation of different methods of analysis. European journal of nuclear medicine and molecular imaging 40:213-227.

Vriend C, Nordbeck AH, Booij J, van der Werf YD, Pattij T, Voorn P, Raijmakers P, Foncke EM, van de Giessen E, Berendse HW, van den Heuvel OA (2014a) Reduced dopamine transporter binding predates impulse control disorders in Parkinson's disease. Movement disorders : official journal of the Movement Disorder Society 29:904-911.

Vriend C, Raijmakers P, Veltman DJ, van Dijk KD, van der Werf YD, Foncke EM, Smit JH, Berendse HW, van den Heuvel OA (2014b) Depressive symptoms in Parkinson's disease are related to reduced [123I]FP-CIT binding in the caudate nucleus. Journal of neurology, neurosurgery, and psychiatry 85:159-164.

Wen M, Zhou B, Chen YH, Ma ZL, Gou Y, Zhang CL, Yu WF, Jiao L (2017) Serum uric acid levels in patients with Parkinson's disease: A meta-analysis. PloS one 12:e0173731.

Wikle C, Royle J (2002) Spatial statistical modeling in biology. Mississauga, ON: EOLSS Publishers Co Ltd 1-27.

Williams-Gray CH, Goris A, Saiki M, Foltynie T, Compston DA, Sawcer SJ, Barker RA (2009) Apolipoprotein E genotype as a risk factor for susceptibility to and dementia in Parkinson's disease. Journal of neurology 256:493-498.

Williams-Gray CH, Mason SL, Evans JR, Foltynie T, Brayne C, Robbins TW, Barker RA (2013) The CamPaIGN study of Parkinson's disease: 10-year outlook in an incident population-based cohort. Journal of neurology, neurosurgery, and psychiatry 84:1258-1264.

Winder-Rhodes SE, Evans JR, Ban M, Mason SL, Williams-Gray CH, Foltynie T, Duran R, Mencacci NE, Sawcer SJ, Barker RA (2013) Glucocerebrosidase mutations influence the natural history of Parkinson's disease in a community-based incident cohort. Brain : a journal of neurology 136:392-399.

Winikates J, Jankovic J (1999) Clinical correlates of vascular parkinsonism. Archives of neurology 56:98-102.

Wu K, O'Keeffe D, Politis M, O'Keeffe GC, Robbins TW, Bose SK, Brooks DJ, Piccini P, Barker RA (2012) The catechol-O-methyltransferase Val(158)Met polymorphism modulates fronto-cortical dopamine turnover in early Parkinson's disease: a PET study. Brain : a journal of neurology 135:2449-2457.

Zaidel A, Arkadir D, Israel Z, Bergman H (2009) Akineto-rigid vs. tremor syndromes in Parkinsonism. Current opinion in neurology 22:387-393.

Zarogianni E, Moorhead TW, Lawrie SM (2013) Towards the identification of imaging biomarkers in

schizophrenia, using multivariate pattern classification at a single-subject level. NeuroImage Clinical 3:279-289.

Zijlmans J, Evans A, Fontes F, Katzenschlager R, Gacinovic S, Lees AJ, Costa D (2007) [123I] FP-CIT spect study in vascular parkinsonism and Parkinson's disease. Movement disorders : official journal of the Movement Disorder Society 22:1278-1285.

Zijlmans JC, Daniel SE, Hughes AJ, Revesz T, Lees AJ (2004) Clinicopathological investigation of vascular parkinsonism, including clinical criteria for diagnosis. Movement disorders : official journal of the Movement Disorder Society 19:630-640.

Appendix

Templates

In collaboration with the nuclear medicine unit of Virgen del Rocío Hospital (Seville, Spain), we have created useful [123I]FP-CIT SPECT templates in standard MNI space (Montreal Neurological Instite) available for the neuroimaging community. In this work, we have used two templates: the first to spatially normalize [123I]FP-CIT SPECT images to standard space; the second to identify posterior, anterior and ventral subregions within the striatum.

[123I]FP-CIT SPECT template. This template was created by spatially normalizing and averaging the scans of 30 normal controls. Available at: http://www.nitrc.org/projects/spmtemplates
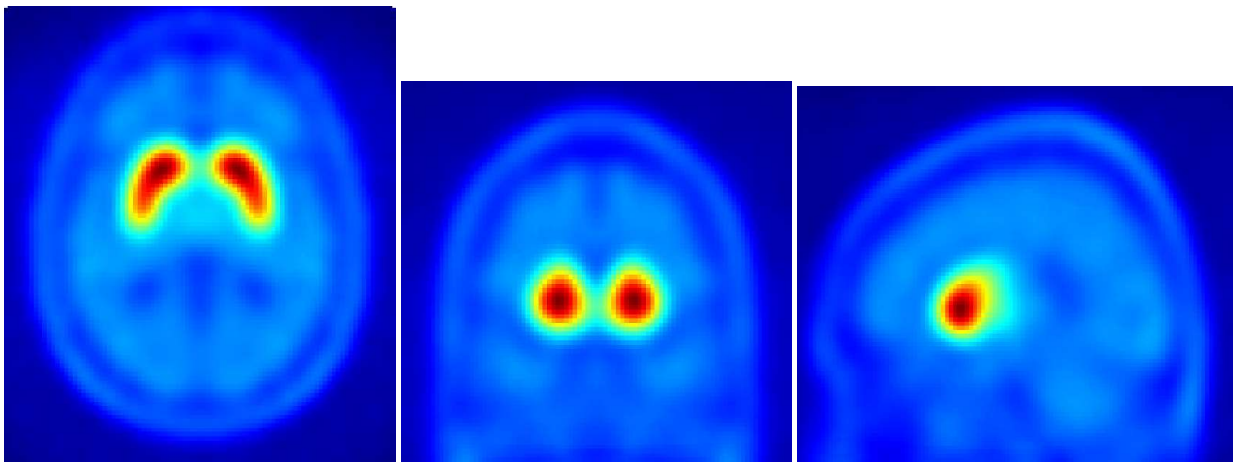
Striatal VOImap. This template was created with ^{18}F-DOPA PET of 12 normal controls. Each striatum was divided into 6 sub-regions: ventral caudate, anterior dorsal caudate, posterior dorsal caudate, ventral putamen, anterior dorsal putamen and posterior dorsal putamen, based on Mawlawi et al. (J Cereb Blood Flow Metab. 2001;21:1034–57) and Oh et al. (J Nucl Med.2012;53:399–406) segmentation. A nonspecific background volume was drawn in the occipital cortex. Available at: http://www.nitrc.org/projects/spmtemplates